ASSESSMENT OF MATERIAL STATE IN COMPOSITES USING GLOBAL DIELECTRIC STATE VARIABLE

by

VAMSEE VADLAMUDI

DISSERTATION

Submitted in partial fulfillment of the requirements

for the degree of Doctor of Philosophy at

The University of Texas at Arlington

December, 2019

Arlington, Texas

Supervising Committee:

Kenneth Reifsnider, Supervising Professor

Endel Iarve, Co-Supervisor

Ashfaq Adnan

Robert Taylor

Ye Cao

Abstract

ASSESSMENT OF MATERIAL STATE IN COMPOSITES USING GLOBAL

DIELECTRIC STATE VARIABLE

Vamsee Vadlamudi, Ph.D.

The University of Texas at Arlington, 2019

Supervising Professors: Kenneth Reifsnider, Endel Iarve

Composites are heterogeneous in nature and a fundamental understanding of the material response to applied mechanical, thermal, electrical and other multi-physical fields is required to efficiently design and synthesize the material system and demands attention to long-term behavior in particular. Unlike metals, composites are designed to develop distributed damage and initiation of a single microscopic crack does not individually affect the strength/life of these materials. Therefore, the primary interest is not in single local events but in the process of interaction of multiple events that have a collective global effect on the material behavior. The interaction of these local events are interpreted using 'state' of the material by the means of 'state' variables e.g. strength, stiffness etc. However, it was observed that the evolution of these state variables are not uniformly progressive in nature even though the damage progression is progressive.

The primary objective of this research is to identify a unique state variable that can assess the material state during service and provide warning of impending failure. This work is focused on in-situ monitoring of material state during quasi-static loading for different material systems, stacking sequences. This work also develops a finite element based multiphysics model that attempts to explain the variation of the in-situ response during damage development. Finally, the shortcomings, challenges of the multiphysics model and recommendations for future work are discussed.

Acknowledgements

I would like to thank Dr. Kenneth Reifsnider, my supervising professor, for his invaluable guidance, support and time that made this work possible. His encouraging words and hunger for learning motivated me throughout my graduate studies. This has been a life-changing journey for me and it would not have been possible without the support and guidance from Dr. Reifsnider in particular.

I would also like to thank Dr. Endel Iarve, my co-supervising professor for his guidance and support during this journey. I am grateful to my advisory committee, Dr. Ashfaq Adnan, Dr. Robert Taylor and Dr. Ye Cao for their valuable suggestions that motivated me in designing some experiments and simulations to portray the effectiveness of the technique.

I would like to thank my dear friends/colleagues, Dr. Rassel Raihan, Dr. Hari Adluru for their time, support and guidance during challenging times. I really appreciate the help of my colleagues, Jared, Ed, Ron, Dave, Muthu, Patrick, Rauhon, Sabari, Deepak, Jani and many others during my doctoral research.

Lastly but not least, I would like to thank my Parents and Sister for their sacrifices and unselfish love and support which kept me going.

Table of Contents

List of Figures

List of Tables

Chapter 1 Introduction

1.1 Background

Composite materials have significant advantages over metals and other conventional materials. These material systems have found their way into many advanced applications, i.e., aerospace, bio-medical, energy storage, civil structures etc. Composites are heterogeneous in nature and a fundamental understanding of the material response to applied mechanical, thermal, electrical and other multi-physical fields is required to efficiently design and synthesize the material system and demands attention to long-term behavior in particular. The heterogeneity of these material systems arises from their constituent phases (i.e. fiber, matrix, and interface/interphase) that make up a lamina, which in turn are stacked in a sequence with varying fiber orientations depending on the application to form a laminate. Hence, the behavior of the material system is dependent on the interaction of these phases in the micro (local) scale and interaction of the laminae at large on the global scale.

Unlike metals, composites are designed to develop distributed damage and initiation of a single microscopic crack does not individually affect the strength/life of these materials. Therefore, the primary interest is not in single local events but in the process of interaction of multiple events that have a collective global effect on the material behavior. The interaction of these local events are interpreted using 'state' of the material by the means of 'state' variables e.g. strength, stiffness etc. Historically the evolution of these state variables with life was used as the measure of durability. However, it was observed that the evolution of these state variables are not uniformly progressive in nature even though the damage progression is progressive. Reifsnider et al observed that the evolution is more of a sudden death phenomenon as shown in Figure 1.1 [1]. From Figure 1.1, it can be observed that the state variables are almost stable until a certain stage after which the

behavior is unstable which could be catastrophic to primary load bearing structures. Based on experimental evidence, the evolution of damage can be classified in to three stages: Damage Initiation, Damage Accumulation & Growth and Damage Interaction as shown below in Figure 1.1.
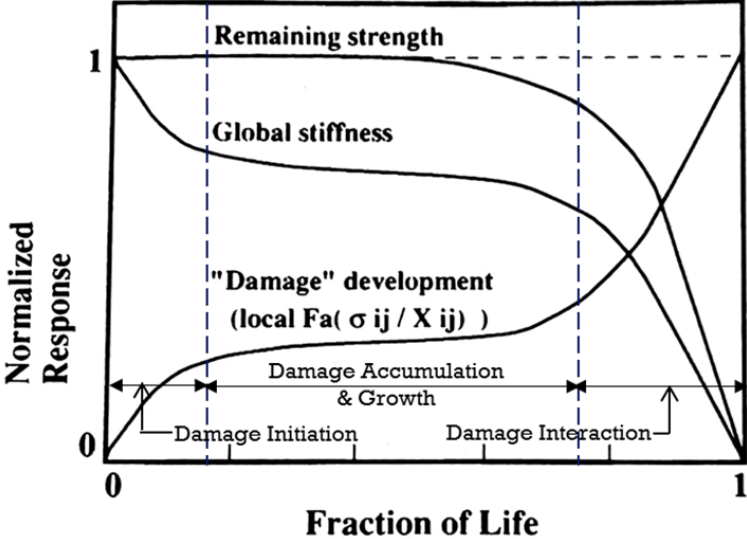
Figure 1.1 Evolution of material state variables during the life of a composite material system [1]
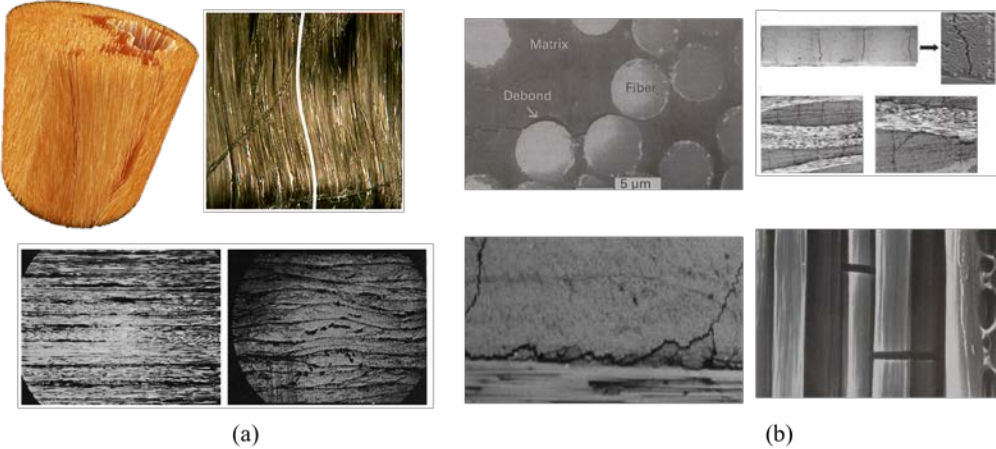
Figure 1.2(a) Defects during processing [2, 4] (b) damage modes observed in service [3]

A vast amount of literature is available on different damage modes, and their progression in both uni-directional and woven composites; damage could initiate because of defects during processing or could develop during service as shown above in Figure 1.2 (a, b) [2-4]. Figure 1.3 depicts the progression of damage in uni-directional composites during fatigue [5]. As observed in Figure 1.3, the initiation of damage starts with matrix micro cracking followed by debonding between fiber-matrix or debonding between fiber-matrix leading to micro cracking [3]. These matrix cracks initiate at different sites along the length of the specimen until a saturation state referred to as the characteristic damage state (CDS) is obtained [5]. CDS is most often referred to a state where in the crack spacing reaches a saturation value after which no more individual cracks are developed in the current ply. At this state, there is generally a significant drop in stiffness but not in the strength as shown in Figure 1.1. This is then followed by creation of secondary cracks that are transverse to the primary cracks in the neighboring plies, followed by coupling of these primary and secondary cracks at the free edge of the sample to initiate edge delaminations. These secondary cracks are created at various sites along the width of the specimen and initiate local interior delaminations which differ from edge delaminations. In the final state of damage development, these secondary cracks interact and grow at a rapid 'rate' such that the locally failed regions find a path which then (aided by fiber fractures) lead to sudden drop in the strength and to final failure.
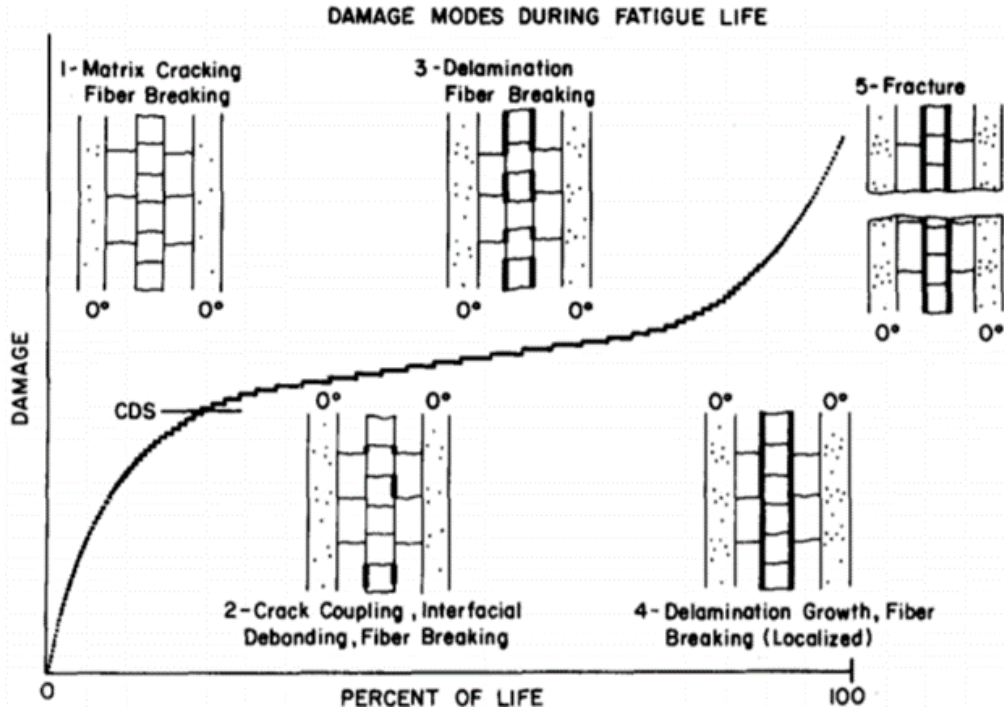
Figure 1.3 Damage modes during fatigue in uni-directional composites [5]

The modes of damage in woven composites are different then what is observed in uni-directional composites. The response to loading in the fiber directions can often be approximated as linear. However, the response to off-axis loading orientations is highly complex and significantly non-linear with very high strain to failure. Figure 1.4 shows the response of a [+-45°] tension specimen [6]. The response can be described in four zones based on applied strain, a different type of behavior is observed in each zone. As loading begins, an initial elastic (mostly) response is observed (zone 1) up to approximately 0.5% strain. At this point, matrix cracks begin to occur (zone 2) and on continuous loading, the density of these matrix cracks keep increasing, and the response becomes non-linear. Around 4% strain (zone 3), the density of matrix cracks saturates and very few new single cracks are formed (CDS). Once a state of crack saturation is attained, the non-linearity resulting from matrix cracking is no longer prevalent. In this zone, the behavior is dominated by the fibers which have a tendency to reorient towards the loading

4

direction. This behavior is referred to as trellising wherein the angle between reinforcement directions changes from 90°. The result of this is a stiffening response as observed in zone 3. Fiber trellising continues until about 13% strain, where the fibers eventually begin to fail (zone 4). The final non-linearity is the likely result of statistically based fiber failure over a range of axial strain [6].
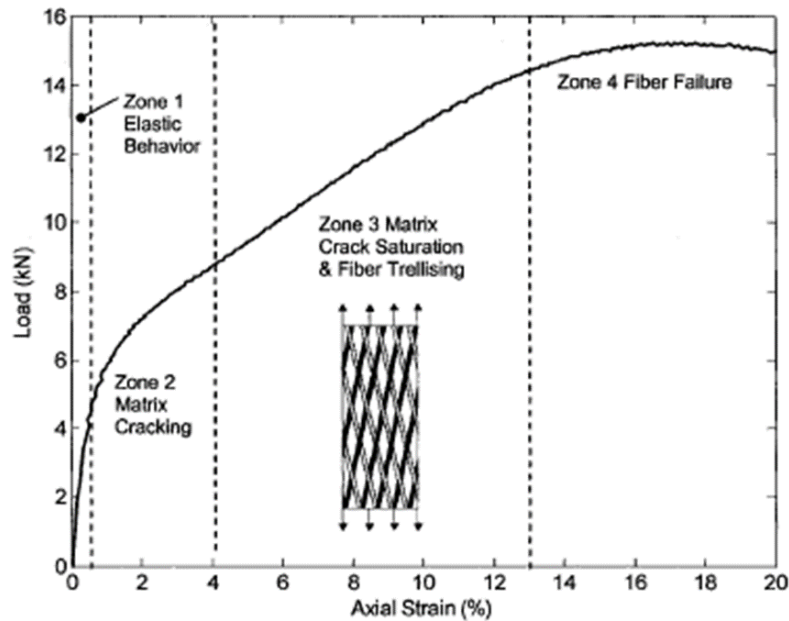
Figure 1.4 Constitutive response of an off-axis woven composite specimen [6]

1.2 Problem Definition

From literature, it is evident that the evolution of the material state is not uniformly progressive in nature even though the damage progression is progressive. Given the complexity of damage modes; the location of the damage is mostly internal. Using advanced non-destructive evaluation (NDE) techniques one can accurately determine the location and nature of damage; however by the time that information is obtained the structure would have already lost its load bearing capability as shown in Figure 1.5 [7]. Considering this sensitivity and instability of state variables to damage details in the final phase of life; the first question is how to measure and

5

interpret these state variables non-invasively during service before the final phase or 'critical' state occurs, [8-9] and the second question (being the most important) is the existence of a single state variable that can identify that critical material state. Based on these questions, recently much emphasis has been given to identification of damage precursors that would provide warning of impending failure. That is the primary objective of the present investigation.
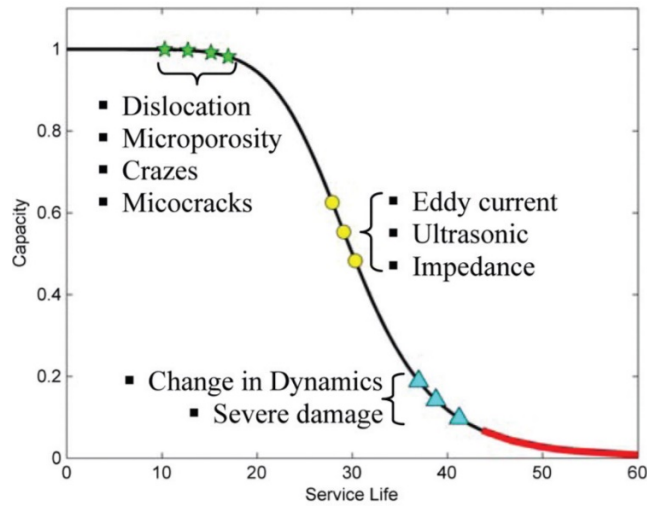
Figure 1.5 Capabilities of current NDE techniques to capture damage state w.r.t structural capacity [7]

1.3 Dissertation Layout

This dissertation is focused in this direction with a specific discussion of broadband dielectric spectroscopy (BbDS) as a potential technique to capture and interpret the material state in Chapter 2. This includes a literature review of the application of BbDS to monitor the material state in composites.

This is followed by discussion of governing equations for modeling the dielectric response of the material system, applying these governing equations to determine the effective (homogenized) dielectric properties of a lamina for the multiphysics analysis.

Chapter 4 discusses insitu monitoring of the material state during uni axial tensile loading for different material systems.

Chapter 5 discusses the development of multiphysics model to simulate/predict the insitu variation of dielectric response. Finally conclusions and future research directions at the end of the dissertation.

1.4 References

[1]   Reifsnider, K. L., & Case, S. W. (2002). Durability and Damage Tolerance of Material Systems. NY: John Wiley & Sons.

[2]   Bowles, K. J., & Frimpong, S. (1992). Void effects on the interlaminar shear strength of unidirectional graphite-fiber-reinforced composites. Journal of composite materials, 26(10), 1487-1509.

[3]   Talreja, R. (2008). Damage and fatigue in composites–a personal account. Composites Science and Technology, 68(13), 2585-2591.

[4]   Raihan, M. (2014). Dielectric Properties of Composite Materials during Damage Accumulation and Fracture. (Doctoral dissertation, University of South Carolina).

[5]   Retrieved from https://scholarcommons.sc.edu/etd/2896

[6]   Reifsnider, K. L., Henneke, E. G., Stinchcomb, W. W., & Duke, J. C. (1983). Damage mechanics and NDE of composite laminates. In Mechanics of composite materials (pp. 399-420). Pergamon.

[7]   Hufner, D. R. (2008). Progressive failure of woven polymer-based composites under dynamic loading; Theory and analytical simulation. (Doctoral dissertation, University of Connecticut). Retrieved from https://opencommons.uconn.edu/dissertations/AAI3308233

[8]   Haile, M. A., Hall, A. J., Yoo, J. H., Coatney, M. D., & Myers, O. J. (2016). Detection of damage precursors with embedded magnetostrictive particles. Journal of Intelligent Material Systems and Structures, 27(12), 1567-1576.

[9]   Reifsnider, K., Rabbi, F., Vadlamudi, V., Raihan, R., & Brinkman, K. (2017). Critical path-driven property and performance transitions in heterogeneous microstructures. Journal of Materials Science, 52(9), 4796-4809.

[10]   Talreja, R. (2014). Assessment of the fundamentals of failure theories for composite materials. Composites Science and Technology, 105, 190-201.

Chapter 2 Dielectric State Variable for Measuring Material State

2.1 Background

In Chapter 1, the need to capture the 'critical' material state has been established and the possibility of defining a single state variable that can capture this critical state was discussed. In this chapter, broadband dielectric spectroscopy (BbDS) as an effective technique to capture and interpret the material state will be discussed.

2.2 Material System as a Sensor for Understanding the Material State

Several NDE techniques are implemented to study the structural integrity of composites; a brief review of these techniques can be studied in article [1]. Most of the NDE techniques involve input some kind of a signal/energy source and/or embed sensors inside the material to monitor response to evolving material state. However some techniques such as acoustic emission (AE), broadband dielectric spectroscopy (BbDS) etc. monitor the behavior of the material based on emission of energy during the process of fracture which makes these techniques unique.

During continuous loading, there is a high concentration of energy deposited into a small volume of material and in the event of crack initiation/propagation/fracture all this energy is released instantaneously leading to one or more ways of dissipation such as: localized heating, acoustic waves, generation of excitations and defects in the material, production of dangling bonds and trapped electrons on or near the freshly created crack wall surface, separation of charges on the crack walls with accompanying intense electric fields for many insulating materials [2]. These forms of such emission accompanying fracture are referred to as "fracto-emission" (FE). Fracto-emission has been a promising field of research to study the fracture events of ceramics, rocks, earth quakes, elastomers etc. [2-4]. Dickinson et al. surveyed the emission of charged particles

from several classes of materials ranging from metals to elastomers [2]. With regard to composites, they had observed that the intensity of fracto-emission was significant in fiber reinforced composites rather than for individual constituents itself as observed in Figure 2.1 and Figure 2.2.
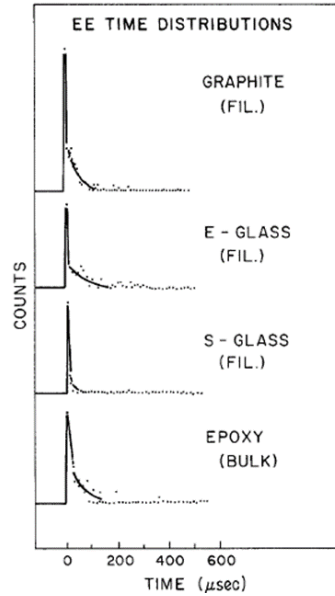
Figure 2.1 Electron emission distributions during fracture of constituent phases of composites [2]
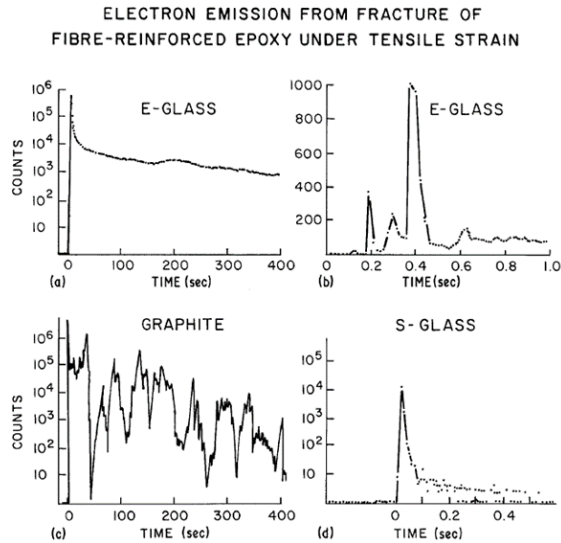
Figure 2.2 (a)FE from E-glass fiber reinforced composites (b) initial counts of FE from E-glass fiber reinforced composites (c) FE from graphite fiber reinforced composites and (d) initial FE counts from S-glass fiber reinforced composite [2]

It can be observed that different fiber-epoxy systems have different FE curves. For example, the emission from E-glass is considerably more intense and longer lasting than for S-glass as observed in Figure 2.2 (a) and (d). Examination under a microscope of the samples following rupture showed considerably more delamination and separation of the filaments in the case of E-glass than for S-glass. The larger diameter E-glass filaments (20μm compared to 10μm) could have contributed to the degree of interfacial failure. Also, FE observed in graphite reinforced composites was similar to E-glass with large intensity but erratic in nature as observed in Figure 2.2 (c). This erratic behavior was primarily due to the high conductivity of graphite leading to surface charging and discharging that altered the FE [2].

Dickinson et al. observed that prior to rupture, the samples suffered minor failures. These failures were primarily fiber breakage and epoxy failure and produced FE similar to that of constituents as observed in Figure 2.1and Figure 2.2 (b). During the process of continuous loading, these minor failures accumulated and the entire strand failed producing a large amount of interfacial failure (delamination) between the filaments and epoxy. They postulated that the latter form of failure was responsible for the major FE component with slow decay and is possibly an indicator of the extent of interfacial failure that had occurred [2]. This observation is critical as it postulates that during individual failures, the intensity is very rapid but lasts only for a short period (Figure 2.2 (b)), whereas during interaction of these individual damage modes the intensity is distributed over a large amount of time (compared to individual events).

Based on the observations of fracto-emissions in composite materials it can be concluded that when multiple events such as matrix cracking, delamination, fiber pullout, fiber fracture etc. are involved different intensities of charge emissions are recorded based on the state of the damage. If one can devise a technique capable of using these emissions to understand the state of the

material, real-time predictions can be made on the state of the damage and measures can be taken to repair/replace the part before catastrophe.

2.3 Broadband Dielectric Spectroscopy (BbDS)

Dielectrics are electrically non-conducting materials such as glass, porcelain, and polymers etc. which exhibit the ability of the electric field to polarize the material creating electric dipoles. Fiber reinforced composites are naturally dielectric primarily due to the heterogeneous microstructure, interfaces and defects (voids, cracks etc.) that act as charge trapping sites.

The displacement of charged particles in atoms or molecules leads to development of a net dipole moment along the applied field direction. The net dipole moment per unit volume is termed as Polarization. Broadband Dielectric Spectroscopy (BbDS) is an established experimental tool that describes the interaction of electromagnetic waves with matter and reflects by that the underlying molecular mechanisms typically in the frequency range from a lower value of 10^{-6} Hz to a higher frequency of 10^{12} Hz. The frequency regime contains information about molecular and collective dipolar fluctuation; charge transport and polarization effects that occur at inner and outer boundaries in the form of different dielectric properties of the material under study [5].

2.4 Polarization Mechanisms

Several polarization mechanisms can occur in a material system, i.e. electronic, ionic (molecular), atomic, dipolar (orientational), interfacial polarizations [6]. Figure 2.3 shows the effect of different charge displacement mechanisms on dielectric response and their corresponding effective frequency range and polarization mechanism.
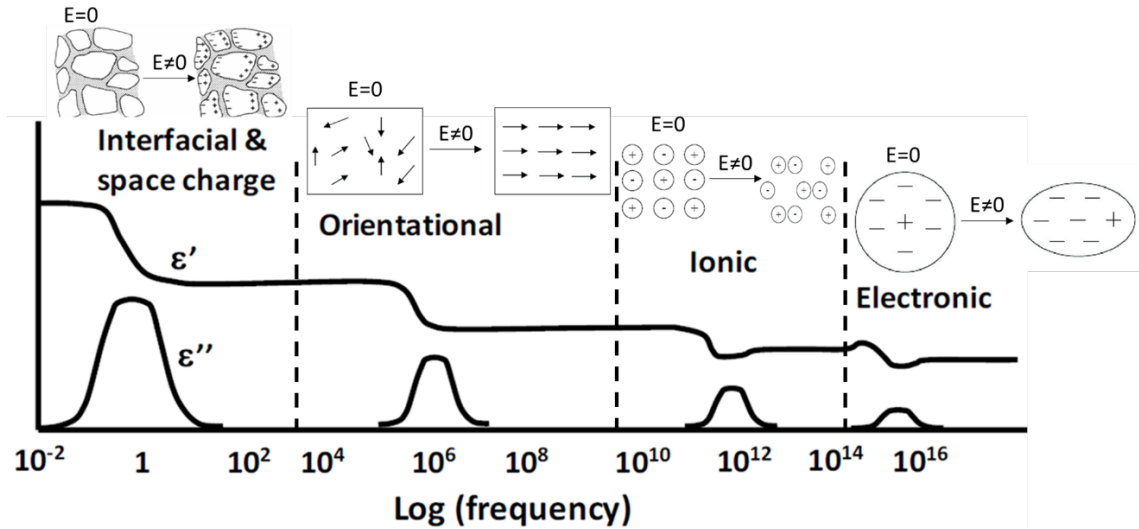
Figure 2.3 Dielectric response to different polarization mechanisms in different frequency regimes [6]

Below is a summary of different polarization mechanisms. In the atomic scale, the separation of effective centers of positive charges from effective centers of negative charge in the presence of an external electric field leads to creation of a net dipole moment and this mechanism of polarization is called electronic polarization. In ionic crystals, the anions and cations are arranged in a balanced structure that the net dipole moment of the structure is zero. However, under the influence of an electric field, a net dipole moment is induced because of the displacement of charges and this mechanism is termed as ionic polarization. In some crystals, the distribution of cations and anions are uneven and leads to creation of a net dipole moment because of the arrangement of these ions, termed as dipolar (permanent dipoles) molecules. In the presence of an electric field, these molecules tend to align in the electric field direction and leads to a net dipole moment. This mechanism of polarization in dipolar molecular structures is termed as orientational polarization. In the above mentioned polarizations, the charges are locally bounds in atoms or molecules. There could be some charge carriers that are not bound and can migrate through the material under the action of a low frequency electric field. These charge carriers are displaced by

the electric field and in the presence of multiple interfaces in the material system, these charge displacements are impeded at the interface and get trapped which results in charge accumulation. This mechanism is called as interfacial or space charge polarization. Based on this, it can be observed that different polarization mechanisms occur at different scales and using different frequency ranges, one can estimate the contribution of each of these different mechanisms [7].

An overview of the different polarization mechanisms was established. To better understand the concept of polarization, consider a parallel plate capacitor setup with two conducting plates separated initially by air. When the plates are charged, since there is no field inside a conductor all the charges reside on the surface of conductor called as free charges. From gauss law,

$$\nabla . E = \frac{\rho}{\varepsilon_0} \tag{2.1}$$

Where $E(V/m)$ is the electric field, $\rho(C/m^3)$ is the charge density, $\varepsilon_0(F/m)$ is the permittivity of free space. Now, assume a dielectric material is included between the parallel plates. Because of the electric field, a net dipole moment is induced inside the dielectric given by the polarization density. The positive charges move towards the surface, because of which the net charge inside is equal in magnitude with opposite sign. These charges are the bound charges given by

$$Q_b = - \oiint P . dS \tag{2.2}$$

Where $Q_b(C)$ is the total bound negative charge, $P(C/m^2)$ is the polarization density. Applying gauss divergence theorem, we get

$$Q_b = - \oiiint (\nabla . P) dV \qquad (2.3)$$

Q_b can be written as the volume integral of the bound charge density $\rho_b (C/m^3)$ which

yields

$$\nabla . P = -\rho_b \qquad (2.4)$$

From gauss law, the net electric field can be determined by

$$\nabla . E = \frac{\rho_{total}}{\varepsilon_0} = \frac{\rho_{free} + \rho_{bound}}{\varepsilon_0} \qquad (2.5)$$

Substituting eq. (2.4) into eq. (2.5) and further simplifying we get

$$\nabla . (\varepsilon_0 E + P) = \rho_{free} \qquad (2.6)$$

This effective electric field is called as the displacement electric field $D (C/m^2)$. Further,

the polarization density can be written in terms of electric field by

$$P = \varepsilon_0 \chi E \qquad (2.7)$$

Where χ is the susceptibility of the material to polarize. The displacement electric field can

now be written as

$$D = \varepsilon_0 E + P = \varepsilon_0 E (1 + \chi) = \varepsilon_0 \varepsilon_r E \qquad (2.8)$$

Where ε_r is the dielectric constant of the material.

2.5 Interfacial Polarization in Composites

In the above mentioned mechanisms, interfacial polarization is of specific interest to us as

it provides the information of redistribution and accumulation of charges between two material

systems or between two regions of the same material. The net dipole moment induced by the

applied external electric field is a global indicator of the local charge accumulation and redistribution due to local events.

From the findings of fracto emission it is evident that during events of fracture multiple charge emissions take place and because of the heterogeneity of composites these charges are trapped at the interfaces. The next question is what happens when there is no damage or no generation of new surfaces, does that mean there would be no response to an external electric field? The answer is no. The source of charge accumulation in these materials is the heterogeneous microstructure. When heterogeneous material systems are immersed in an electric field, electric charges accumulate at the discontinuity created by the interface between the different phases and is called Maxwell-Wagner-Sillars polarization (an interfacial polarization at the mesoscopic scale) [8-10]. Baker et al. performed several surface charge measurements on a polymer resin with conductive circular inserts using Atomic Force Microscope (AFM) in air at normal room and humidity conditions. They measured the charge along the surface of the material system and observed that the measured charge is somewhat distributed on either side of the inclusion [11]. Several other research groups measured the surface charge and the resulting change in dielectric properties because of the charge accumulation due to heterogeneity (introduced by cracks) in semiconductors [12-15]. Based on these findings the sources of charge accumulation and mechanisms of redistribution (polarization) in composites have been described. Next a review of various findings involving material state monitoring using BbDS (and similar approaches) is presented.

2.6 Review of Electrical Methods to Monitor Structural Integrity of Composites

Using electrical methods to monitor structural integrity of composites has been around since 1970's. The first part of the review deals with the DC measurements in which electrical

resistance is the primary variable of interest, the change in resistance is used as the indicator of damage. Robinson studied the change in resistivity of carbon fiber reinforced composites (CFRP) (on-axis) loaded in tension and compression and correlated the increase in resistance to damage in fibers and discussed the possibility of insitu measurements of resistance during flight to warn the pilot of impending failure; but emphasized the importance of uncertainty and reliability in measurements with a confidence interval [16]. Schulte et al. performed similar measurements of resistance change in on-axis CFRP during fatigue loading to continuously monitor the condition of structure [17]. Irving et al. performed insitu electrical resistance measurements during fatigue and concluded that significant resistance changes observed during initial cycles corresponded to lower fatigue life and may be used as a basis for life estimation for in-plane fatigue [18-19]. Schueler et al. used electrical conductivity mapping by developing electrical impedance tomography (EIT) methods for orthotropic materials to detect damage in CFRP using a series of network resistors to determine the change in resistance along a damage region [20]. Todoroki et al. identified delamination using variation of resistance measurements taken from multiple co-cured electrodes on the surface of a composite [21]. Wang et al. observed that during fatigue the resistance increased suddenly when delamination was initiated as it decreases the chance that fibers in adjacent layers touch each other. Under continued fatigue, another sudden increase was observed followed by noisy response due to the percent increase in area of delamination [22]. Several other research groups have used the electrical resistance measurement methods to monitor structural integrity [23-27]. However, a key point to consider is that the electrical resistance measurements depend on the change in resistivity of the material system due to damage and hence works well with CFRP. However, for glass fiber reinforced composites (FRP) the use of carbon

black fillers in matrix or embedded carbon nano tubes (CNT) have been implemented to obtain these measurements.

On the other hand techniques such as electrochemical impedance spectroscopy (EIS) and BbDS don't explicitly need any form of a conducting medium to interpret the measurement change with damage state. Using EIS, the impedance of the material system is measured which comprises of real (resistance) and imaginary (losses due to capacitive effects) parts. Generally Bode (variation of magnitude of impedance with frequency) and Nyquist (behavior of the system at different frequencies) plots are used to understand the response. Using BbDS, the complex dielectric permittivity is calculated which is comprised of real (capacitive/storage) and imaginary (conduction/relaxation/losses) parts. Generally permittivity (real and imaginary) is plotted against frequency to identify the mechanisms in the material system.

Historically, EIS has been used to monitor moisture absorption and induced damage in composites. Glass et al. used EIS to monitor damage in CFRP due to moisture absorption. They observed that with increase in moisture absorption the capacitance increases because of the opening of matrix cracks due to swelling and with time the capacitance started to decrease due to loss of active surface area. However, they observed that with increase in uptake of moisture the shear strength decreased as well and during ex-situ measurement the capacitance also decreased because of broken fibers that isolated the areas of composite exposed to moisture [28]. Bekas et al. used EIS to monitor damage in nano-enhanced composites and found direct correlation of change in impedance to damage events [29]. Fazzino et al. used EIS with woven composites and showed that the micro cracking due to fatigue changed the impedance measurements dramatically and definitively as shown in Figure 2.4. They induced surface-initiated damage using end-loaded bending. The samples were soaked in 5M NaCl solution and this ionic solution filled the micro

18

cracks and penetrated through the surface to the interior of the sample leading to conductive regions leading to a decrease in impedance. During continuous fatigue, these micro cracks coupled through the thickness and created a path (fracture plane) filled with this ionic solution resulting in a significant decrease in impedance measurements [30].
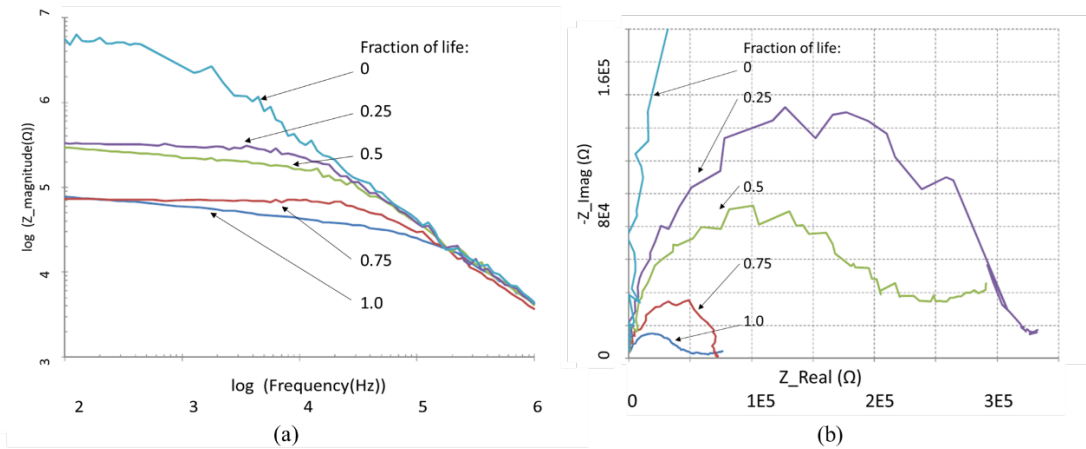
Figure 2.4(a) Bode plot and (b) Nyquist plot at various stages of life [30]

Using BbDS, Raihan et al. studied insitu dielectric response of off axis woven composites during tensile loading and observed that the dielectric permittivity rapidly increased in the beginning owing to matrix micro cracking resulting in creation of new surfaces (interfacial polarization), followed by saturation of permittivity due to crack saturation, gradual decrease due to coupling and fiber trellising, and final decrease with increased slope during the initiation of fiber fracture [31]. They categorized the response into various regions as shown in Figure 2.5. They postulated that the decrease in permittivity during coupling is because of transition from surface to volume effects.
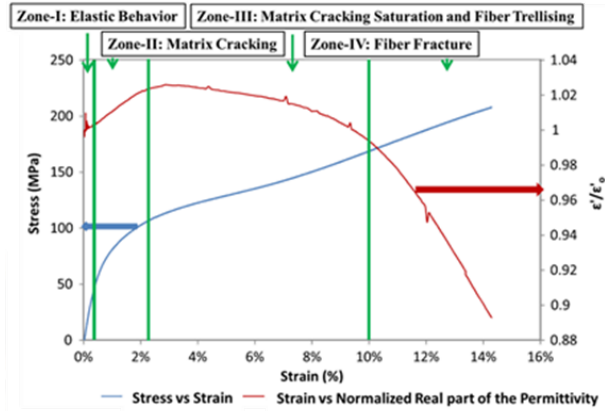
Figure 2.5 Insitu dielectric response of off-axis woven composites [31]

Further, Reifsnider et al. calculated the second variation of strain energy and the second variation of the measured capacitance with strain; normalizing both of those plots by the initial value, it was observed that the two variations were remarkably similar as shown in Figure 2.6. They concluded that the physics of damage initiation (micro-crack formation) events drives corresponding changes in strain energy and dielectric response measured in the laboratory, i.e., that those observables are dual responses to the process of damage development [32]. Several other researchers have used the BbDS technique for damage monitoring in composites and observed variation in the dielectric properties during damage development [33-36].
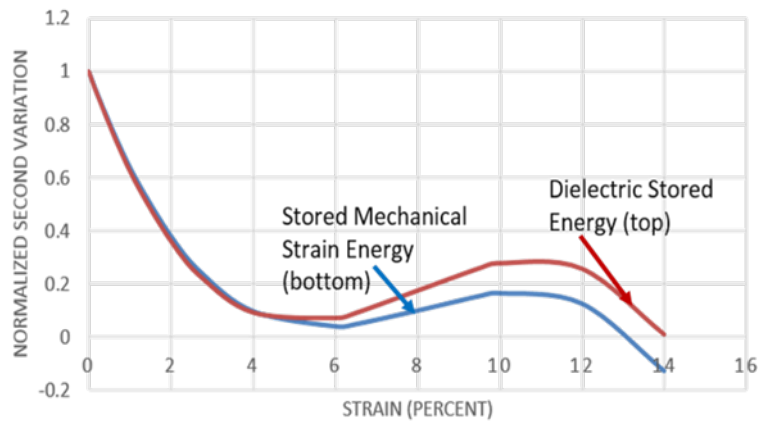
Figure 2.6 Variation of strain energy and dielectric capacitance with strain [32]

The prior work outlined in this chapter depicts the change in dielectric response during damage progression, it successfully explains the initial increase in permittivity with micro cracking, however it doesn't fully explain the science of 'why' (why the response changes), 'what' (what mechanism is causing this change) and 'how' (can we model this mechanism and the resulting change in the dielectric response) during damage interaction. In the upcoming chapters a multiphysics model is discussed and developed which tries to answer and validate these questions and observations.

In chapter 3, the working principle of dielectric measurements is outlined followed by interpretation of these measurements. The governing equations for modeling the dielectric response are then derived followed by a micromechanics model to depict the polarization mechanisms in composites. This is then followed by prediction of lamina properties (mechanical and dielectric) using different representative volume elements (RVE) and developing the basis for multiphysics based finite element model.

2.7 References

[1]   Gholizadeh, S. (2016). A review of non-destructive testing methods of composite materials. Procedia Structural Integrity, 1, 50-57.

[2]   Dickinson, J. T., Donaldson, E. E., & Park, M. K. (1981). The emission of electrons and positive ions from fracture of materials. Journal of Materials Science, 16(10), 2897-2908.

[3]   Carpinteri, A., & Borla, O. (2017). Fracto-emissions as seismic precursors. Engineering Fracture Mechanics, 177, 239-250.

[4]   Enomoto, Y., & Hashimoto, H. (1990). Emission of charged particles from indentation fracture of rocks. Nature, 346(6285), 641.

[5]   Kremer, F. (2002). Dielectric spectroscopy–yesterday, today and tomorrow. Journal of Non-Crystalline Solids, 305(1-3), 1-9.

[6]   Raju, G. G. (2003). Dielectrics in electric fields. NY: CRC press.

[7]   Kremer, F., & Schönhals, A. (Eds.). (2012). Broadband dielectric spectroscopy. NY: Springer Science & Business Media.

[8]   Scaife, B. K. P. (1989). Principles of dielectrics. Oxford: Clarendon Press

[9]   Sillars, R. W. (1937). The properties of a dielectric containing semiconducting particles of various shapes. Journal of the Institution of Electrical Engineers, 80(484), 378-394.

[10]   Pelster, R., & Simon, U. (1999). Nanodispersions of conducting particles: preparation, microstructure and dielectric properties. Colloid and polymer science, 277(1), 2-14.

[11]   Baker, J., Adkins, J. M., Rabbi, F., Liu, Q., Reifsnider, K., & Raihan, R. (2014). Meso-design of heterogeneous dielectric material systems: Structure property relationships. Journal of Advanced Dielectrics, 4(02), 1450008.

[12]   Penmecha, B. P. (2013). Fracture of materials undergoing solid-solid phase transformation. (Doctoral dissertation, California Institute of Technology).

        Retrieved from https://resolver.caltech.edu/CaltechTHESIS:05302013-233635296

[13]   Schneider, G. A., & Heyer, V. (1999). Influence of the electric field on Vickers indentation crack growth in BaTiO3. Journal of the European Ceramic Society, 19(6-7), 1299-1306.

[14]   Sun, X., Su, Y. J., Gao, K. W., Guo, L. Q., Qiao, L. J., Chu, W. Y., & Zhang, T. Y. (2011). Surface Potential Distribution in an Indentation-Pre-Cracked BaTiO3 Single Crystal. Journal of the American Ceramic Society, 94(12), 4299-4304.

[15]   Engert, A. R., Felten, F., Jelitto, H., & Schneider, G. A. (2011). What do we know about surface charges on cracks in ferroelectric ceramics?. In IUTAM Symposium on Multiscale Modelling of Fatigue, Damage and Fracture in Smart Materials (pp. 9-20). Springer, Dordrecht.

[16]   Robinson, D.A. (1987). Failure modes in composite materials. Trident Scholar Project Report. MD: United States Naval Academy.

        Retrieved from https://apps.dtic.mil/dtic/tr/fulltext/u2/a182527.pdf

[17] Schulte, K. A., & Baron, C. (1989). Load and failure analyses of CFRP laminates by means of electrical resistivity measurements. Composites science and technology, 36(1), 63-76.

[18] Irving, P. E., & Thiagarajan, C. (1998). Fatigue damage characterization in carbon fibre composite materials using an electrical potential technique. Smart materials and structures, 7(4), 456.

[19] Thiagarajan, C., & Irving, P. E. (1994). In Service Damage Monitoring techniques in polymer composites. Proc of the Aerotech, 94.

[20] Schueler, R., Joshi, S. P., & Schulte, K. (2001). Damage detection in CFRP by electrical conductivity mapping. Composites Science and Technology, 61(6), 921-930.

[21] Todoroki, A., & Tanaka, Y. (2002). Delamination identification of cross-ply graphite/epoxy composite beams using electric resistance change method. Composites Science and Technology, 62(5), 629-639.

[22] Wang, X., & Chung, D. D. L. (1997). Sensing delamination in a carbon fiber polymer-matrix composite during fatigue by electrical resistance measurement. Polymer Composites, 18(6), 692-700.

[23] Wang, X., & Chung, D. D. L. (1996). Continuous carbon fibre epoxy-matrix composite as a sensor of its own strain. Smart materials and structures, 5(6), 796.

[24] Prakash, R., & Owston, C. N. (1976). Eddy-current method for the determination of lay-up order in cross-plied crfp laminates. Composites, 7(2), 88-92.

[25] Prabhakaran, R. (1990). Damage assessment through electrical resistance measurement in graphite fiber-reinforced composites. Experimental Techniques, 14(1), 16-20.

[26] Louis, M., Joshi, S. P., & Brockmann, W. (2001). An experimental investigation of through-thickness electrical resistivity of CFRP laminates. Composites science and technology, 61(6), 911-919.

[27] Abry, J. C., Bochard, S., Chateauminois, A., Salvia, M., & Giraud, G. (1999). In situ detection of damage in CFRP laminates by electrical resistance measurements. Composites Science and Technology, 59(6), 925-935.

[28]   Glass, R. C., Taylor, S. R., Cahen, G. L., & Stoner, G. E. (1987). Electrochemical impedance spectroscopy as a method to nondestructively monitor simulated in-service damage in a carbon fiber reinforced plastic. Journal of Nondestructive evaluation, 6(4), 181-188.

[29]   Bekas, D. G., & Paipetis, A. S. (2016). Damage monitoring in nanoenhanced composites using impedance spectroscopy. Composites Science and Technology, 134, 96-105.

[30]   Fazzino, P. D., Reifsnider, K. L., & Majumdar, P. (2009). Impedance spectroscopy for progressive damage analysis in woven composites. Composites Science and Technology, 69(11-12), 2008-2014.

[31]   Raihan, R., Adkins, J. M., Baker, J., Rabbi, F., & Reifsnider, K. (2014). Relationship of dielectric property change to composite material state degradation. Composites Science and Technology, 105, 160-165.

[32]   Reifsnider, K., Raihan, M. R., & Vadlamudi, V. (2016). Heterogeneous fracture mechanics for multi-defect analysis. Composite Structures, 156, 20-28.

[33]   Majumdar, P., Bhuiyan, Y., Clifford, J., Haider, F., & Reifsnider, K. (2015). Multi-physical description of material state change in composite materials. Proceedings SAMPE, Baltimore, 18-21.

[34]   Majumdar, P. K., Faisal,H. M., & Reifsnider, K. (2013). Multi-physics response of structural composites and framework for modeling using material geometry. In 54th AIAA/ASME/ASCE/AHS/ASC Structures, Structural Dynamics, and Materials Conference (p. 1577).

[35]   Majumdar, P., Wilkes, C., Katiyar, P., & Arnold, A. (2017). Effect of Interfacial Defects on Mechanical and Electrical Properties of Composite Materials Fatigue. Proceedings of American Society for Composites, West Lafayette

[36]   Banerjee, P. K., Elenchezhian, M. R. P., Vadlamudi, V., Raihan, R., & Reifsnider, K. (2017). Predicting Adhesive Bond Performance Based on Initial Dielectric Properties. Proceedings of American Society for Composites, West Lafayette

Chapter 3 Multiphysics Modeling of Heterogeneity in Composites

3.1 Background

In Chapter 2, a review of electrical methods to monitor the structural integrity of composites was presented. Electrochemical impedance spectroscopy (EIS) and broadband dielectric spectroscopy (BbDS) techniques were shown to have the advantage over traditional electrical resistance measurement methods which explicitly need conducting matrix/fiber properties to measure the change in response with damage. The heart of the EIS and BbDS techniques lies in the heterogeneity of the material system that results in the accumulation and redistribution of charges leading to change in the global response based on local events. In this chapter, first the working principle of the BbDS technique followed by interpretation and normalization of the measured permittivity is discussed. This is followed by discussion of a micromechanics model that models the polarization in composites. A micromechanics model to estimate the effective lamina properties (mechanical and dielectric) is discussed and is used as a basis for the multiphysics finite element based model to simulate specific BbDS details.

3.2 Measuring Dielectric State Variables using Broadband Dielectric Spectroscopy

The dielectric constant of a material can be measured using different techniques limited by the frequency at which the measurements are to be made. In this work, the complex permittivity is measured using the parallel plate capacitor technique. The setup is shown below in Figure 3.1. The dielectric material (laminate) is sandwiched between two conductive plates (electrodes) to form this setup. A sinusoidal voltage is input though one electrode and the output current is measured through the other electrode which could be in phase or out of phase with the input voltage signal based on the nature of the material. The dielectric constant of the sample is calculated based on relations given below [1].
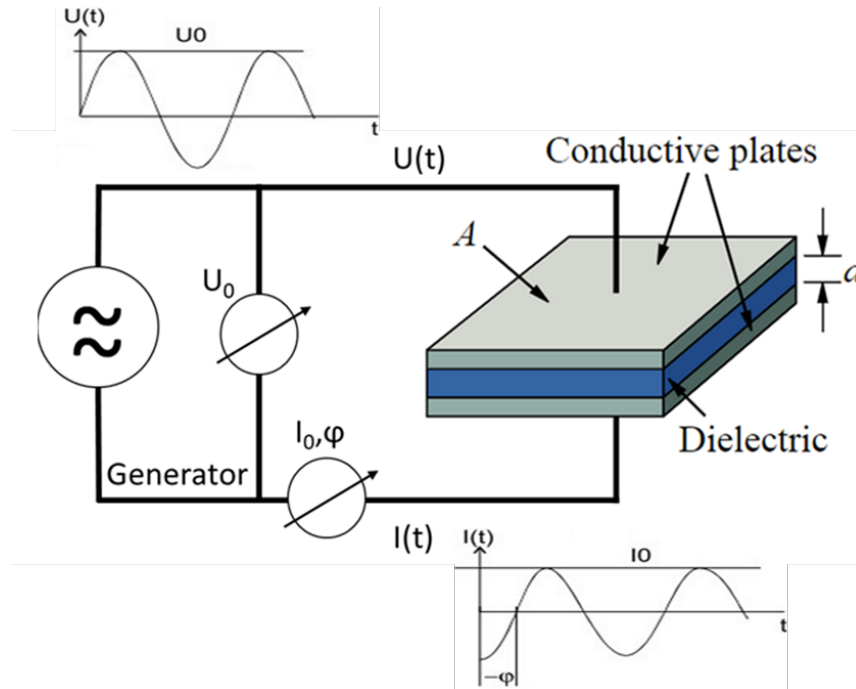
Figure 3.1 Working principle of broadband dielectric spectroscopy

A voltage $U_0(V)$ with a fixed frequency $(\omega/2\pi)$ is applied to the sample that causes a current $I_0(A)$ at the same frequency but with a phase shift(φ). The relation between them can be expressed in complex notation by the relations shown below:

$$U(t) = U_0 \cos(\omega t) = Re(U^* e^{j\omega t}) \tag{3.1}$$

$$I(t) = I_0 \cos(\omega t + \varphi) = Re(I^* e^{j\omega t}) \tag{3.2}$$

Where $U^* = U_0$ and $I^* = I' + jI''$ is the complex representation of the current caused by the applied voltage. The magnitude of this current is given by $I_0 = \sqrt{I' + I''}$. The measured impedance and capacitance of the sample is given by:

$$Z^*(\omega) = Z' + jZ'' = \frac{U^*}{I^*} \tag{3.3}$$

$$C^*(\omega) = C' + jC'' = \frac{1}{j\omega Z^*} \tag{3.4}$$

26

Where $Z'(\Omega), Z''(\Omega), C'(F), C''(F)$ are the real and imaginary parts of measured impedance $Z^*(\Omega)$ and capacitance $C^*(F)$ respectively. The dielectric constant of the sample is given by:

$$\varepsilon_r^*(\omega) = \varepsilon_r' + j\varepsilon_r'' = \frac{C^*}{C_0} \tag{3.5}$$

$$C_0 = \varepsilon_0 \frac{A}{d} \tag{3.6}$$

Where $\varepsilon_r', \varepsilon_r''$ are the real and imaginary parts of measured complex dielectric constant ε_r^* and $C_0(F)$ is the capacitance of free space, $\varepsilon_0(F/m)$ is the permittivity of free space, $A(m^2)$ is the area of the electrodes, $d(m)$ is the distance between the electrodes (thickness of the laminate).

3.3 Interpretation of the Measured Dielectric State Variable

In the previous section, the principle of measuring the dielectric state variable was presented. It can be observed that the measured dielectric state variable is dependent on the area A of the electrodes. Hence, as a best practice it is advised to use the same electrode configuration to measure the dielectric data of the sample being monitored. The question is how one can interpret the value of this variable? The effective way is to normalize the data w.r.t to initial dielectric data to understand the change in material state. To better understand, consider a material system as shown in Figure 3.2. In the initial state, the material comprises of some manufacturing defects and the initial dielectric constant of the as manufactured system is obtained. Under the application of a field (mechanical/electrical/thermal etc.) defects (cracks) develop in the material system. In the current state, the dielectric constant is obtained. Based on the theory of interfacial polarization, the creation of these new surfaces (cracks) would lead to charge accumulation and hence to a net increase in the measured dielectric constant with reference to the initial state of the material. The normalized value with respect to the initial state would give a representation of the intensity of damage.
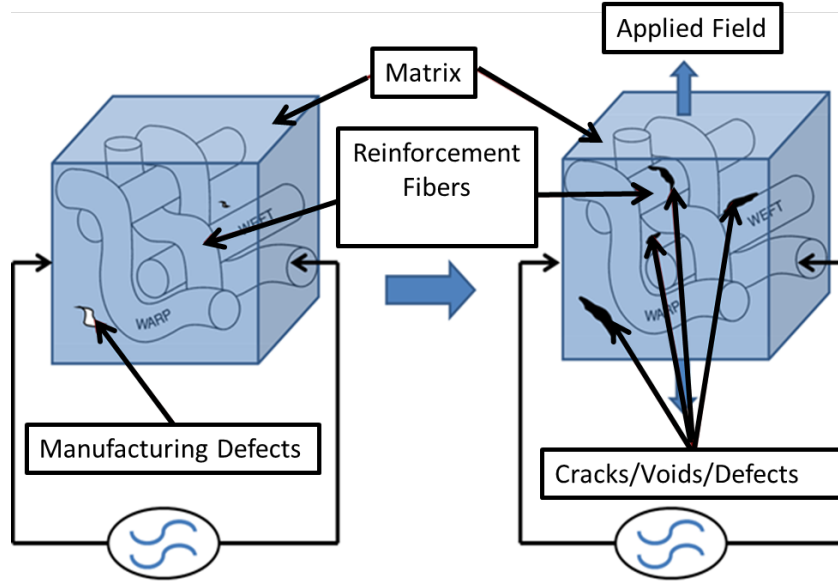
Figure 3.2 Different material states for interpretation of the dielectric state variable

3.4 Modeling the Dielectric Response of a Material System

The working principle and the interpretation of the dielectric state variable has been discussed above. In this section, the governing partial differential equation (PDE) of the dielectric response is derived. The response can be categorized based on how one considers the flow of current in the material system. The basis for the governing equations are the Maxwell's' equations as shown below [2].

$$\nabla.\mathrm{D} = \rho_v \tag{3.7}$$

$$\nabla.\mathrm{B} = 0 \tag{3.8}$$

$$\nabla \times \mathrm{E} = -\frac{\partial \mathrm{B}}{\partial t} \tag{3.9}$$

$$\nabla \times \mathrm{H} = \frac{\partial \mathrm{D}}{\partial t} + J \tag{3.10}$$

Where $\mathrm{B(T)}$ is the magnetic flux density, $H(\mathrm{A/m})$ is the magnetic field, $J(\mathrm{A/m^2})$ is the conduction current density and $\frac{\partial \mathrm{D}}{\partial t}(\mathrm{A/m^2})$ is the net displacement current density due to

28

polarization mechanisms. For clarity please refer to Section 2.3 of Chapter 2. Eq. (3.7) is the conservation of charge equation that states that the divergence of the net electric field over any region is equal to the net amount of charge in the region. The net electric field is given by eq. (2.8) as shown below

$$D = \varepsilon_0 \varepsilon_r E$$

and $E(V/m)$ is defined as the gradient of the electric potential $\emptyset(V)$ as shown below

$$E = -\nabla\emptyset \qquad (3.11)$$

Substituting eq. (2.8) and eq. (3.11) yields the electrostatic governing equation of the dielectric response as shown below.

$$-\nabla.(\varepsilon_0 \varepsilon_r \nabla\emptyset) = \rho_v \qquad (3.12)$$

ρ_v is the source term in the governing equation. If one assumes that $\rho_v = 0$ and since $\varepsilon_0 (F/m)$ is a constant, eq. (3.12) indicates that the product of the dielectric constant ε_r and the gradient of the potential $\nabla\emptyset$ in the region has to be constant in the volume. In simple words, variation in ε_r will create a gradient in potential and conversely a gradient in the potential in a region indicates difference in ε_r of the region.

Similarly considering the Maxwell's-Ampere's equation (current conservation equation), eq. (3.10) and taking the divergence of the equation we obtain eq. (3.13) based on the identity, 'divergence of the curl is zero'.

$$\nabla.(\frac{\partial D}{\partial t} + J) = 0 \qquad (3.13)$$

On further simplifying we obtain,

$$\frac{\partial (\nabla.D)}{\partial t} + \nabla.J = 0 \qquad (3.14)$$

Also $(\nabla.D) = \rho$, so we obtain another form of continuity equation as shown below

$$\nabla.J = -\frac{\partial \rho}{\partial t} \qquad (3.15)$$

Eq. (3.13) is the current conservation equation which states that in a given volume the net current entering the volume is equal to the net current leaving the volume. Eq. (3.15) states that the divergence of the conduction current is equal to the net dielectric current produced by the displacement of charges due to time varying displacement electric fields. In simpler words, if divergence is positive; the flux is directed outwards, conduction current is leaving the volume (decreasing in the volume) i.e. leaking, indicates that the net dielectric current is decreasing in the volume, i.e. the charges are dissipating. Similarly, if the divergence is negative; the flux is directed inwards, conduction current is entering the volume (increasing in the volume) i.e. storing, indicates that the net dielectric current is increasing in the volume, i.e. the charges are accumulating inside the volume.

As discussed above, the current inside the volume can be decomposed into conduction current and dielectric current as in eq. (3.13) (the basis of Maxwell-Ampere's equation). The conduction current is derived from the Ohm's law and is given by the equation

$$J = \sigma E \qquad (3.16)$$

Where $\sigma(S/m)$ is the electrical conductivity (inverse of resistivity) of the material. Substituting eq. (3.16) and eq. (2.8) in eq. (3.13), we obtain

$$\nabla.\left(\frac{\partial (\varepsilon_0 \varepsilon_r E)}{\partial t} + \sigma E\right) = 0 \qquad (3.17)$$

On applying a time harmonic electric field $E = E_0 e^{jwt}$, and assuming that the dielectric constant ε_r varies only spatially and doesn't vary time harmonically; on simplifying we obtain

$$\nabla \cdot ((jw\varepsilon_0\varepsilon_r + \sigma)E) = 0 \qquad (3.18)$$

Substituting $E = -\nabla\emptyset$ in eq. (3.18) we obtain the governing equation

$$-\nabla \cdot ((jw\varepsilon_0\varepsilon_r + \sigma)\nabla\emptyset) = 0 \qquad (3.19)$$

The physical interpretation of eq. (3.19) is, the product of net conductivity $(jw\varepsilon_0\varepsilon_r + \sigma)$ and the gradient in potential $\nabla\emptyset$ has to be constant. In simple words, if the net conductivity changes in the region, it induces a potential gradient and conversely if there exists a potential gradient in a region, it indicates the net conductivity is different in the region.

Eq. (3.12) and eq. (3.19) are the governing second order PDE's of the dielectric response (conservation of charge and conservation of current respectively). The aim is to solve for the potential $\emptyset$, prescribed by the boundary conditions

$$\emptyset(x, y, z)_{top\ electrode} = 1\ V \qquad (3.20)$$

$$\emptyset(x, y, z)_{bot\ electrode} = 0\ V \qquad (3.21)$$

Commercial FEA tool COMSOL Multiphysics© has the governing equations inbuilt in the AC/DC module. It has both the electrostatics interface (conservation of charge) and electric currents interface (conservation of current) to solve for the potential $\emptyset$. Once the potential $\emptyset$ is solved, we can obtain the gradient in potential $\nabla\emptyset$ and the net current density $((jw\varepsilon_0\varepsilon_r + \sigma)\nabla\emptyset)$ at each material point. The parameters such as impedance, capacitance and the complex permittivity can then be calculated based on eq.'s (3.3-3.6).

3.5 Simulation of the Dielectric Response in a Heterogeneous Material System

In the above section, derivation of the governing equations for modeling the dielectric response is presented. In this section we simulate the dielectric response in commercial FEA software COMSOL Multiphysics$^©$. As discussed, dielectric response can be simulated based on charge conservation and current conservation. In charge conservation, dielectric constant ε_r is the driving factor where as in current conservation, the combination of conductivity $\sigma(S/m)$ and dielectric constant ε_r are the driving factors. We will discuss both of the models in detail below.

Consider a 2D representative volume element (RVE) with one inclusion as shown below in Figure 3.3. The RVE dimensions are 10µm×10µm with an inclusion diameter of 5µm. We consider three cases, case (a) the inclusion properties are same as the surrounding bulk material properties, case (b) the inclusion is more conductive then the surrounding bulk material and case (c) the inclusion is more insulative then the surrounding bulk material. Case (a) is a homogeneous material system whereas case (b) and (c) is a heterogeneous material system. The properties of the bulk material and the inclusion are provided in Table 3.1 below.
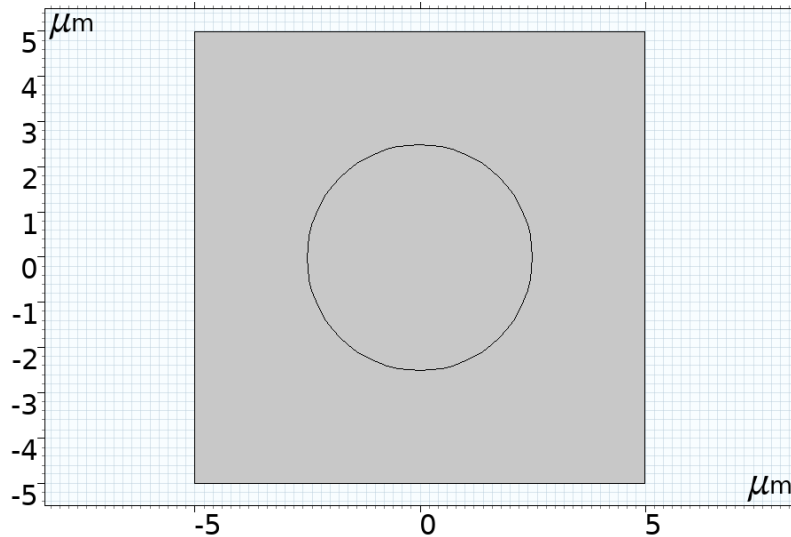
Figure 3.3 Representative volume element (RVE) with one inclusion

Table 3.1 RVE constituent dielectric properties

Entity		Dielectric constant $\varepsilon_r (units)$	Conductivity $\sigma(S/m)$
Case (a)	Bulk material	3.15	1E-14
Homogeneous	Inclusion	3.15	1E-14
Case (b)	Bulk material	3.15	1E-14
Heterogeneous	Inclusion	1	1E6
Case (c)	Bulk material	3.15	1E-14
Heterogeneous	Inclusion	1.005	1E-15

The finite element mesh and the boundary conditions are shown below in the Figure 3.4. The interface between inclusion and the bulk material was discretized with more elements as it is the region of importance. A voltage of $1(V)$ is applied on the top along the line $y = 5$ and the other end of the RVE is grounded at $y = -5$ as shown in Figure 3.4. To model the accurate response, periodic conditions were enforced by the boundary condition $V_{src} = V_{dst}$.
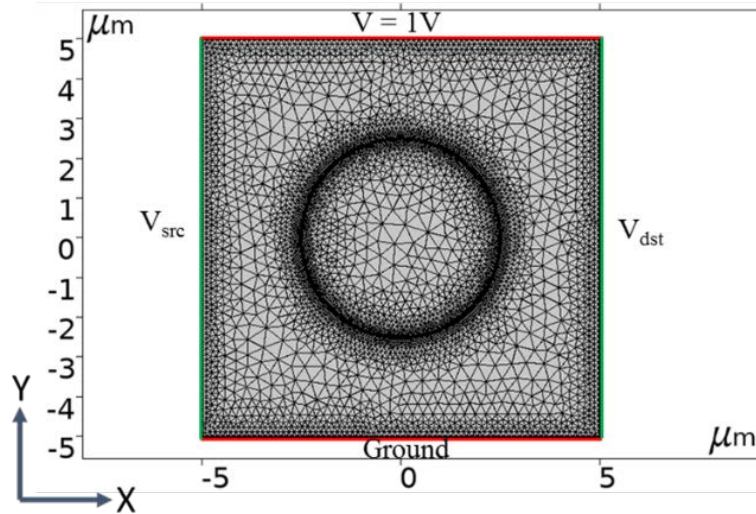
Figure 3.4 Finite element mesh with boundary conditions

3.5.1 Simulation using charge conservation

The governing equation for charge conservation Eq. (3.12) is only dependent on dielectric constant ε_r and as per the governing equation, the product of the permittivity and the gradient in potential has to be constant. This can be observed in the simulation results discussed below.

For case (a) where the inclusion has the same properties as the bulk material the potential distribution is uniform as shown in Figure 3.5 (a). For case (b) with the conductive inclusion it can be observed that the potential distribution is no longer uniform and the potential lines bend into the inclusion indicating there is more charge accumulation in the inclusion as shown in Figure 3.5 (b). However, the distribution doesn't make sense because there can be no electric field inside a conductor. This is observed because ε_r value for metal is considered as 1 and hence as per eq. (3.12) the decrease in permittivity in the volume (inclusion) is compensated by an increase in gradient of potential in the inclusion resulting in higher electric field with in the inclusion. However, as per eq. (3.12) for the electric field to be 0 inside the inclusion the ε_r value should be ∞ (a very large value) as indicated by various theories [3]. Hence, using a larger value (1000) it can be observed that the potential lines bend over the inclusion indicating charge accumulation along the surface of the inclusion which is the ideal behavior with a conductor inclusion as shown in Figure 3.5 (c). For case (c) the behavior described for the conductive inclusion with ε_r value of 1 for the inclusion is observed as shown in Figure 3.5 (d). The potential variation along the line $x = 0$ for all the models is shown in Figure 3.5 (e).
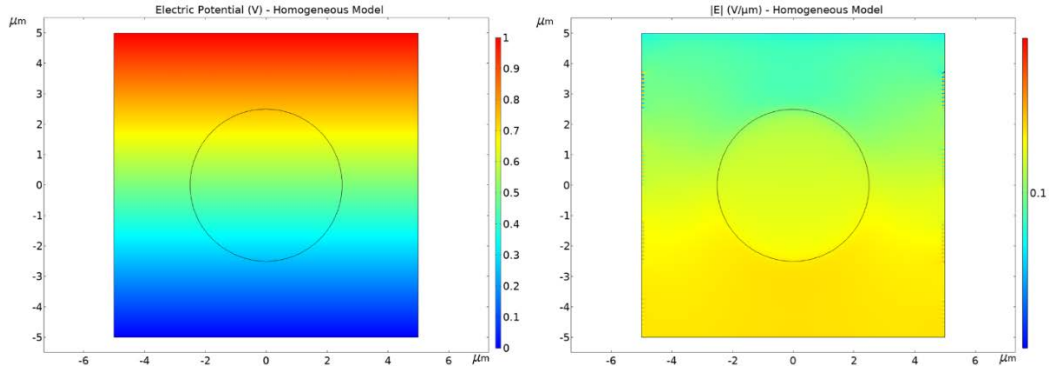
(a)
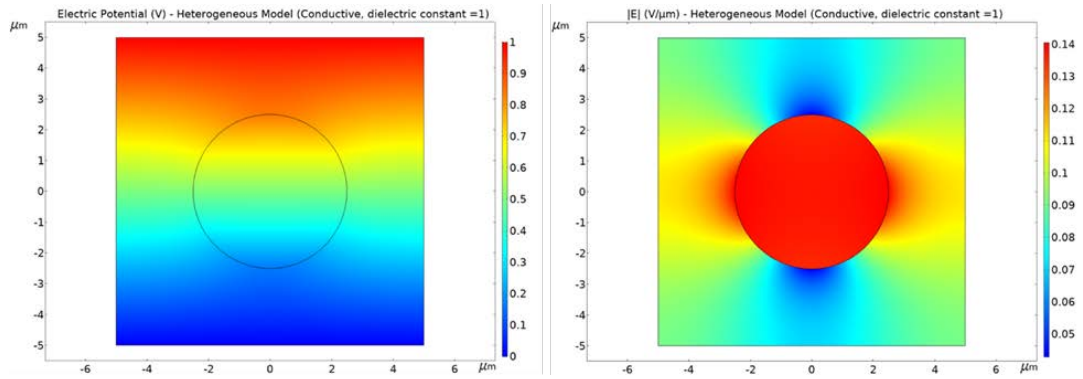
(b)
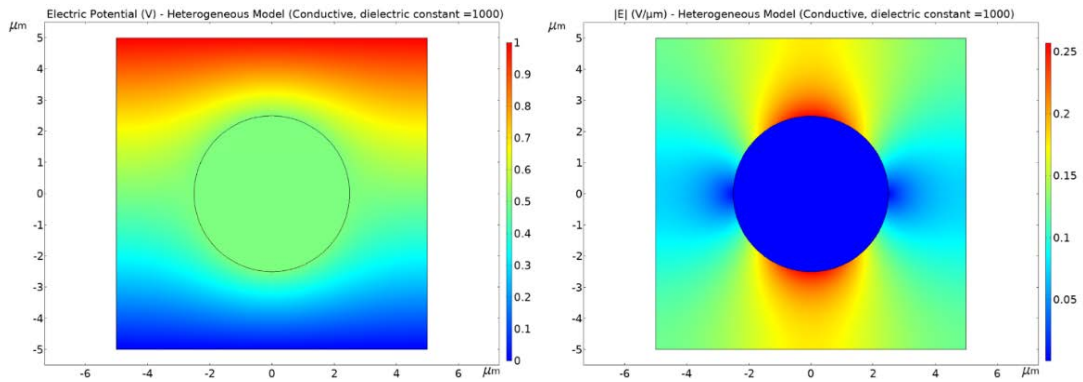
(c)

(d)
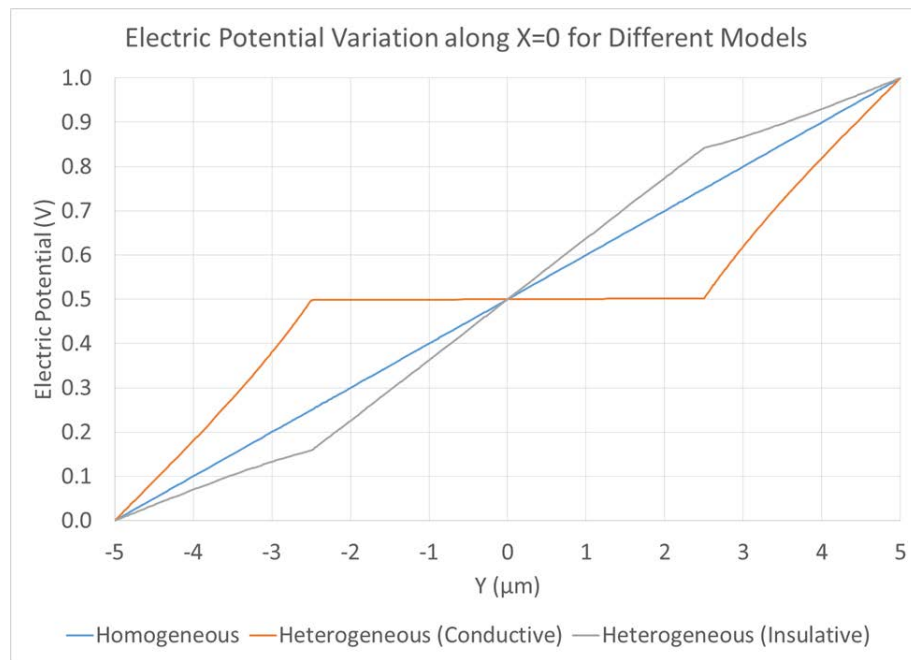
(e)

Figure 3.5 Electric potential distribution (left) and electric field distribution (right) for (a) Homogeneous model, (b) Heterogeneous (conductive) model with $\varepsilon_r = 1$,(c) Heterogeneous (conductive) model with $\varepsilon_r = 1000$, and (d) Heterogeneous (insulative) model. (e) Electric potential variation along $x = 0$ for different models

3.5.2 Simulation using current conservation

In the above section, the simulation results were discussed with charge conservation. In this section we discuss the simulation results with current conservation. The governing equation for current conservation Eq. (3.19) is dependent on dielectric constant ε_r and the conductivity σ.

36

As per the governing equation, the product of the net conductivity and the gradient in potential has to be constant.

For case (a) where the inclusion has the same properties as the bulk material the potential distribution is uniform as shown in Figure 3.6 (a). For case (b) the conductive inclusion it can be observed that the potential distribution is no longer uniform and the potential lines bend over the inclusion indicating there is charge accumulation over the inclusion as shown in Figure 3.6 (b). However, the distribution isn't symmetric, that is all the potential drop occurs before the inclusion which is not the ideal response. This is observed because the ratio of conductivities of the inclusion and the bulk material is 10^{20}, which causes the numerical issues and is purely a solver error rather than a physical phenomenon. To resolve this, the conductivity of the inclusion was changed to $\sigma = 1\,S/m$ which still maintains the heterogeneity of the system (ratio of conductivities is 10^{14}) and this made the distribution symmetric as shown in Figure 3.6 (c). For case (c) the behavior described in the charge conservation model with an insulative inclusion can be observed as shown in Figure 3.6 (d). The potential variation along the line $x = 0$ for all the models is shown in Figure 3.6 (e). These correspond close to observations made in [12].

(a)

Electric Potential (V) - Heterogeneous Model (Conductive, σ =1E6 S/m) @ 1MHz

|E| (V/μm) - Heterogeneous Model (Conductive, σ =1E6 S/m) @ 1MHz

(b)

Electric Potential (V) - Heterogeneous Model (Conductive, σ =1 S/m) @ 1MHz

|E| (V/μm) - Heterogeneous Model (Conductive, σ =1 S/m) @ 1MHz

(c)

Electric Potential (V) - Heterogeneous Model (Insulative) @ 1MHz
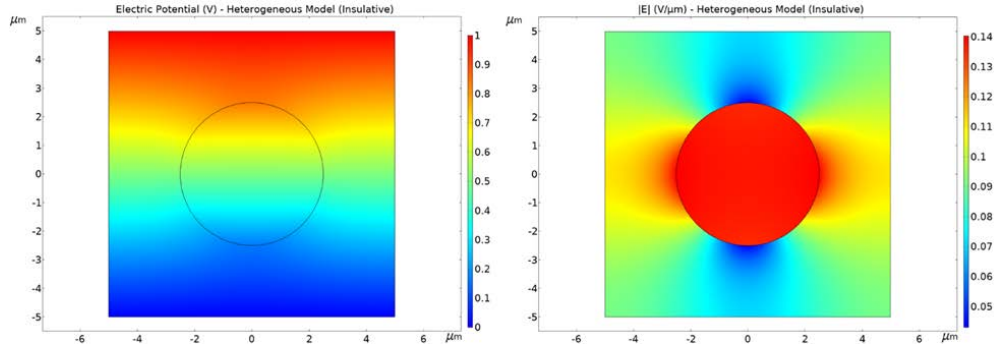
|E| (V/μm) - Heterogeneous Model (Insulative) @ 1MHz

(d)

(e)
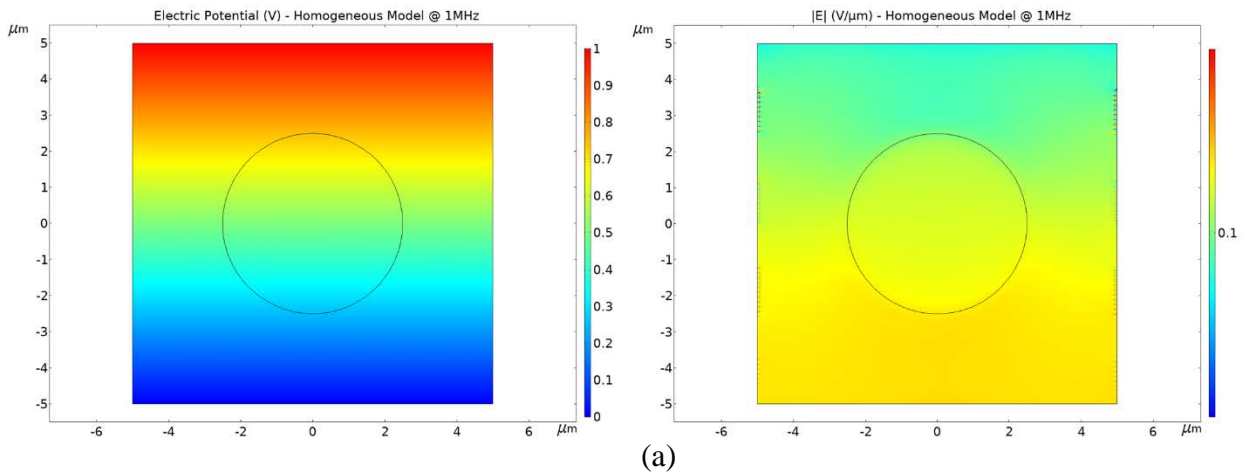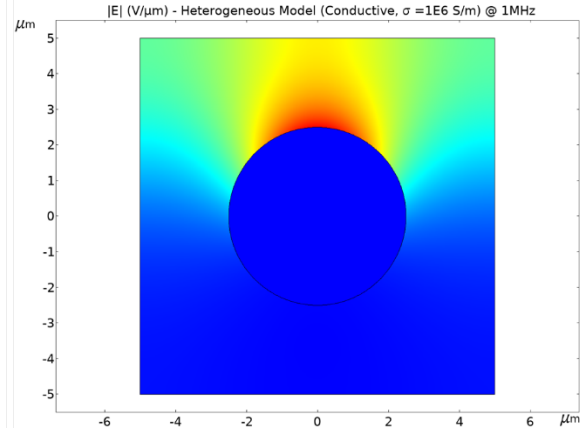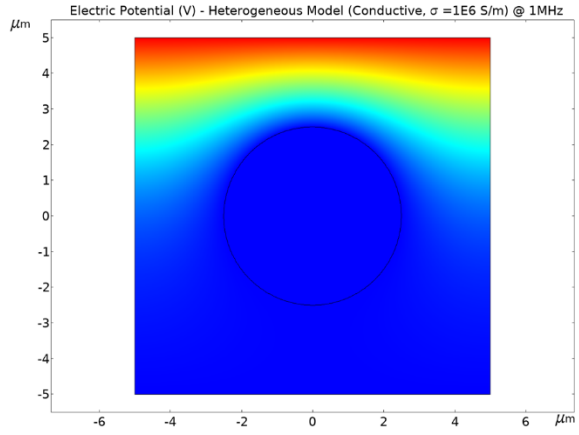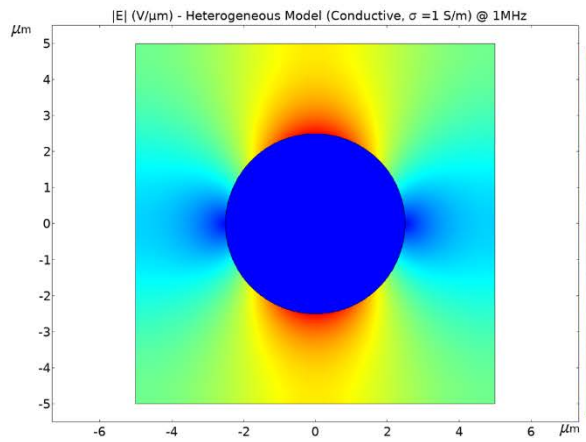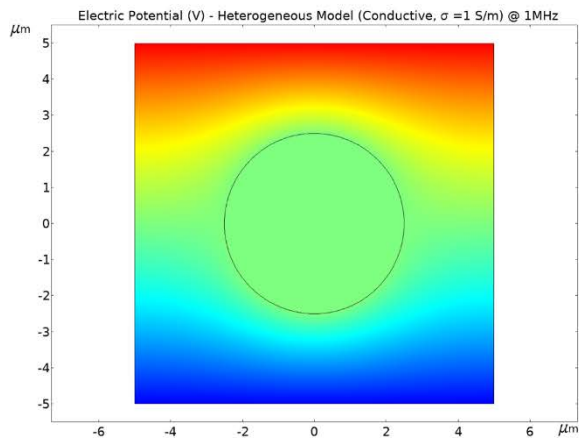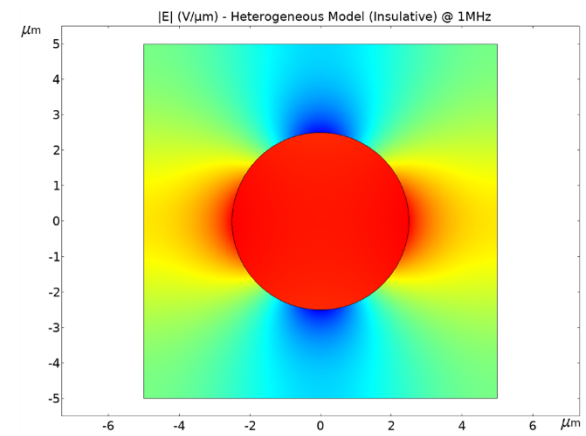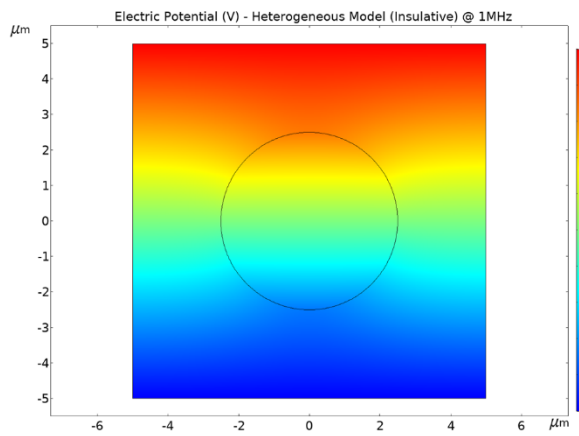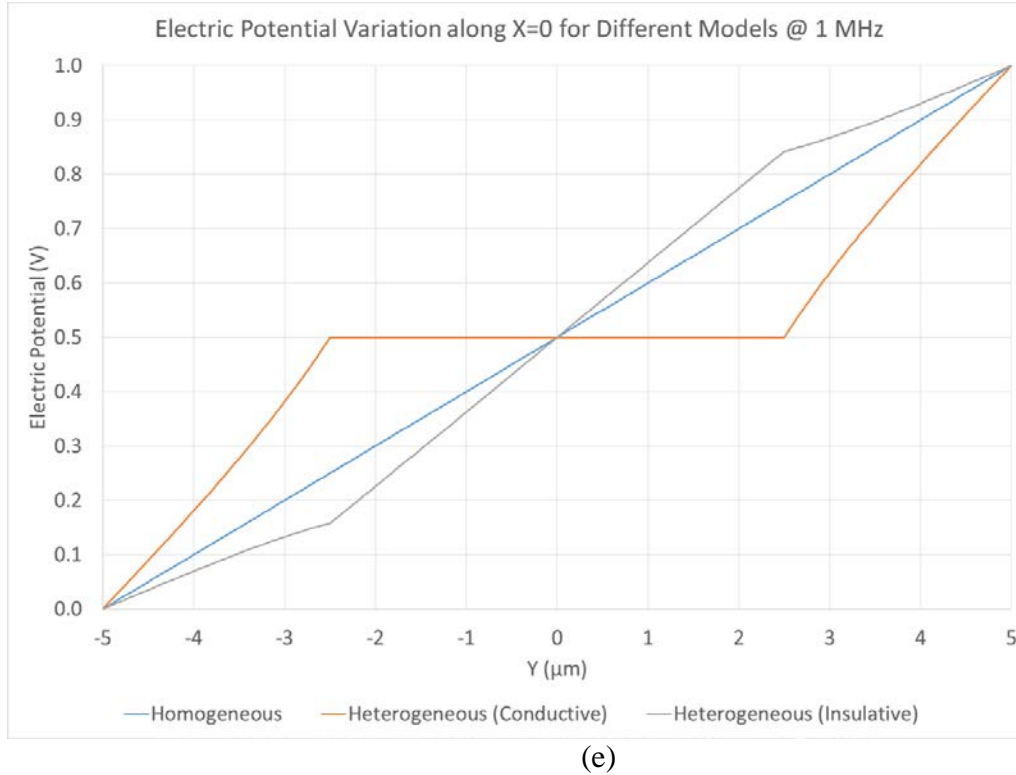
Figure 3.6 Electric potential distribution (left) and electric field distribution (right) @ 1MHz for (a) Homogeneous model, (b) Heterogeneous (conductive) model with $\sigma = 1E6\ S/m$, (c) Heterogeneous (conductive) model with $\sigma = 1\ S/m$, and (d) Heterogeneous (insulative) model. (e) Electric potential variation along $x = 0$ for different models

From the simulation results using charge conservation and current conservation principles it can be observed that the behavior is identical. The only difference is in the charge conservation model, it is assumed that the charges are stationary (steady state/after effects); where as in current conservation the charges are displaced by the time varying electric field. However, for the multiphysics simulations the current conservation principle will be used as it is much closer to reality and deals with displacement of charges during damage development which triggers a global variation in the dielectric state variable.

3.6 Effective Properties of the Heterogeneous Material System

In the above section, the simulation of dielectric response was discussed for a heterogeneous material system at the micromechanics level. However, at the global scale the

properties are orthotropic in nature and no longer deal with constituent properties but instead depend on the fiber orientations. Hence it is important to predict the orthotropic material properties (mechanical and dielectric) to simulate the multiphysics response. The main focus of this section is to discuss the effective dielectric properties based on various models and theories and compare them with the effective properties predicted using a finite element model.

3.6.1 Dielectric mixture theories

In the above section, the simulation of dielectric response was discussed for a heterogeneous material system at the micromechanics level. However, at the global scale the properties are orthotropic in nature and no longer deal with constituent properties but instead depend on the fiber orientations. Various theories have been proposed to find the effective dielectric properties of heterogeneous systems. However, the limiting values of the effective properties can be based on how the constituent phases interact with the applied electric field E which alters the net electric displacement field D. The lower bound comes from assuming that the net electric displacement field is uniform in both the constituents whereas the upper bound comes from assuming that the applied electric field is constant known as the Wiener bounds [4].

$$\varepsilon = (1 - V_i)\varepsilon_m + V_i\varepsilon_i \tag{3.22}$$

$$\frac{1}{\varepsilon} = \frac{1 - V_i}{\varepsilon_m} + \frac{V_i}{\varepsilon_i} \tag{3.23}$$

Where ε is the effective dielectric constant, V_i is the volume fraction of the inclusion, ε_m is the dielectric constant of the bulk material, and ε_i is the dielectric constant of the inclusion. The effective dielectric constant of the heterogeneous system cannot be greater than the upper bound given by Eq. (3.22) and cannot be lesser than the lower bound given by Eq. (3.23). Another common theory used most often is the Maxwell-Garnett approximation [5] given by

$$\varepsilon = \varepsilon_m \frac{\varepsilon_m(1 - V_i)(1 - A) + \varepsilon_i(V_i + A(1 - V_i))}{\varepsilon_m + A(1 - V_i)(\varepsilon_m - \varepsilon_i)} \tag{3.24}$$

Where A is the depolarization factor for different inclusion shapes. For spheres $A = \frac{1}{3}$, cylinders $A = \frac{1}{2}$ [6]. Another famous approximation using mixture theories is the Raleigh approximation [7] given by

$$\frac{\varepsilon - \varepsilon_m}{\varepsilon + \varepsilon_m} = V_i \frac{\varepsilon_i - \varepsilon_m}{\varepsilon_m + \varepsilon_i} \tag{3.25}$$

Several other models that are used for calculating the effective dielectric properties are mentioned in the references [8-10].

3.6.2 Effective properties using finite element model

In the above section, different approximate theories for calculating the effective dielectric properties of the heterogeneous material system were reviewed. In this section, FEM is used to predict the effective dielectric properties. Two models are considered, case (a) single fiber RVE case (b) hexagonally packed fiber RVE case. The hexagonal packing of fibers will consider interaction of neighboring fibers hence providing realistic predictions. Both carbon fiber and glass fiber RVEs will be simulated and compared with the mixture theories. The constituent properties are tabulated below in Table 3.2 [11]. First the carbon fiber RVE model predictions will be discussed.

Table 3.2 Dielectric properties of the constituents

Constituent	Material	Dielectric Constant ε_r	Conductivity σ (S/m)
Matrix	Epoxy	3.15	1E-14
Fiber	Glass	6.2	1E-13
	Carbon	13.5	1

For the one fiber model, RVE block dimensions were 5.72μm×5.72μm×5.72μm with carbon fiber (diameter of 5μm) to obtain $V_i \approx 60\%$. The FEM and the boundary conditions are shown below in Figure 3.7.
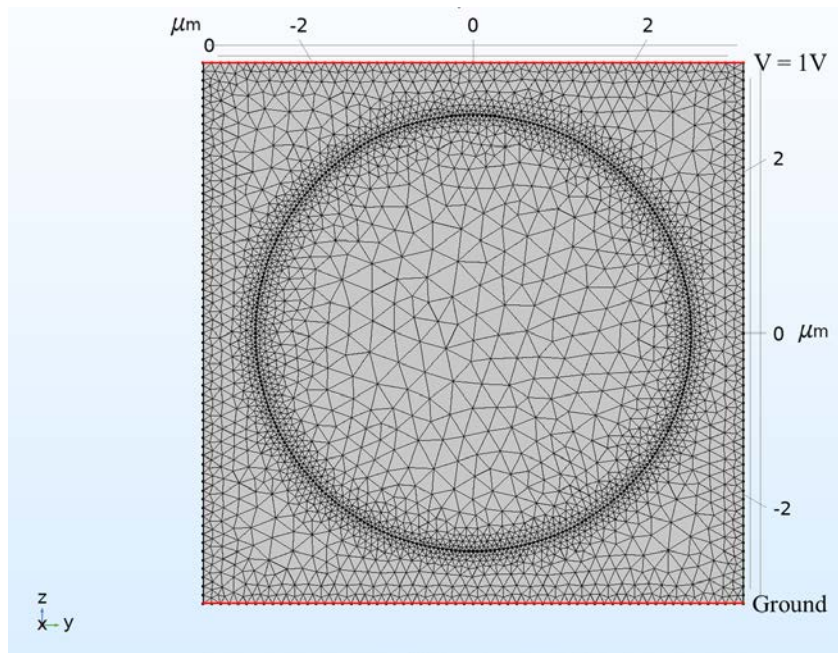
Figure 3.7 Finite element mesh and the boundary conditions of 1 fiber CFRP RVE

For the hexagonal fiber packing model, RVE block dimensions were 6.2μm×6.2μm×10.74μm with carbon fiber (diameter of 5μm) to obtain $V_i \approx 60\%$. The FEM and the boundary conditions are shown below in Figure 3.8.
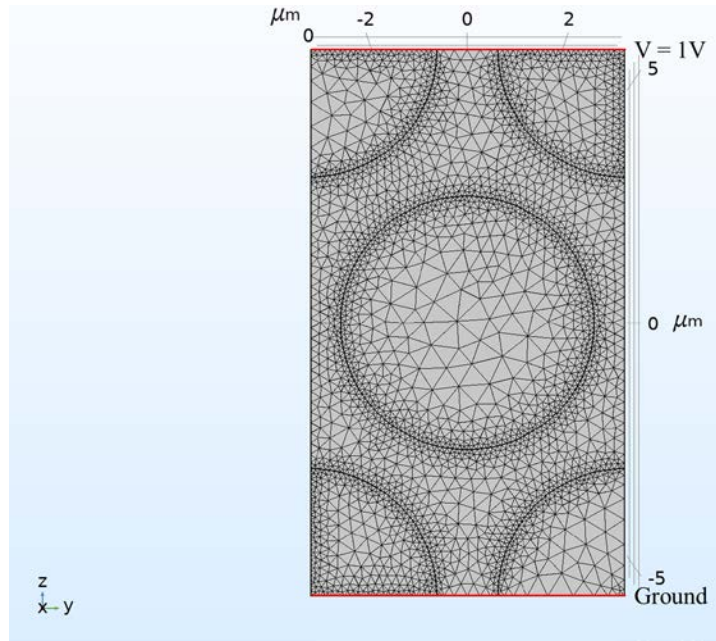
Figure 3.8 Finite element mesh and the boundary conditions of hexagonal packed CFRP RVE

The permittivity can be calculated using the relations below.

$$\varepsilon = \frac{C}{(\frac{\varepsilon_0 A}{d})} \tag{3.26}$$

$$\varepsilon = \frac{1}{j\omega \left(\frac{\varepsilon_0 A}{d}\right) Z^*} \tag{3.27}$$

Eq. (3.26) is used when charge conservation is used to simulate the dielectric response and Eq. (3.27) is used with current conservation. The predicted permittivity is tabulated below in Table 3.3

Table 3.3 Predicted permittivity values using various mixture theories and FEM for CFRP

Permittivity CFRP								
					FEM			
					1 Fiber RVE		Hexagonal RVE	
Experimental	Wiener upper bound	Wiener lower bound	Maxwell-Garnet	Raleigh	Eq. (3.26)	Eq. (3.27)	Eq. (3.26)	Eq. (3.27)
13±3	9.36	5.83	6.9	6.9	6.63	13.68	6.8	12.28

It can be observed that the predicted permittivity values based on mixture theories and FEM using charge conservation Eq. (3.26) are far off from the experimental data. The primary reason for this discrepancy is that the theories and the principle of charge conservation don't consider conductivity which plays an important role if the heterogeneity is significant. Hence, the predicted permittivity using current conservation Eq. (3.27) yield close predictions to experimental data.

The predictions for glass fiber RVE will be discussed below. For the one fiber model, RVE block dimensions were 17.162µm×17.162µm×17.162µm with glass fiber (diameter of 15µm) to obtain $V_i \approx 60\%$. For the hexagonal fiber packing model, RVE block dimensions were 18.45µm×18.45µm×31.95µm with carbon fiber (diameter of 15µm) to obtain $V_i \approx 60\%$. The boundary conditions are similar to the simulations with CFRP. The predicted permittivity is tabulated below in Table 3.4.

Table 3.4 Predicted permittivity values using various mixture theories and FEM for GFRP

Permittivity GFRP								
					FEM			
					1 Fiber RVE		Hexagonal RVE	
Experimental	Wiener upper bound	Wiener lower bound	Maxwell-Garnet	Raleigh	Eq. (3.26)	Eq. (3.27)	Eq. (3.26)	Eq. (3.27)
4.4±0.4	4.98	4.47	4.68	4.69	4.69	4.69	4.68	4.68

It can be observed that the predicted permittivity values based on mixture theories and FEM using charge conservation Eq. (3.26) and current conservation Eq. (3.27) are in close proximity to experimental data unlike CFRP predictions. The primary reason is that the heterogeneity in the dielectric sense is not too severe to cause error in predictions.

Another key point to be noted is that because of the anisotropic nature of composites, the permittivity and conductivity are no longer single values but are tensor values. The predictions obtained in the above section are through thickness measurements. Similarly, measurements can be made in the other orthogonal directions to build the dielectric property tensor. Also, it has to be noted that in the given work the tensor is a diagonal matrix i.e. no coupling terms would be included or in simpler terms an applied electric field in the Z direction induces current only in the Z direction. However in the practical sense there would be additional components that contribute to losses which are ignored in the current work and will be discussed in our future research plan.

In the next chapter, the experimental investigations of the insitu behavior of composites under uniaxial tension are studied for different material systems and stacking sequences. The observations will be discussed and the variation of the dielectric response will be correlated with material state changes.

3.7 References

[1]   Frequency domain measurement. Retrieved from

        https://www.novocontrol.de/php/intro_freq_domain.php

[2]   Maxwell, J. C. (1865). VIII. A dynamical theory of the electromagnetic field. Philosophical

        transactions of the Royal Society of London, (155), 459-512.

[3]   Rice, M. J., & Bernasconi, J. (1972). Frequency-dependent conductivity and dielectric constant of

        nearly-one-dimensional metallic conductors. Physics Letters A, 38(4), 277-278.

[4]   Wiener, O. (1912). Der Abhandlungen der Mathematisch-Physischen Klasse der Konigl.

        Sachsischen Gesellshaft der Wissenschaften, 32, 509-604.

[5]   Garnett, J. M. (1904). XII. Colours in metal glasses and in metallic films. Philosophical

        Transactions of the Royal Society of London. Series A, Containing Papers of a Mathematical or

        Physical Character, 203(359-371), 385-420.

[6]   Sillars, R. W. (1937). The properties of a dielectric containing semiconducting particles of various

        shapes. Journal of the Institution of Electrical Engineers, 80(484), 378-394.

[7]   Rayleigh, L. (1892). LVI. On the influence of obstacles arranged in rectangular order upon the

        properties of a medium. The London, Edinburgh, and Dublin Philosophical Magazine and Journal

        of Science, 34(211), 481-502.

[8]   Tuncer, E., Gubański, S. M., & Nettelblad, B. (2001). Dielectric relaxation in dielectric mixtures:

        Application of the finite element method and its comparison with dielectric mixture formulas.

        Journal of Applied Physics, 89(12), 8092-8100.

[9]   Krakovský, I., & Myroshnychenko, V. (2002). Modeling dielectric properties of composites by

        finite-element method. Journal of applied physics, 92(11), 6743-6748.

[10]   Bruggeman, V. D. (1935). Berechnung verschiedener physikalischer Konstanten von heterogenen

        Substanzen. I. Dielektrizitätskonstanten und Leitfähigkeiten der Mischkörper aus isotropen

        Substanzen. Annalen der physik, 416(7), 636-664.

[11]   Dielectric constant of different materials. Retrieved from

          http://www.clippercontrols.com/pages/Dielectric-Constant-Values.html

[12]   Baker, J., Adkins, J. M., Rabbi, F., Liu, Q., Reifsnider, K., & Raihan, R. (2014). Meso-design of

          heterogeneous dielectric material systems: Structure property relationships. Journal of Advanced

          Dielectrics, 4(02), 1450008.

Chapter 4 In-Situ Monitoring of Material State in Composites

4.1 Background

In Chapter 3, governing equations for modeling the dielectric response of composites were derived. Predictions of the effective dielectric properties of composites were made using a finite element model and were compared to dielectric mixture theories. In this chapter, at first the experimental setup for in-situ monitoring of material state is discussed followed by selection of material systems and stacking sequences. The variation in dielectric response will be correlated with damage mechanisms and validated through edge replications of the damaged coupon. Finally, a basis for multiphysics modeling of material state will be established which will be explored in detail in the next chapter.

4.2 Experimental Setup for In-Situ Monitoring of Material State

4.2.1 Uni-axial tensile loading setup

The test specimens are loaded in uni-axial tension using MTS™ landmark servo hydraulic test system equipped with a load cell capable of loading up to 50KN (±0.05 KN). Hydraulic wedge grips with tungsten carbide surface coating ensure adequate friction for firm gripping and load introduction into the specimen with exceptional repeatability. MTS™ multipurpose elite software provides an extremely powerful and flexible platform for creating and running tests and exporting data for analysis.

4.2.2 Dielectric characterization setup

In the current work, the material behavior is characterized by broadband dielectric spectroscopy (BbDS) using the Novocontrol™ alpha analyzer. The alpha analyzer measures the complex dielectric properties of the material system as a function of frequency of applied electric

field. The principle of measuring the dielectric properties was discussed in section 3.2 of chapter 3. The frequency range of the alpha analyzer is limited to (3µHz – 20MHz) with a phase accuracy of 0.002º and impedance range of ($10^{-3}\Omega$ - $10^{15}\Omega$) for the current work.

4.2.3 In-situ testing setup

Uniaxial tensile loading was applied using displacement control in the MTS™ test system. The rate of displacement was around 0.3 mm/min, the slow rate of loading was chosen in order to ensure distributed damage [1]. In the current work, strain was calculated by normalizing the actuator displacement with gage length of the specimen. It will be later observed that shape of the stress-strain curve was similar to one obtained by Raihan et al.[2], where a clip gage (extensometer) was used to measure the strain.

To perform insitu dielectric studies, the gage region of the coupon was placed between the electrode blocks to create a parallel plate capacitor arrangement. The blocks were clamped using a spring loaded clamp to ensure uniform electrode contact with the sample. The electrodes were connected to the analyzer of Novocontrol™ unit which measures the impedance, capacitance as a function of frequency with high precision. In the current work, a frequency of (10 Hz, 100 Hz) (for interfacial polarization) was used for the dielectric response in order to obtain low frequency response with a high sampling rate which is crucial to capture the change in material state. The schematic of the setup is shown in Figure 4.1 and the sample setup is shown below in Figure 4.2.
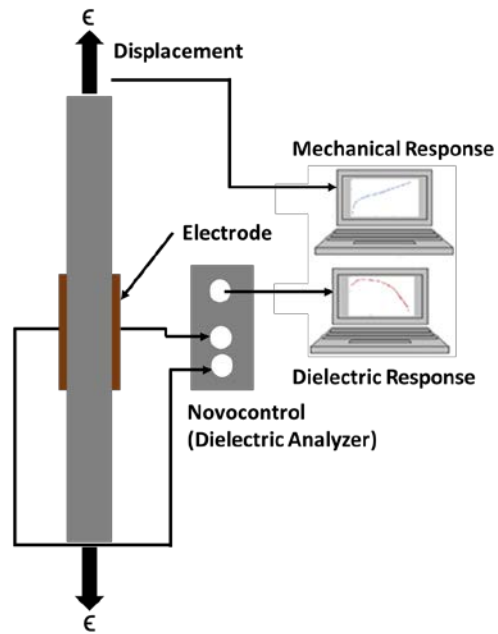
Figure 4.1Schematic of the insitu test setup

Figure 4.2 Insitu test setup

4.3 Consideration of Material Systems and Stacking Sequences

To obtain a better understanding of the damage mechanisms and their effect on the dielectric response certain stacking sequences were preferred.

Extensive literature is available on the damage progression of cross ply laminates $[0/90_n/0]$ and $[90/0_n/90]$ as these sequences result in extensive transverse cracking and hence a lot of studies were performed to understand the transverse crack spacing and stiffness reduction mechanisms in these laminates [3-4]. In the current work, we use $[90/0_2/90]$ laminates and monitor the material state change and correlate the variation in dielectric response with damage development.

Quasi isotropic laminates are preferred across various applications because of their higher in plane strengths. A lot of literature is available on the damage progression in these laminates in both uniaxial tension and fatigue [4]. In the current work $[-45/0/45/90]_s$ laminates are tested in uniaxial tension and the changes in dielectric response will be correlated with the damage mechanisms.

Off-axis laminates especially $[45/-45]_s$ which result in nonlinear shear behavior will be tested. For the above listed stacking sequences, glass fiber reinforced polymer matrix composites were manufactured.

4.4 Manufacturing of Composite Laminates

Unidirectional glass fiber reinforced polymer composites (Newport 301 epoxy resin/E-Glass fibers (volume fraction 55%)) and woven glass fiber reinforced polymer composites (Newport 301 epoxy resin/7781 E-Glass fabric (volume fraction 60%)) were manufactured as per the stacking sequence. This material system is well suited for structural applications in sporting goods, automobile bodies, marine (ship hulls), medical and industrial manufacturing. The laminate

panels were made using compression molding techniques where the temperature was ramped up at a rate of 3 °C/min from 21 °C to 135 °C, cured at 135 °C for 60 minutes and cooled at a rate of 3 °C/min from 135 °C to 49 °C, as per the manufacturer recommendations [5]. For woven composite laminates, 8 ply $[(0°)]_8$ laminae were stacked and cured with the same curing cycle mentioned above for the unidirectional laminates. Cured panels were cut into coupons as per ASTM D 3039 recommendations [6]. The samples were cut at 5 different orientations (0°, 30°, 45°, 60°, and 90°). A minimum of 3 samples were made for each of the described stacking sequence.

4.5 Material State Change and the Corresponding Variation of Dielectric State Variable

This section is the heart for understanding how the damage mechanisms result in variation of dielectric response. The damage mechanisms will be described in detail for the outlined stacking sequences and the corresponding variation of the dielectric state variable will be discussed in the later part of this section. Primarily evolution of damage in a general sense for a composite material will be discussed and an analytical understanding of how these damage mechanisms trigger a variation in the dielectric state variable will be presented.

In a general sense under uniaxial tensile loading, matrix damage is the primary mode of damage in these material systems. Matrix cracking initiates primarily at the free edge of the laminate at various locations along the length in the ply with the lowest transverse tensile strength. These cracks grow through the thickness of the ply and grow almost instantly across the width (depends on various factors such as current stress state of the ply, neighboring plies etc.) until they attain a saturation along the length of the specimen. This saturation state is often referred to as the characteristic damage state (CDS) in which there would be a significant drop in the stiffness of the laminate but not in the strength. This is then followed by creation of secondary cracks in the

neighboring plies due to the change in stress state triggered by the primary matrix cracks. The coupling of these cracks at the free edge induces edge delaminations which may or may not grow along the width of the specimen. These secondary cracks occur at various sites along the width and coupling of these secondary cracks and primary cracks in the interior of the laminate results in interior delaminations which result in local failure. Under continued loading, these secondary cracks tend to grow at a higher rate resulting in coalescence of delaminations and these locally failed regions find a path which then aided by fiber fractures leading to a sudden drop in the strength and final failure [7-8].

To understand the variation of dielectric response with damage mechanisms, let's recall the polarization mechanisms. Electronic, ionic and orientation polarization occur at high frequencies and relate to dipole moments generated by the realignment of bound charges in atoms and molecules. However there are charge carriers that are not bounded with in atoms or molecules and are free to migrate through the material. Given the dielectric nature of these material systems the inherent conductivity is very low. However, when a low frequency external electric field is applied these charges are displaced. During the damage events, new surfaces are created and these charge displacements are impeded by these newly created surfaces resulting in charge trapping and accumulation at these sites which is described as interfacial or space charge polarization. This accumulation of charges at these interfaces leads to increased charge storage (capacitance) of the system resulting in an increase in the permittivity ε_r of the material system. From the continuity equation (Eq. (3.15)) $\nabla . J = -\frac{\partial \rho}{\partial t}$, accumulation of charges inside the volume results in a positive $\frac{\partial \rho}{\partial t}$ which indicates $\nabla . J$ is negative which indicates current is entering the volume (increasing in the volume). If the current in the volume is increasing, this indicates that the impedance of the material system is reducing. These observations are consistent with the findings from Raihan et al.

53

[2] until the coupling of damage mechanisms start; they observed a decrease in ε_r during coupling shown below in Figure 4.3. From the above mentioned theory, the ε_r will monotonically increase even during coupling because of the generation of new surfaces during damage progression. However, it has to be noted that the role of delamination hasn't been considered in the above theory.
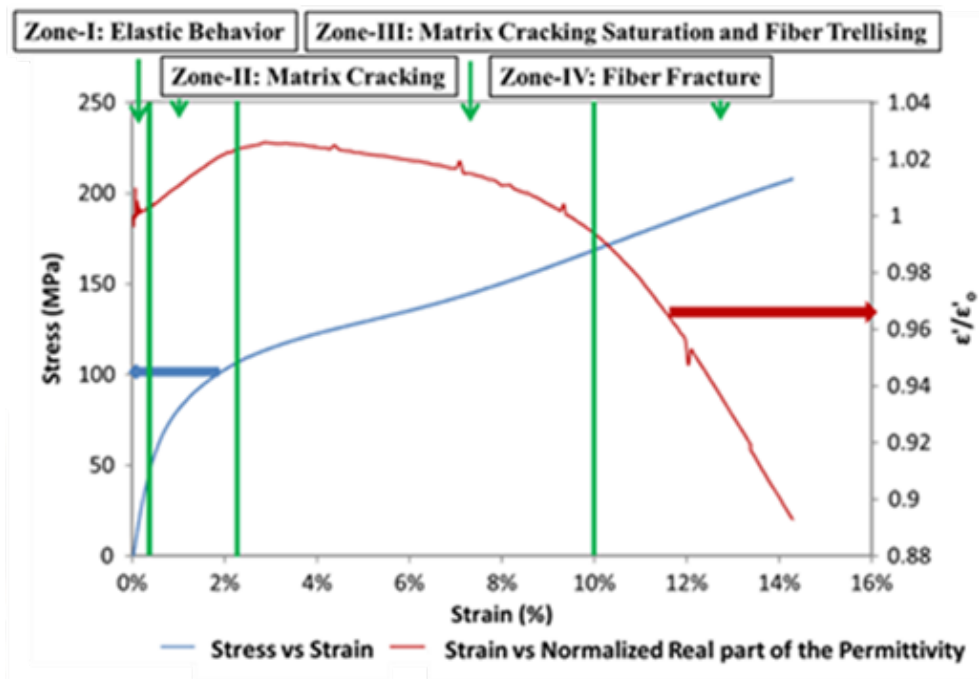
Figure 4.3 Insitu dielectric response observed by Raihan et al. [2]

During coupling of primary and secondary matrix cracks (refer to damage in composites in general sense) delaminations are triggered both at the free edge and at the interior which result in local failure. For off axis woven composites (tested by Raihan et al.[2]) , in the local volume of material where delamination occurs (at the intersection of tows and intersection of matrix cracks) the constraining effect of individual ply lamination is no longer present because of which the off axis fibers can now align to the loading direction for uniaxial loading, known as fiber trellising which results in a stiffening response at the global level. So, when a delamination is triggered the

plies are no longer bonded in the local region i.e. there are no more transfer of stresses across the interface. The same applies to the electric field as well (especially when it is a through thickness electric field), the local delamination acts as a discontinuous boundary which results in no flux across the delaminated boundary given by the equation

$$n.D = 0 \tag{4.1}$$

Recall that Maxwell-Ampere's law (Eq. (3.10)) is based on both conduction current J and dielectric displacement current $\frac{\partial D}{\partial t}$. In a given volume when delamination is triggered during loading, enforcing Eq. (4.1) results in a decrease in dielectric displacement current $\frac{\partial D}{\partial t}$ in the volume. This decrease in $\frac{\partial D}{\partial t}$ results in a negative $\frac{\partial \rho}{\partial t}$ which indicates that the charge is dissipating within the volume. If the charge dissipates, this indicates that the capacitance decreases and hence ε_r decreases. If $\frac{\partial \rho}{\partial t}$ is negative, this indicates that $\nabla.J$ is positive which means the conduction current is decreasing in the volume. If the conduction current is decreasing in the volume, this results in an increase in the impedance of the material system. On continuous loading, the delaminations start to coalesce resulting in increased rate of change of the dielectric state variables which is consistent with the findings from Raihan et al. [2] where they observed a slower change during the initiation of coupling followed by an increased rate of decrease in permittivity at the end stages. Let us now apply this understanding to various other material systems and stacking sequences to study the variation of dielectric response with material state change.

4.5.1 Identifying material state change in cross ply laminates

The cross ply laminates [90/0$_2$/90] were loaded in uni axial tension and simultaneous dielectric response was monitored. The mechanical response of the samples are shown below in Figure 4.4.
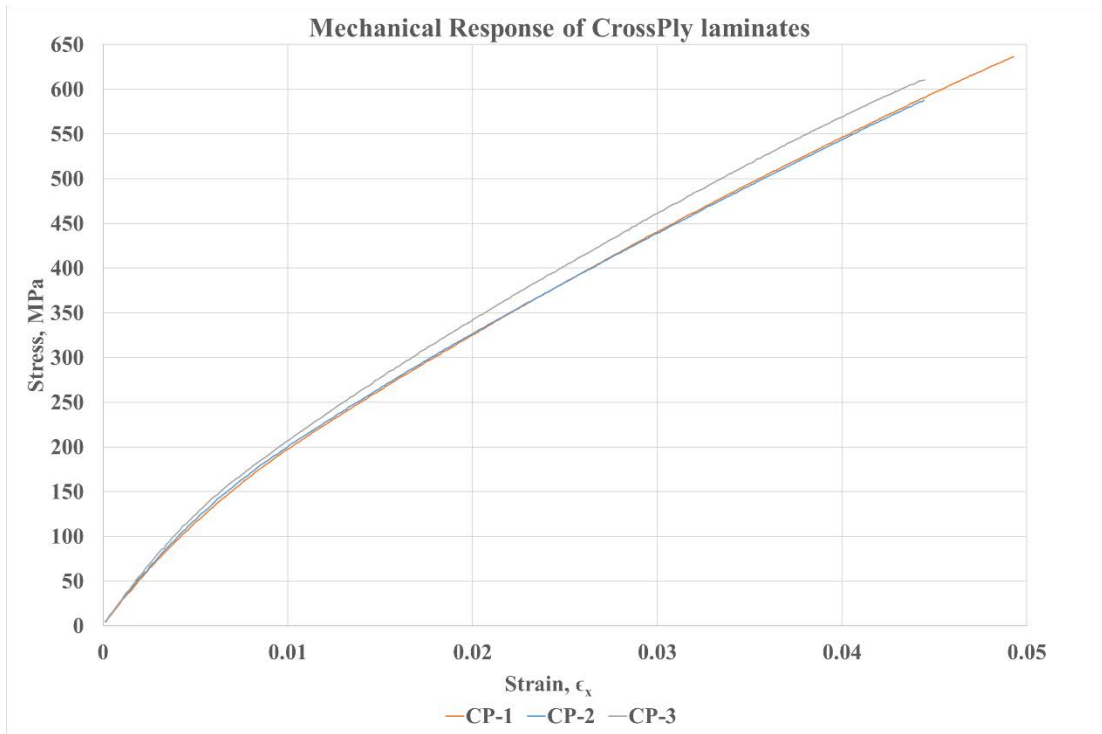
Figure 4.4 Mechanical behavior of cross ply laminates

In these laminates, transverse cracking is the primary damage mode observed at various sites along the length of the specimen until a saturation state (CDS) is attained. These cracks grow through thickness of the 90º ply almost instantly, but along the width these cracks grow in progression because of the thin ply constraint [3]. These transverse cracks alter the stress state of the longitudinal ply that results in creation of longitudinal cracks (matrix cracks in the 0º ply) at various sites along the width that don't grow instantly along the length as described in [4]. However, the out of plane stresses generated by the transverse cracks and longitudinal cracks are additive in nature and attains a maximum where these cracks cross in the laminate leading to local delaminations. The spacing of these longitudinal cracks along the width can be estimated similar to transverse crack spacing and has been established in [4]. On continuous loading, once all the transverse cracks have grown across the width these longitudinal cracks continue to grow along the length and simultaneously the delaminations coalesce as well. At this stage, the combined

effect of delamination and longitudinal cracks tend to isolate volume of material in the 0° ply termed as fiber splitting which occurs at various locations. This splitting results in increase in load to these fibers which result in local fiber failure and this alters stress distribution in the other fibers hence resulting in fiber fracture and global fracture. The fractured specimen can be seen below in Figure 4.5.

Figure 4.5 Fractured cross ply laminate showing transverse cracks, delaminations and fiber splits

The insitu dielectric response and the mechanical response for one specimen is shown below in Figure 4.6. The permittivity ε_r increases in the beginning due to transverse matrix cracks resulting in charge trapping (interfacial polarization). Once a saturation state is reached, the longitudinal cracks are formed followed by delaminations where these longitudinal and transverse cracks cross in the laminate. The result of these mechanisms is an increasing trend with a reduced slope as seen below in Figure 4.6. The reduced slope is the effect of local delaminations which result in no flux across the delaminated boundary (Eq. (4.1)). On continuous loading the longitudinal cracks continue to grow resulting in coalescence of delaminations thus resulting in decrease in ε_r with a smaller slope. At the end stages the coupling of longitudinal cracks and delaminations result in fiber splitting that tends to isolate more volume of the material and hence ε_r decreases with a larger slope as observed in Figure 4.6.
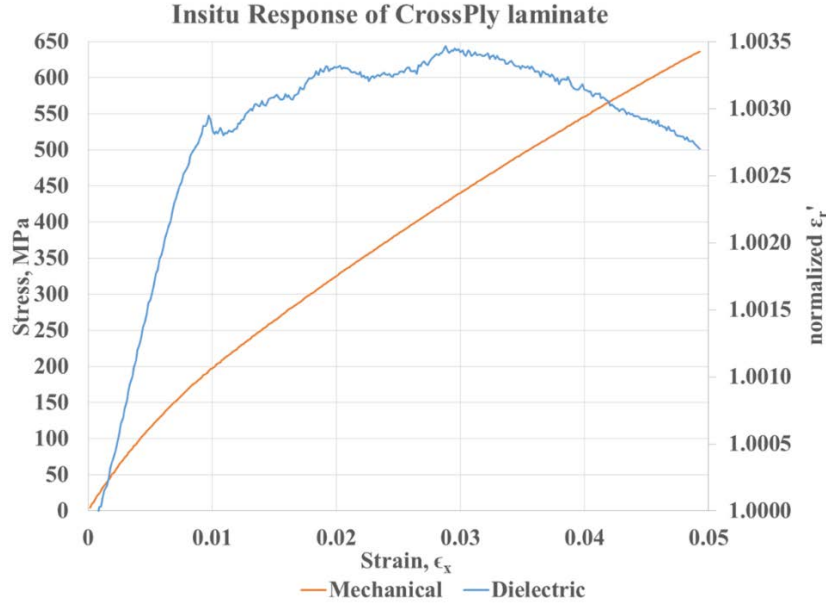
Figure 4.6 Insitu response of cross ply laminate

To better understand the correlation of the damage mechanisms with the change in dielectric response, the secant modulus and the slope of the dielectric state variable $\frac{d\varepsilon_r}{d\epsilon_x}$ is plotted in Figure 4.7. The secant modulus and $\frac{d\varepsilon_r}{d\epsilon_x}$ were normalized w.r.t initial values. The dielectric response was fitted using 4th order polynomial curves and the first slope of the curve was obtained. It can be observed that the secant modulus (mechanical state variable) changes at a higher rate till CDS, followed by a steady rate till failure; whereas the dielectric state variable has a higher rate of change at the beginning (during transverse matrix cracking) and steadily reduces till CDS is attained (due to delaminations from coupling of transverse and longitudinal cracks), followed by a steady slope when delaminations are coalescing gradually and an increased rate of change in the end (due to coupling of longitudinal cracks and delaminations leading to fiber splitting and fracture). To better visualize the change in the rate of change of dielectric state variable during damage progression, the second slope $\frac{d^2\varepsilon_r}{d\epsilon_x{}^2}$ was obtained and plotted in Figure 4.7. It can be

58

observed that the rate at which the dielectric state variable changes clearly depends on the material state and how the rate of interaction of damage events trigger the rate of change of dielectric state variable.
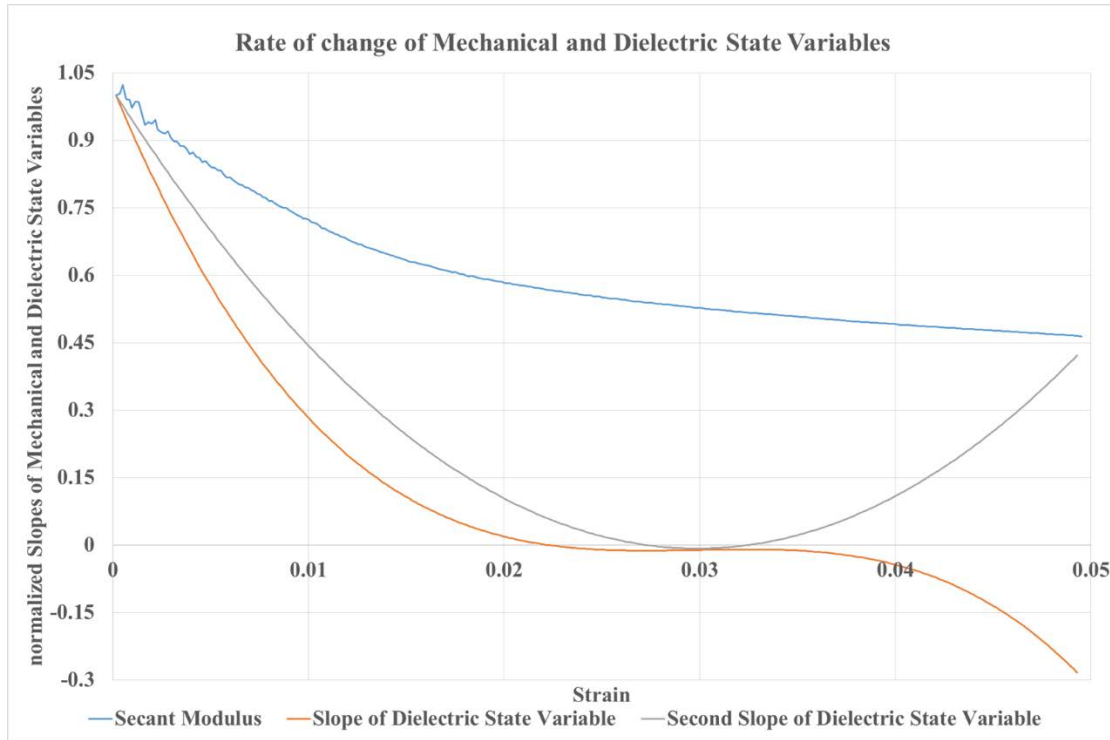
Figure 4.7 Rate of change of mechanical and dielectric state variables during damage progression in cross ply laminates

4.5.2 Identifying material state change in quasi isotropic laminates

Quasi isotropic laminates [-45/0/45/90]$_s$ were loaded in uni axial tension and simultaneous dielectric response was monitored. The average dimensions for these laminates were 198.24mm×18.01mm×1.427mm. The mechanical response of the samples are shown below in Figure 4.8.
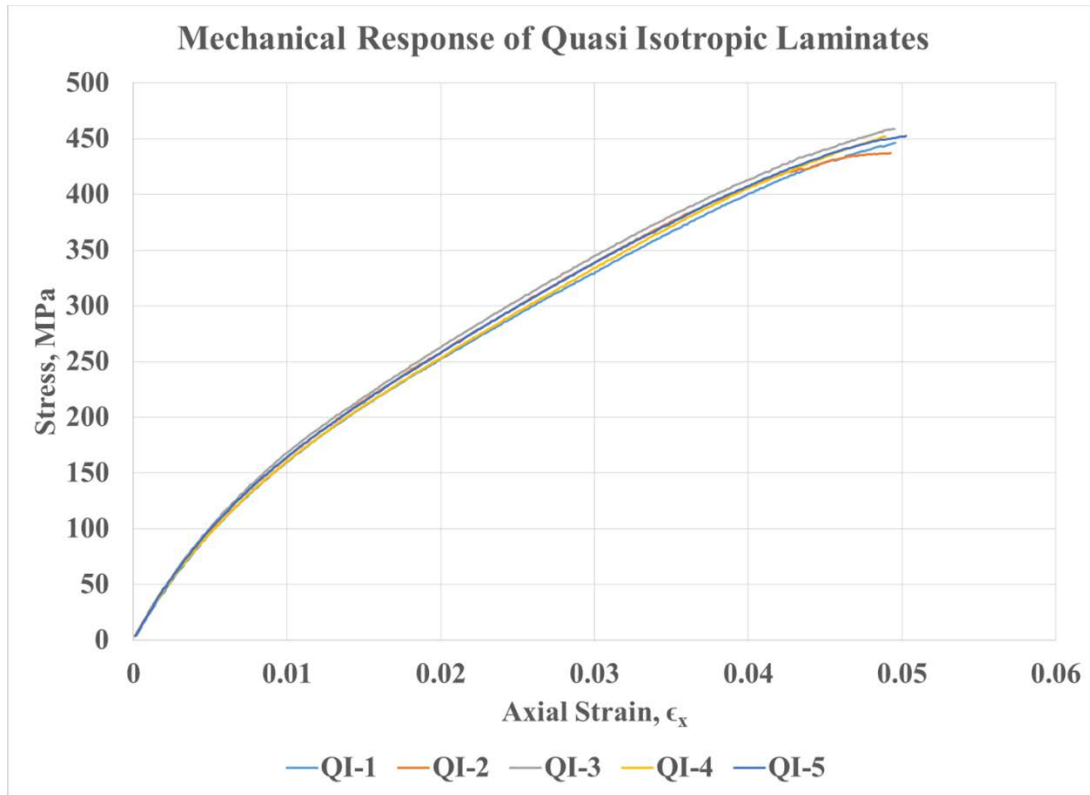
Figure 4.8 Mechanical behavior of quasi isotropic laminates

In these laminates, transverse cracking is the primary damage mode observed at various sites along the length of the specimen until a saturation state (CDS) is attained. These cracks grow through thickness of the 90º ply almost instantly and are arrested at the ply interface and start to grow across the width. After the saturation of the transverse cracks in the 90º ply, transverse cracks started to occur in the angled ply's (45º, -45º ply's) and attained a saturation state similar to the 90º ply. It was observed that during the creation of cracks in the 45º ply, longitudinal cracks emerged at the 90º ply interface and on continuous loading, the longitudinal cracks grew along the length connecting all the 90º ply cracks creating a large edge delamination as shown below in Figure 4.9. The 45º and -45º ply cracks also start to grow along the width and also induce edge delaminations at the 0º/45º and at the -45º/0º interface due to large interlaminar shear stresses and normal stresses near the free edge of these ply interfaces [5]. When the 45º cracks grow across the

width, the interlaminar normal stresses are additive where the 45º cracks and 90º cracks cross leading to interior delaminations. Following this longitudinal cracks start in the 0º ply. During this stage the edge delaminations at the 90º/45º start to grow across the width which results in local failures; and at this stage the increasing delamination transfers the load to the 0º ply resulting in fiber fractures and hence global fracture. The fractured specimens are shown below in Figure 4.10.

Figure 4.9 Edge delaminations at the 90º/45º ply interface that grows along the width to induce fracture

Figure 4.10 Fractured quasi isotropic laminates

The insitu dielectric response and the mechanical response for one specimen is shown

below in Figure 4.11. The permittivity ε_r increases in the beginning due to transverse matrix cracks

in the 90° ply resulting in charge trapping (interfacial polarization). Once a saturation state is

reached, transverse cracks are formed in the 45° and -45° ply along with edge delamination at the

interface between 90°/45°, 0°/45°, and -45°/0° ply's resulting in an increase in ε_r with reduced slope.

As the transverse cracks grow across the width, delaminations initiate between 90°/45° plies due

to additive interlaminar normal stress at the crack intersections resulting in a decrease in ε_r with

steady slope. At this stage, when the edge delamination at the 90°/45° starts growing across the

width towards the center, the rate of volume isolation increases and hence ε_r decreases at a very

high rate during end stages as shown below in Figure 4.11.
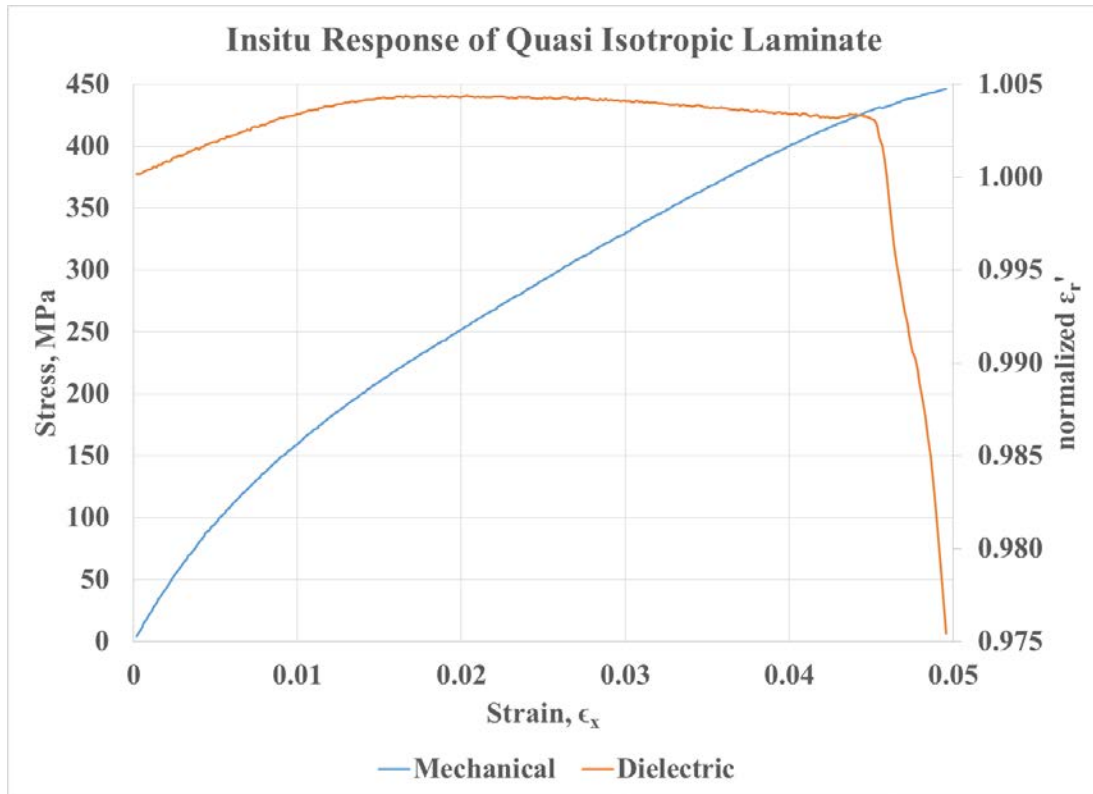
Figure 4.11 Insitu response of a quasi isotropic laminate

4.5.3 Identifying material state change in angle ply laminates

Angle ply (off axis) laminates [45° /-45°]$_s$ were loaded in uni axial tension and simultaneous dielectric response was monitored. Two sets of coupons were prepared for testing off axis laminates and the average dimensions for these laminates were 200mm×19mm×0.79mm. The mechanical response of the samples are shown below in Figure 4.12 [10].
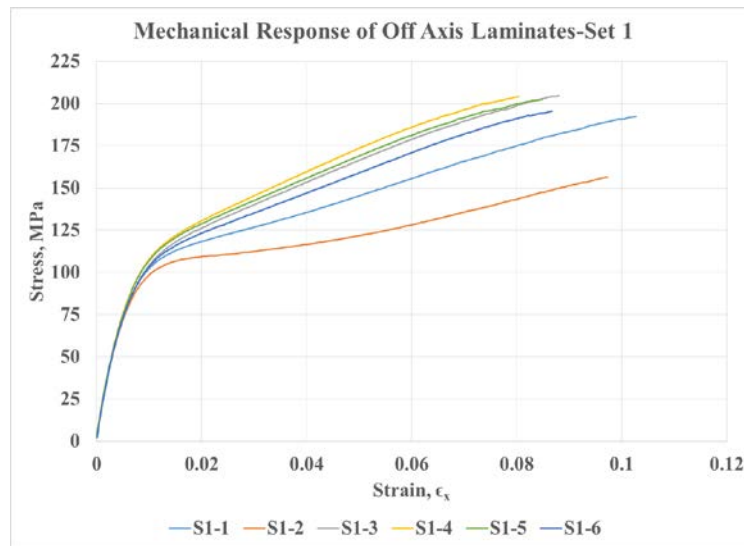
(a)
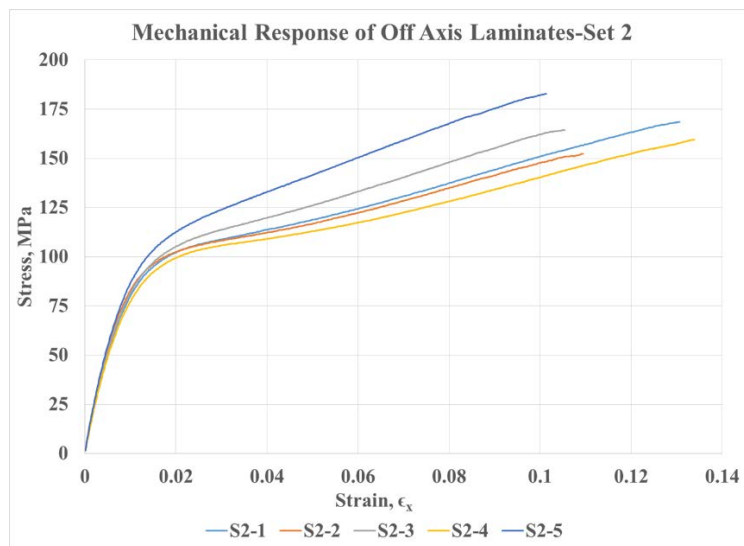
(b)

Figure 4.12 Mechanical response of off axis laminates- (a) set 1 (b) set 2

Damage in these laminates initiates at the free edge in the form of transverse cracks. The cracks were first observed in the outer 45º plies, however we couldn't tell if the cracking was symmetric in these (outer) plies from the edge replications we obtained, but some cracks were symmetric and others asymmetric. These cracks grow along the thickness gradually and are arrested at -45º ply interfaces. On continued loading, the cracks attained a saturation spacing along the length of the laminate and also started to grow across the width. At this stage, the cracks at the 45º/-45º ply interface induced longitudinal cracks (delamination (because of high interlaminar shear stresses)) and led to the creation of transverse cracks in the -45º ply's that grew almost instantly through the thickness. This occurred at most of the arrested cracks along the 45º/-45º ply and hence induced longitudinal cracks and transverse cracks in the -45º ply at these locations. On continuous loading, these longitudinal cracks coalesced to connect the transverse cracks in the -45º ply which led to creation of a single large edge delamination. As the transverse cracks (in both 45º and -45º plys) grow along the width, they induce additional interlaminar stresses (at the crack tips) and when these transverse cracks cross each other in the laminate, the combined effect induces local delaminations. From the mechanical response, stiffening behavior can be observed almost consistently in all the samples between 4-5 % axial strains (from Figure 4.12). We believe that this is an effect of local delaminations, wherein the constraining effect of individual ply lamination is no longer present because of which the off axis fibers can now align to the loading direction for uniaxial loading. This behavior is more predominant in woven off axis laminates and is known as fiber trellising. On continuous loading when one or more of these transverse cracks (in both 45º and -45º plies) grow along the entire width, coupled by delamination between these continuous transverse cracks to create separation of ply's and eventual failure. The details can be seen in the

fractured specimen and the edge replications shown below in Figure 4.13 and Figure 4.14 respectively [10].

Figure 4.13 Fractured off axis laminate
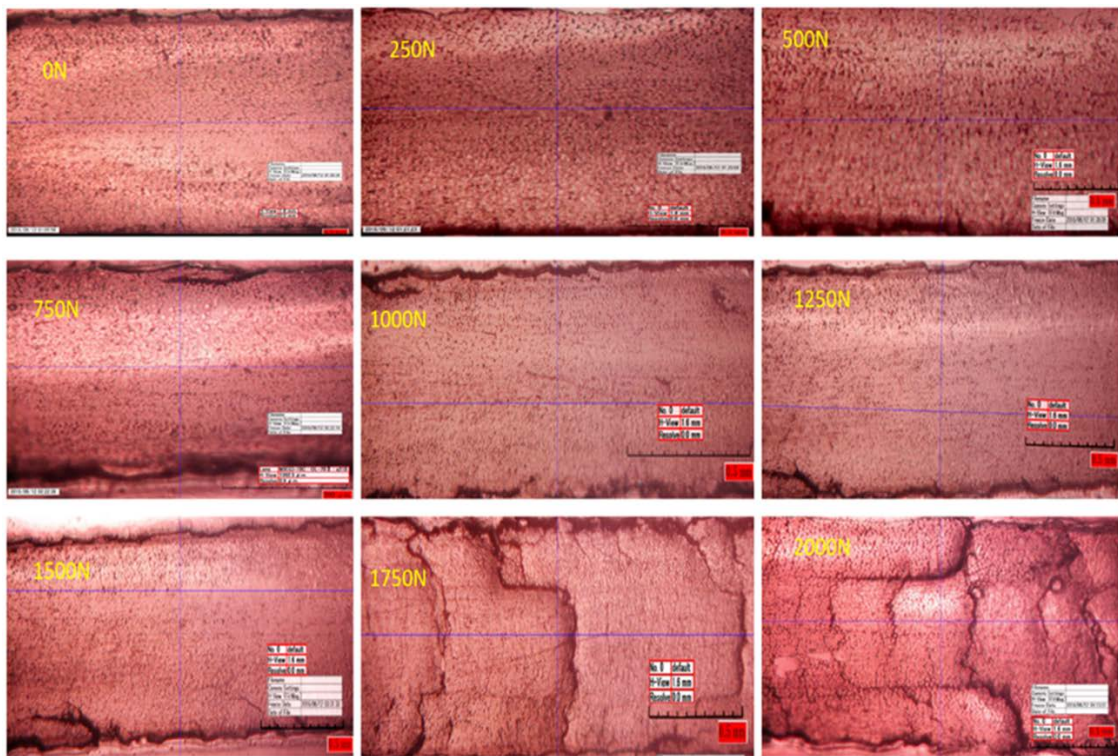
Figure 4.14 Edge replication showing damage mechanisms in off axis laminates

The insitu dielectric response and the mechanical response for one specimen is shown below in Figure 4.15. The permittivity ε_r increases in the beginning due to transverse matrix cracks in the 45° ply resulting in charge trapping (interfacial polarization). Once a saturation state is reached, transverse cracks are formed in the -45° ply along with longitudinal cracks (delamination)

at the interface between 45º/-45º ply's resulting in an increase in ε_r with reduced slope. On continuous loading, these longitudinal cracks connect all of the transverse cracks in -45º ply leading to edge delamination at various sites along the length resulting in a gradual drop in ε_r. On continuous loading the transverse cracks growing through width induce local delaminations leading to continued decrease in ε_r. At this stage, as the cracks start to grow at a higher rate across the width, the delaminations also grow at a higher rate resulting in higher rate of volume isolation and hence an accelerated drop in ε_r. When the transverse cracks have grown across the width the delaminations tend to coalesce (in the region of final failure where the transverse cracks cross in the laminate) and hence a larger slope change in ε_r. It can be observed from Figure 4.13 that the damage is lot more distributed along the specimen length (away from fractured region) in contrast to damage distribution in cross ply and quasi isotropic laminates, which is the primary reason for the long lasting drop in ε_r compared to the former laminate types.
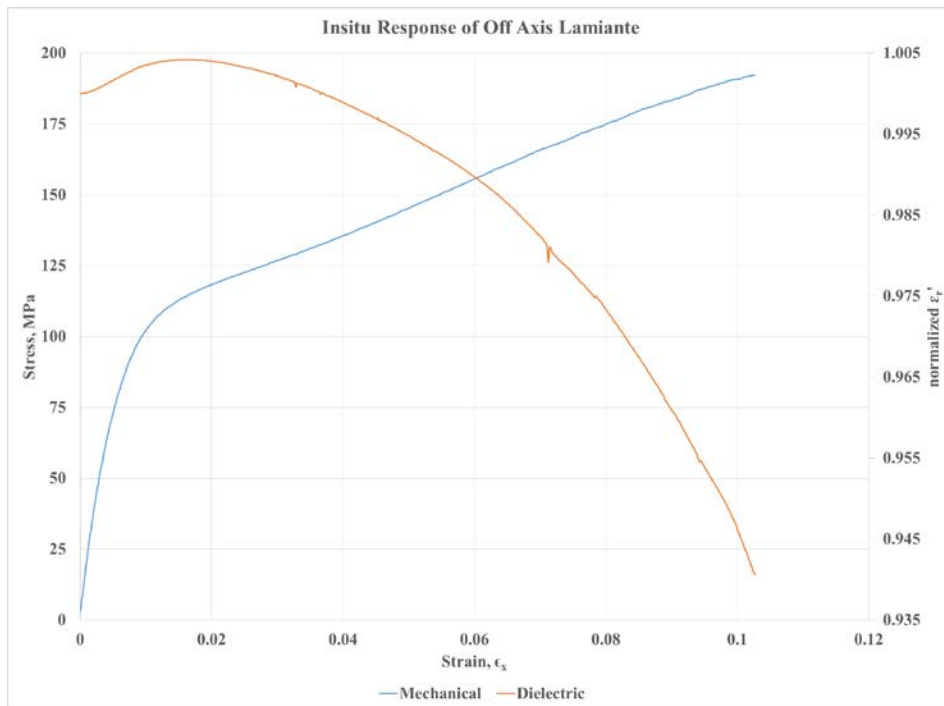
Figure 4.15 Insitu response of off axis laminate

66

4.5.4 Identifying material state change in woven composite laminates

The stress-strain response of the woven 45° coupons are shown in Figure 4.16. The modes of damage in woven composites are different then what is observed in uni-directional composites. The response to loading in the fiber directions can often be approximated as linear. However, the response to off-axis loading orientations is highly complex and significantly non-linear with very high strain to failure. As loading begins, an initial elastic (mostly) response is observed up to approximately 0.5% strain. At this point, matrix cracks begin to occur and on continuous loading, the density of these matrix cracks keep increasing, and the response becomes non-linear. Around 4% strain, the density of matrix cracks saturates and very few new single cracks are formed (CDS). Once a state of crack saturation is attained, the non-linearity resulting from matrix cracking is no longer prevalent. In this zone, the behavior is dominated by the fibers which have a tendency to reorient towards the loading direction. This behavior is referred to as trellising wherein the angle between reinforcement directions changes from 90°. The result of this is a stiffening response as observed in Figure 4.16. Fiber trellising continues until about 9% strain, where the fibers eventually begin to fail. The final non-linearity is the likely result of statistically based fiber failure over a range of axial strain [10, 11].
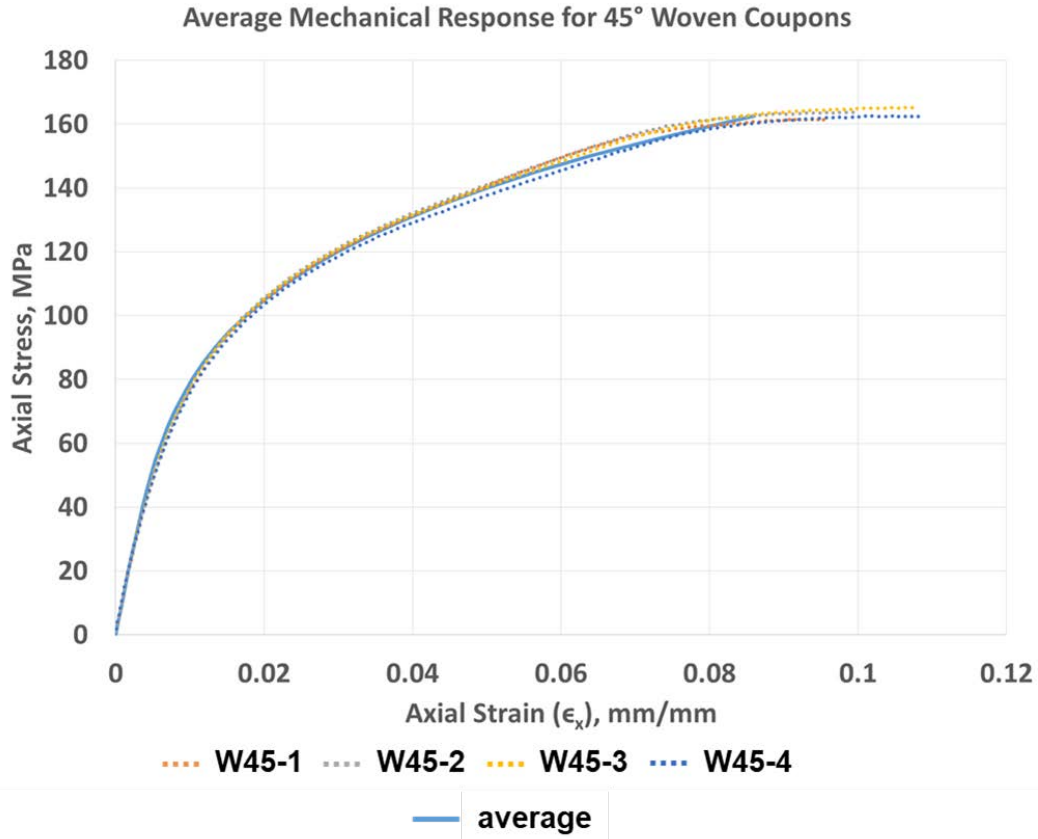
Figure 4.16 Mechanical response of 45° woven laminates [10]

The normalized dielectric response is shown in Figure 4.17. It can be observed that the trend is similar to response observed in uni-directional laminates, an initial increase followed by saturation and decrease. Similarly, the experimental data were fitted for the remaining orientations and the combined stress-strain plots and normalized dielectric response plots are shown in Figure 4.18 and Figure 4.19. It can be observed that for all orientations, there is an initial increase in the dielectric permittivity, followed by saturation and then a decrease that correlates with various damage mechanisms. The initial increase is caused by the micro cracking, followed by saturation that represents the Characteristic Damage State (CDS), followed by an initial permittivity decrease corresponding to crack coupling and delamination between tows leading to possible fiber trellising; the final slope change correlating to the end stages of fracture of the material system.
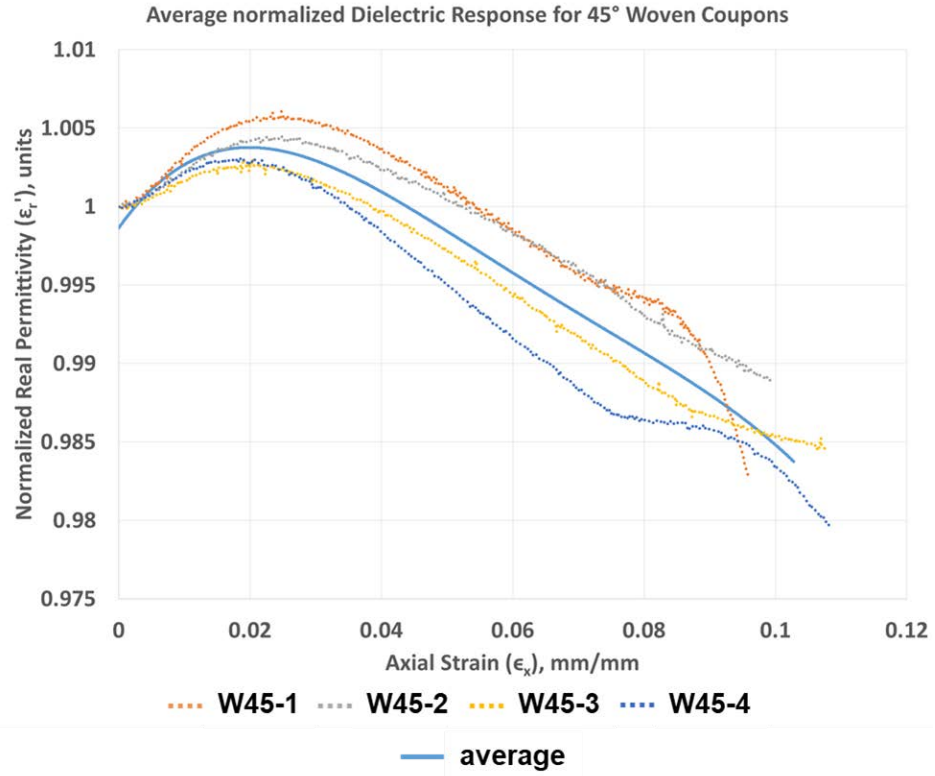
Figure 4.17 Normalized dielectric response of 45º woven laminates [10]

Figure 4.18 Combined mechanical response for different orientations [10]
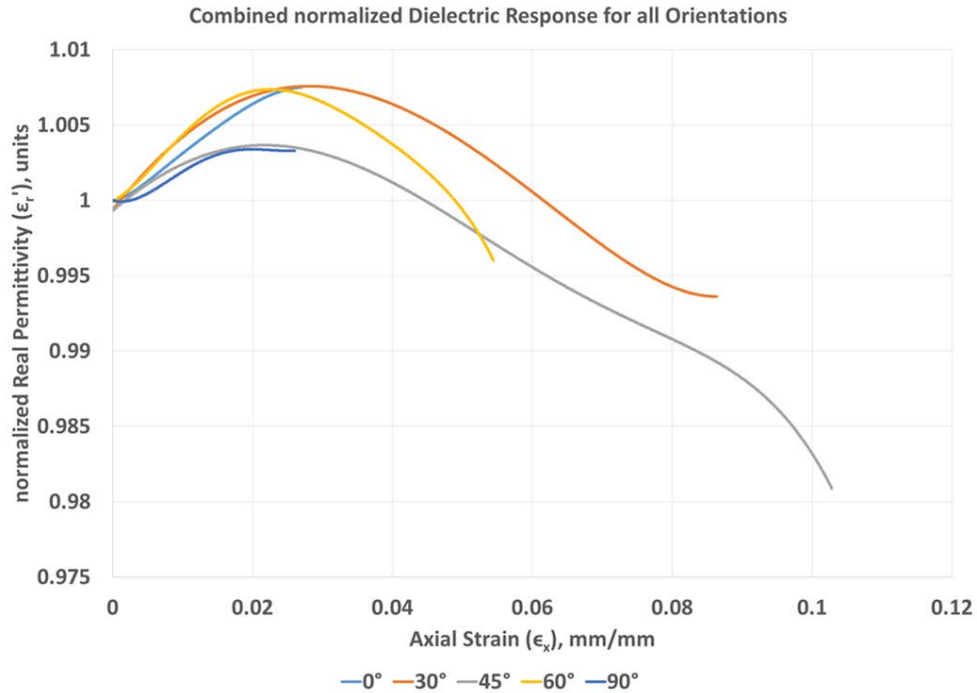
Figure 4.19 Combined normalized dielectric response for different orientations [10]

In this chapter, an attempt has been made to describe the mechanics of damage development and how the interaction of damage modes leads to material state changes. Also, a correlation was established between the mechanisms of damage development and the variation of dielectric state variable. In the next chapter, we take this understanding to develop multiphysics models that can simulate the variation in the dielectric state variable with damage development and further enhance our understanding of the physical defect coupling process.

4.6 References

[1]   Fitoussi, J., Meraghni, F., Jendli, Z., Hug, G., & Baptiste, D. (2005). Experimental methodology for high strain-rates tensile behaviour analysis of polymer matrix composites. Composites Science and Technology, 65(14), 2174-2188.

[2]   Raihan, R., Adkins, J. M., Baker, J., Rabbi, F., & Reifsnider, K. (2014). Relationship of dielectric property change to composite material state degradation. Composites Science and Technology, 105, 160-165..

[3]   Parvizi, A., Garrett, K. W., & Bailey, J. E. (1978). Constrained cracking in glass fibre-reinforced epoxy cross-ply laminates. Journal of Materials Science, 13(1), 195-201.

[4]   Jamison, R. D., Schulte, K., Reifsnider, K. L., & Stinchcomb, W. W. (1984). Characterization and analysis of damage mechanisms in tension-tension fatigue of graphite/epoxy laminates. In Effects of defects in composite materials. ASTM International.

[5]   PL-301, Technical Data Sheet for Newport 301 Epoxy Resin System. Irvine, CA. (2018). Retrieved from: http://mccfc.com/wp-content/uploads/2018/09/PL-301.091218.pdf

[6]   ASTM, D3039. (2008). Standard test method for tensile properties of polymer matrix composite materials.

[7]   Reifsnider, K., Rabbi, F., Vadlamudi, V., Raihan, R., & Brinkman, K. (2017). Critical path-driven property and performance transitions in heterogeneous microstructures. Journal of Materials Science, 52(9), 4796-4809.

[8]   Talreja, R. (2014). Assessment of the fundamentals of failure theories for composite materials. Composites Science and Technology, 105, 190-201.

[9]   Herakovich, C. T. (1989). Edge effects and delamination failures. The Journal of Strain Analysis for Engineering Design, 24(4), 245-252.

[10]   Vadlamudi, V., Shaik, R., Raihan, R., Reifsnider, K., & Iarve, E. (2019). Identification of Current Material State in Composites using a Dielectric State Variable. Composites Part A: Applied Science and Manufacturing, 105494.

[11]   Hufner, D. R. (2008). Progressive failure of woven polymer-based composites under dynamic loading; Theory and analytical simulation. (Doctoral dissertation, University of Connecticut). Retrieved from https://opencommons.uconn.edu/dissertations/AAI3308233

Chapter 5 Multiphysics Modeling of Material State Change in Composites

5.1 Background

In Chapter 4, the mechanics of damage development and the interaction of various damage modes was established. Also, based on Maxwell's equations the variation of dielectric response with damage development was explained. In this chapter we use this understanding to model damage development and the resulting variation in dielectric response due to material state change caused by damage development.

5.2 Modeling Damage Mechanisms in Composite Materials

5.2.1 Review of different techniques of modeling damage in composite materials

Evident from experimental findings and literature, fracture in a composite structure is the coupling of discrete damage events such as fiber/matrix debonding, matrix cracking, delamination and fiber failure. Matrix cracking is generally termed as intralaminar/intra-ply (with in the lamina) damage whereas delamination is known as interlaminar (interfacial) damage. The study of evolution of damage modes leading to fracture is generally termed as progressive damage analysis.

Intra-ply damage modes have been investigated primarily within the framework of continuum damage mechanics (CDM) [1, 2], while delamination has been studied extensively using interface fracture modeling techniques such as cohesive zone models [3–5] and virtual crack closure techniques (VCCT) [6, 7]. A critical distinction between the CDM and interface fracture models exists in the approach in which a displacement discontinuity is represented; i.e. the CDM methodology replaces the displacement discontinuity with local volumetric stiffness degradation, whereas the interface fracture-based techniques directly include the kinematics of the displacement

jump. As a result, CDM can be easily implemented into conventional non-linear finite element solvers. However, a key limitation of this approach is the inability to accurately model and capture localized interaction of damage modes (ex. matrix cracking and delamination).

Another approach is to model the kinematics of the displacement jump directly that occurs at the discontinuity. In the aspects of modeling, delamination surfaces in composite materials coincide with morphological features such as ply interfaces and hence can be represented by the opening of doubled nodes using existing finite element (FE) tools. Matrix cracks, on the other hand, are not straightforward within the framework of traditional FE tools. The kinematics of the crack front can be captured by traditional FE modeling combined with adaptive remeshing techniques [8], which have been successful in predicting complex crack evolution in metallic structures. However, application to laminated composites, where cracks form in different plies in adjacent locations, require remeshing under multiple mesh compatibility constraints. An alternative approach to modeling displacement discontinuities due to matrix cracking involves mesh independent crack modeling techniques. Over the last decade, a significant effort has been devoted to the concept of the eXtended Finite Element Method (x-FEM) to composite materials. Modeling a matrix crack that propagates parallel to the fiber direction in a ply is conceptually straightforward using x-FEM, it is more difficult to model networks of matrix cracks in a laminate where the fracture planes of matrix cracks in individual plies intersect at common interfaces and can cause delaminations that link the matrix cracks through the thickness. The difficulty in modeling linked networks of multiple cracks could be addressed by developing a special enrichment for multiple crack situations or by connecting two enriched/cracked elements.

Alternatively, Iarve proposed a regularized extended Finite Element Method (Rx-FEM) [9-11], where the step function used in x-FEM to describe the crack surface is replaced by a

73

continuous function facilitated by the use of displacement approximation shape functions to approximate the step function and thus maintain the Gauss integration schema for element stiffness matrix computation, without regard to cracking orientation. In this case, the Gauss integration points of the initial approximation may be used for integration of the enriched functions, providing a framework for connecting plies where the matrix cracks can propagate in arbitrary directions.

5.2.2 Discrete damage modeling of matrix cracks and delamination

In the present work, the discontinuity will be represented through discrete damage modeling by defining the displacement jump across the discontinuous boundary using Rx-FEM (BSAM). The advantage of using Rx-FEM is that the same cohesive element formulation can be used for both matrix cracking and delamination and only differ in how the propagation is defined.

The most important aspect of accurately predicting the damage modes and hence the laminate strength is how accurately the initiation of damage is specified. It is mandatory to specify a damage initiation criteria for discrete damage modeling. Hence selecting a failure criteria that considers the interaction of various stress fields and which is capable of modeling each failure mechanism separately is critical.

In the current work LaRC04 failure criteria will be used to predict damage initiation in laminates under uni-axial tensile loading. The failure index for matrix failure under transverse tension is given by Eq. (5.1)[12].

$$FI_{MT} = (1 - g)\frac{\sigma_{22}}{Y_T^{is}} + g(\frac{\sigma_{22}}{Y_T^{is}})^2 + \frac{\Lambda_{23}^0\tau_{23}^2 + \chi(\gamma_{12}^{u,is})}{\chi(\gamma_{12})} \leq 1 \qquad (5.1)$$

When the failure criteria is met at the integration point, Rx-FEM inserts a cohesive zone in the element. The formulation of the cohesive zone is based on Turon's cohesive element

formulation [5] which considers mode mixity in the displacement jump at the crack tip given by Eq. (5.2).

$$B = 1 - \frac{\langle \Delta u_n \rangle^2}{\lambda^2} \tag{5.2}$$

λ is the norm of the displacement jump. The functional shape of the fracture energy as a function of displacement jump is assumed to have the form given by Eq. (5.3)

$$\tau = (1 - d)K\Delta u - dK\langle \Delta u_n \rangle n \tag{5.3}$$

K is the initial penalty stiffness used to define the constitutive behavior of the cohesive element. The constitutive behavior is generally modeled as a bilinear law and the interface failure begins after the displacement jump reaches an initiation value given by Eq. (5.4)

$$\Delta_0 = \tau_0/K \tag{5.4}$$

τ_0 is the cohesive strength which depends on the interfacial normal and shear strength and the mode mixity parameter given by Eq. (5.5)

$$\tau_0^2 = Y^2 + (S^2 - Y^2)B^\eta \tag{5.5}$$

The fracture energy density is the area under the cohesive bilinear law given by Eq. (5.6)

$$g(\lambda, B) = \int_{q=0}^{\lambda} \tau(q, B)dq \tag{5.6}$$

To ensure correct crack propagation, final value of displacement jump Δ_f is defined such that the fracture energy density is equal to critical energy release rate given by Eq. (5.7) [9].

$$g(\Delta_f, B) = G_c(B) \tag{5.7}$$

In the traditional surface fracture cohesive constitutive formulation, the fracture energy density is function of crack opening displacement and is given by Eq. (5.6) and hence this

formulation can be used straight forward for delamination propagation (Eq. (5.7)) using Rx-FEM. However, for matrix crack propagation crack surface is replaced with a gradient zone in a volume and the fracture energy balance has to be expressed through volume integration given by Eq. (5.8) [9].

$$\iint_{\Gamma_\alpha \epsilon v} g(x)dS \approx \iiint_v g(x)|\nabla \widetilde{H}|dV \tag{5.8}$$

$|\nabla \widetilde{H}|$ is the approximate surface area of the crack enclosed in the volume. Combining Eq. (5.7) and eq. (5.8) the criteria for matrix crack propagation is given by Eq. (5.9)

$$\iiint_v g(x)|\nabla \widetilde{H}|dV = S * G_c(B) \tag{5.9}$$

5.3 Modeling Damage in the Dielectric Perspective

In the above section, the modeling technique of damage in composite materials had been established. Using Rx-FEM, we can simulate matrix cracks, delaminations and their interactions leading to fracture. Now, the challenge is how do we model this damage in the dielectric perspective? From experimental standpoint, it is clear that at the stages of damage initiation, growth and interaction the behavior of the dielectric state variable is different. So how do we couple this damage development with dielectric behavior?

A robust and the rigorous approach would be to fully couple the physical fields i.e. stress field and the electric displacement field as developed by several research groups [13-15]; we would like to implement this formulation in the future research plan. For the current work, we developed a semi coupled formulation where the damage in the material (displacement jump due to stress field) is going to indirectly alter the dielectric state variable (electric displacement field) by means of polarization mechanisms and Maxwell's equations and will be described in detail in this section.

76

To gain a better understanding, we recall the polarization mechanisms described in section 2.4 of chapter 2. As described there are several polarization mechanisms in a dielectric that opereate at different frequency ranges. While the electronic, ionic and orientational polarization occur at high frequency in the range of 1MHz-10^{16} Hz, these mechanisms deal with charges bound in the atoms or molecules of the dielectric material. Since dielectrics are not insulators, they have some free charge carriers that can migrate in the material. A low frequency electric field can displace these charges and if there are interfaces in the material system, these charge displacements can be impeded at these interfaces and get trapped at these locations. This mechanism is termed as interfacial or space charge polarization and this behavior can be modeled by Maxwell-Wagner-Sillars (MWS) polarization theory [16].

Theory of MWS model states that "interfacial polarization processes occur in heterogeneous dielectrics as a result of the build-up of space charges at interfaces between two media having differing permittivity's and conductivities" [17]. It is straightforward that in the case of composite materials, the heterogeneity of the material system is the added benefit of modeling the MWS polarization theory. This was validated in section 3.5 and section 3.6 using models of current conservation (Maxwell-Ampere law of current conservation) to simulate interfacial polarization in composites and predicting the effective (homogenized) dielectric properties. Now when we model the global laminate response, the lamina is homogenized and the electric field would be uniform everywhere (similar to stress field in a homogenized lamina). However, when discrete damage events are developed, the displacement jumps create the discontinuities (crack boundaries) in the homogenized laminate and can be used as interfaces for simulating the MWS effect by importing the deformed displacement fields.

Now, using a continuum damage mechanics (CDM) model in the dielectric behavior we can simulate the MWS polarization. The methodology is outlined below.

At every material point, for every increment of the mechanical response till laminate failure:

1. The deformed displacement fields along with the displacement jumps are imported.

2. A CDM model is implemented in the dielectric response where the displacement jumps are modeled as stiffness (dielectric stiffness matrix) degradation.

3. Dielectric response is simulated at low frequency (100 Hz) to simulate the MWS polarization.

4. Effective dielectric state variables of the damaged material system are calculated.

The outlined process is represented pictorially below in Figure 5.1
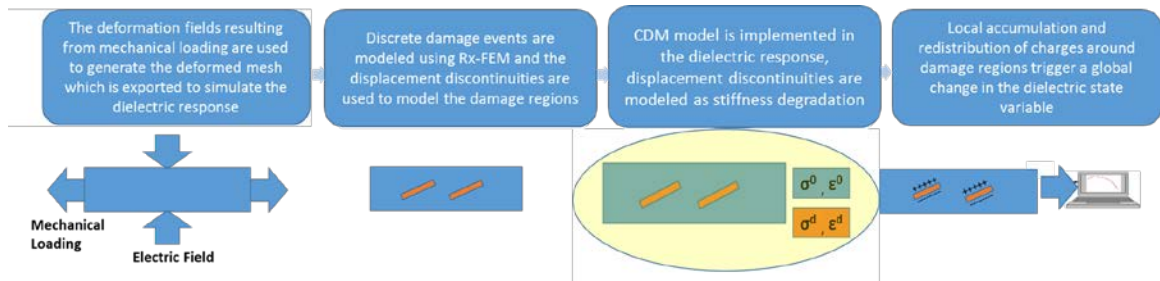

Figure 5.1 Modeling damage in the dielectric perspective

5.4 Computational Setup for Multiphysics Modeling of Material State Change

5.4.1 Computational setup for discrete damage modeling using Rx-FEM in BSAM

Rx-FEM was used to model progressive matrix cracking and delaminations in the 4 ply off axis laminate with the stacking sequence [45/-45]$_s$. Abaqus^{TM} was used to model, and mesh the geometry and the input file was then exported to BSAM which would perform the analysis. The

model and boundary conditions are shown in Figure 5.2. To eliminate the effect of boundary conditions, regions close to the boundaries were not allowed to develop damage as shown below in Figure 5.2. The applied displacement is divided into a number of load steps (increments). Element size of 1 mm was chosen based on recommendations made by Leone et al. [18] given by (Eq.'s 5.10 & 5.11). The outer (45° plies) were meshed with 1 element through thickness, whereas inner (-45° plies) were modeled as one thick ply with 2 elements through thickness. A mesh convergence study will be done by meshing the outer ply with 4 elements through thickness and the inner thick ply with 8 elements through thickness.

$$L_e \leq \frac{2G_{Ic}E_y}{Y_t^2} \tag{5.10}$$

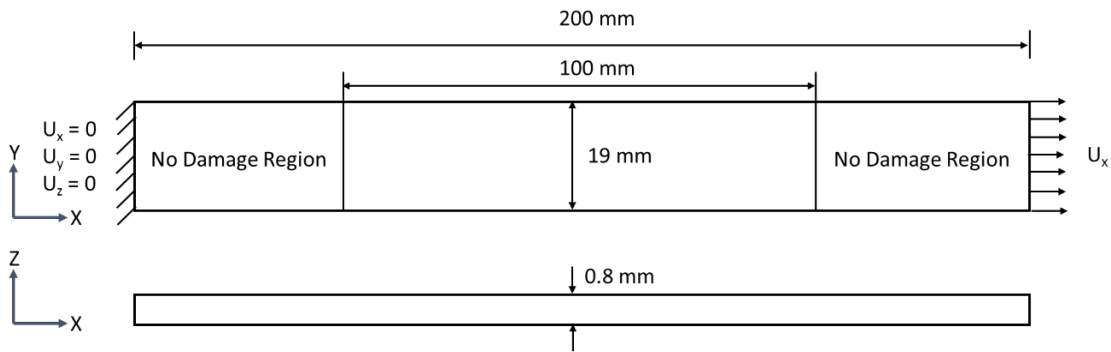$$L_e \leq \frac{2G_{IIc}G_{xy}}{S_L^2} \tag{5.11}$$

Figure 5.2 Geometry and boundary conditions for the computational model

The generated mesh is shown in Figure 5.3. The ply level properties were determined using micromechanics and are tabulated in Table 5.1 [19].
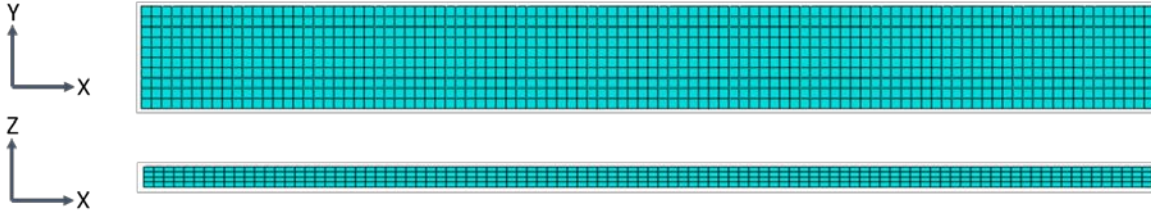
Figure 5.3 Finite element mesh of the computational model

Table 5.1 Predicted E-glass/Np310 mechanical properties [19]

Property	Description	Value	Units
E_{11}	Longitudinal modulus (fiber direction)	46.5	GPa
E_{22}, E_{33}	Transverse modulus (matrix direction)	15	GPa
ν_{12}, ν_{13}	Poisson's ratio 12,13	0.12	-
ν_{23}	Poisson's ratio 23	0.17	-
G_{12}	In-plane shear modulus	5.8	GPa
G_{13}	Transverse shear modulus (1-z plane)	5.8	GPa
G_{23}	Transverse shear modulus (2-z plane)	6.8	GPa

A crack (cohesive zone) was inserted in the element when the LaRC04 failure criteria at an integration point was met as described in section 5.2.2. The crack propagation takes place when the energy release rate in the crack volume reaches a critical value (Gc) (Eq. (5.9)). Eventually final failure occurs when a delamination initiates and opens to link the matrix cracks in different plies. To simulate the shear nonlinearity, the experimental (observed) non-linear shear stress-strain curve was used as input to BSAM as shown in Figure 5.4.

To obtain the transverse tensile strength Y_t, and the in plane shear strength S_L, we obtained the stress levels at which the initial matrix micro cracks were observed in the edge replication

images, input the stress level in the CLT code to obtain the ply level stresses. The observed strengths were $Y_t = 13\ MPa$ and $S_L = 24.2\ MPa$. The critical energy release rate ($G_{IC} = 140Jm^{-2}$) was obtained from literature [20]. However, G_{IIC} was estimated as $G_{IIC} = 2G_{IC}$ in the current prediction.
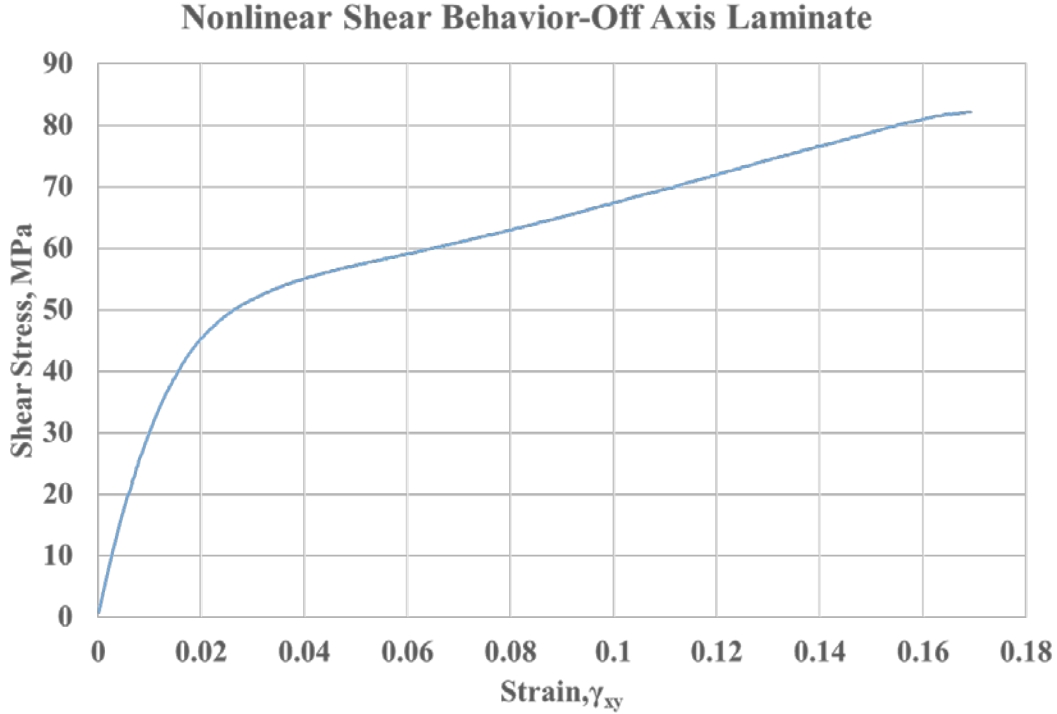

Figure 5.4 Observed nonlinear shear behavior of the off axis laminate

At the end of each load step (increment), BSAM writes the nodal displacements, stresses, strains and damage variables to a DAT file. A python script was developed that generates an INP (Abaqus^{TM}) input file from the DAT file and also creates an element set with cracked (open) elements (if any) based on the damage variable given by Eq. (5.12) below.

$$Damage\ Variable\ (MIC) = \begin{cases} 0 & No\ crack \\ 0 < MIC < 0.95 & Not\ an\ open\ crack \\ 0.95 \leq MIC \leq 1 & Open\ crack \end{cases} \quad (5.12)$$

Using the Abaqus^{TM} scripting interface, the cracked (open) elements set (if any) in the INP file is used to generate uncracked and cracked domains (if any) and are exported as STL files. These STL files can be imported into Comsol Multiphysics^{TM} using the imported mesh feature. This procedure is repeated for each increment till failure. The process is shown in Figure 5.5.
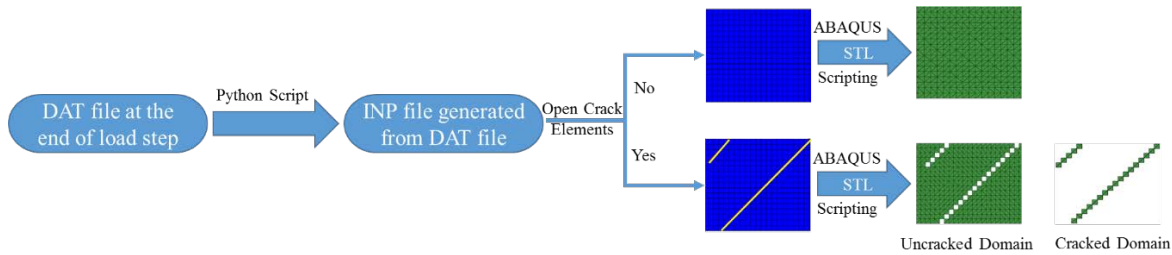

Figure 5.5 Post processing of BSAM results for the multiphysics response

5.4.2 Computational setup to model dielectric state variable change during damage development

The post processing of BSAM DAT files is the preprocessing step for modeling the dielectric response. As discussed above, the STL files are imported into Comsol Multiphysics^{TM} using the import mesh feature. The effective material properties of the homogenized plies are obtained through micromechanics simulations done in section 3.6.2. As mentioned earlier, to define the orthotropic material behavior the constitutive law has to be defined using orthotropic dielectric stiffness matrix which based on current conservation principle is a combination of the dielectric constant ε_r and the conductivity σ of the material. The predicted dielectric properties from the micromechanics model are tabulated below in Table 5.2.

Table 5.2 Predicted dielectric properties of E-glass/Np310

Property	Description	Value	Units
ε_{rx}	Dielectric constant in X direction	4.98	-
ε_{ry}	Dielectric constant in Y direction	4.68	-
ε_{rz}	Dielectric constant in Z direction	4.68	-
σ_x	Conductivity in X direction	6.4E-14	$\Omega^{-1}m^{-1}$
σ_y	Conductivity in Y direction	4.87E-14	$\Omega^{-1}m^{-1}$
σ_z	Conductivity in Z direction	4.87E-14	$\Omega^{-1}m^{-1}$

The dielectric tensor can be transformed to the lamina orientation (θ) by using the tensor rotation given by Eq's (5.13 & 5.14). Similarly, the lamina conductivity tensor can be obtained. These can be defined directly in the stiffness matrix using θ as a parameter that varies in every lamina of the laminate.

$$\varepsilon_{lam} = [T]\left[\varepsilon_{principal}\right][T]' \tag{5.13}$$

$$T = \begin{bmatrix} cos\theta & -sin\theta & 0 \\ sin\theta & cos\theta & 0 \\ 0 & 0 & 1 \end{bmatrix} \tag{5.14}$$

Using CDM model, the stiffness matrix of the cracked domains are now degraded. For the ideal case, we start with vacuum properties ($\varepsilon_r = 1.0005, \sigma = 1E - 15[S/m]$) in the crack domain and discuss the predictions. The effective dielectric properties can be calculated using Eq. (3.27) and is given below for reference

$$\varepsilon = \frac{1}{j\omega \left(\frac{\varepsilon_0 A}{d}\right) Z^*} \tag{3.27}$$

5.5 Results and Discussion

5.5.1 Mechanical response

The simulated cracks and fracture surface are shown below in Figure 5.6 [19]. It can be observed that the simulated fracture surface is identical to the observed fracture surface where in the final fracture takes place when the matrix cracks grow across the width and hence the delaminations coalesce in the region leading to separation of plies and hence fracture.
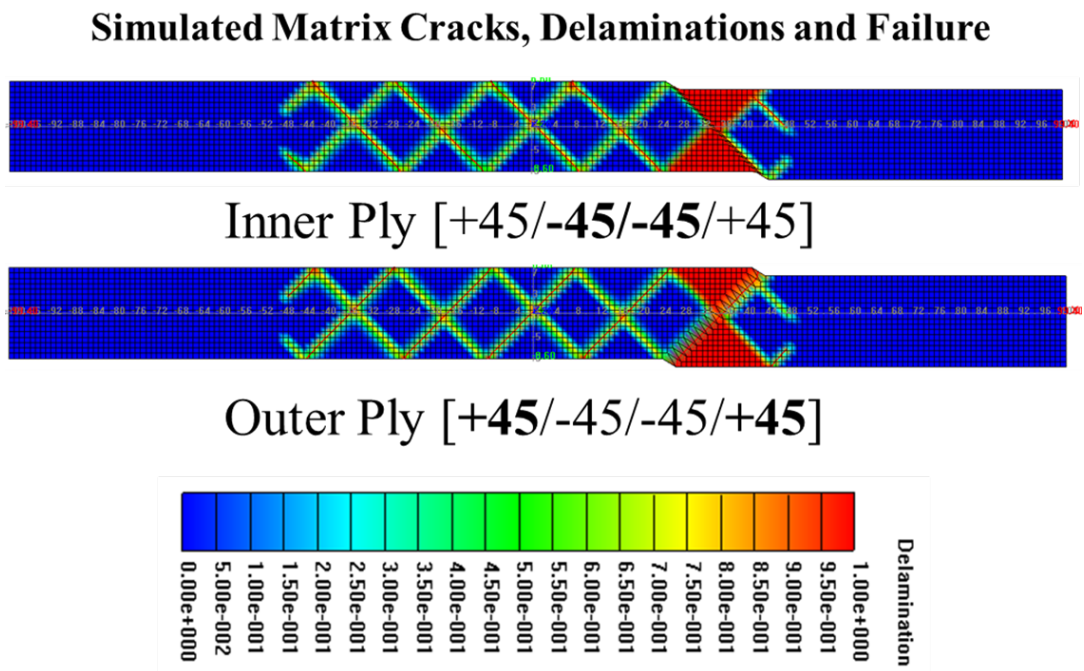

Figure 5.6 Simulated discrete damage events using Rx-FEM

The simulated and the observed stress strain response is shown below in Figure 5.7. It can be observed that both the stress and strain to break predictions are way off. The progressive failure simulation begins with matrix crack insertion, their opening and eventually final failure when a delamination initiates and opens to link the matrix cracks in different plies. The controlling material property for the delamination propagation in this case is G_{IIC} since it is a mode II delamination. This parameter was estimated as $G_{IIC} = 2G_{IC}$, which is perhaps a lower bound and

a more typical ratio would be about 4 as in most CFRP [21]. To estimate the sensitivity of the strength prediction to G_{IIC} a higher $(G_{IIC} = 1350Jm^{-2})$ was used and much more accurate strength predictions were obtained as shown in Figure 5.8.
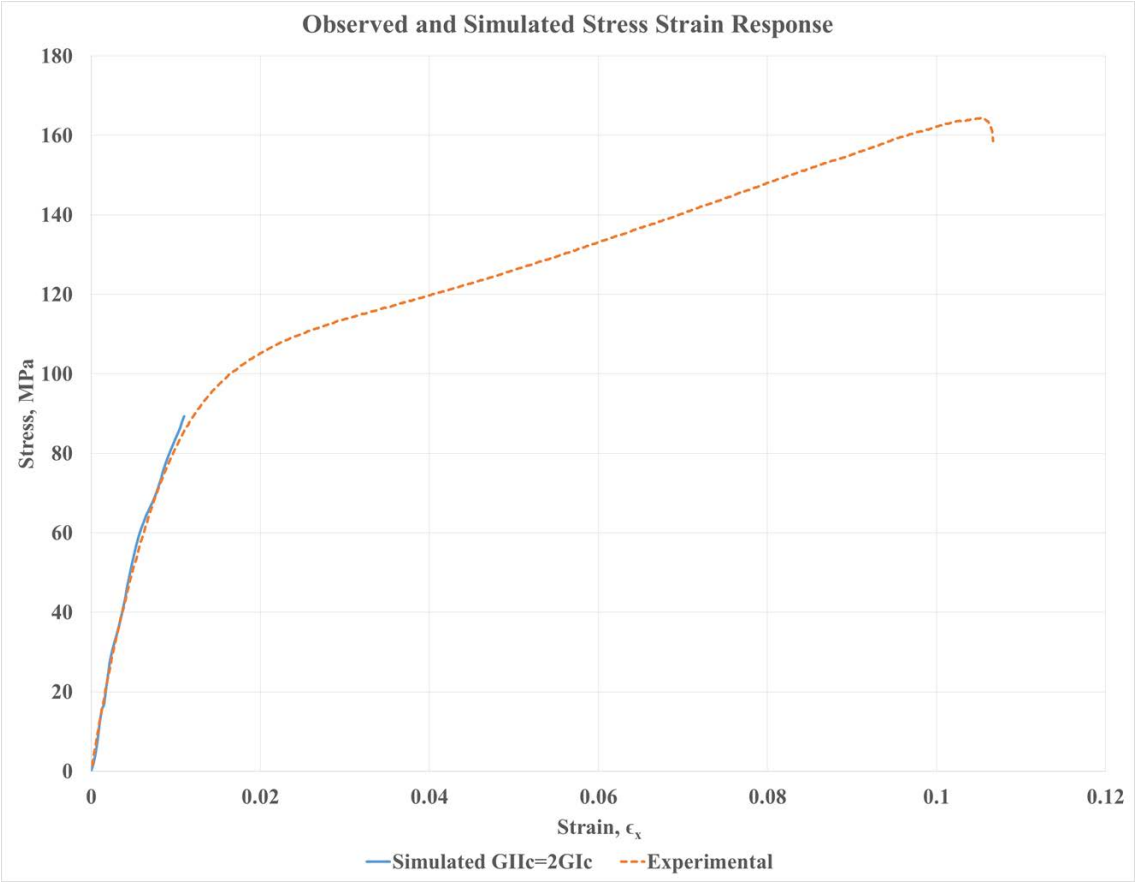

Figure 5.7 Observed and predicted stress strain response with lower bound of G_{IIc}

A mesh convergence study was performed with more number of elements through thickness to check the accuracy. It was observed that by increasing more number of elements through thickness, the strength predictions were accurate than using one element through thickness as shown below in Figure 5.9.
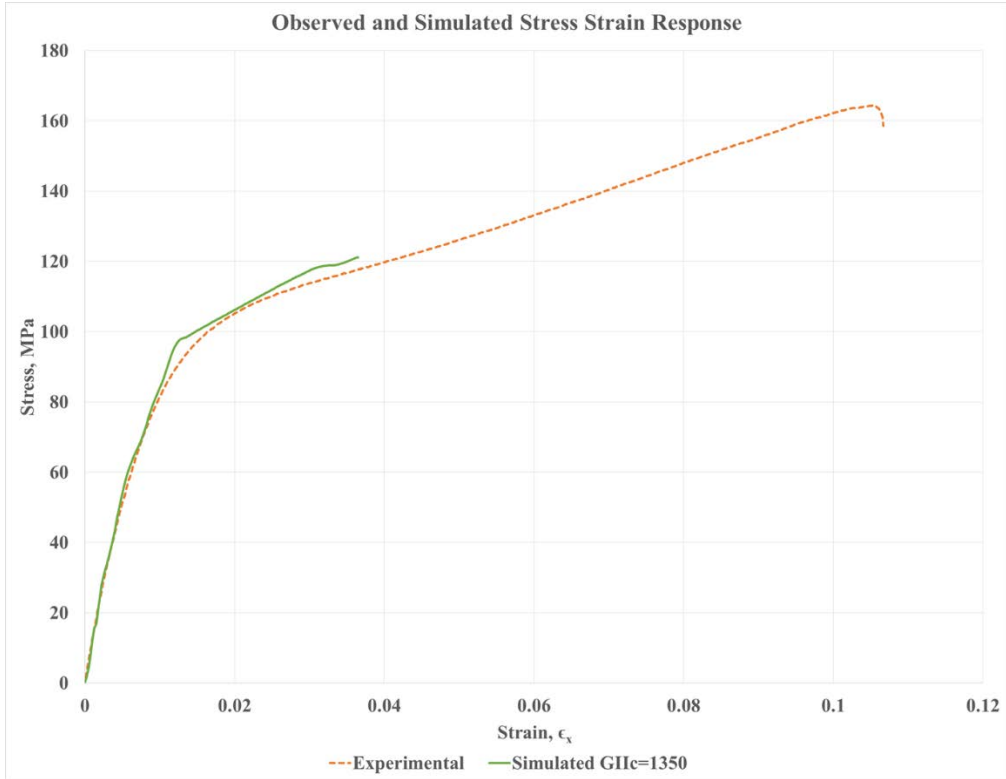
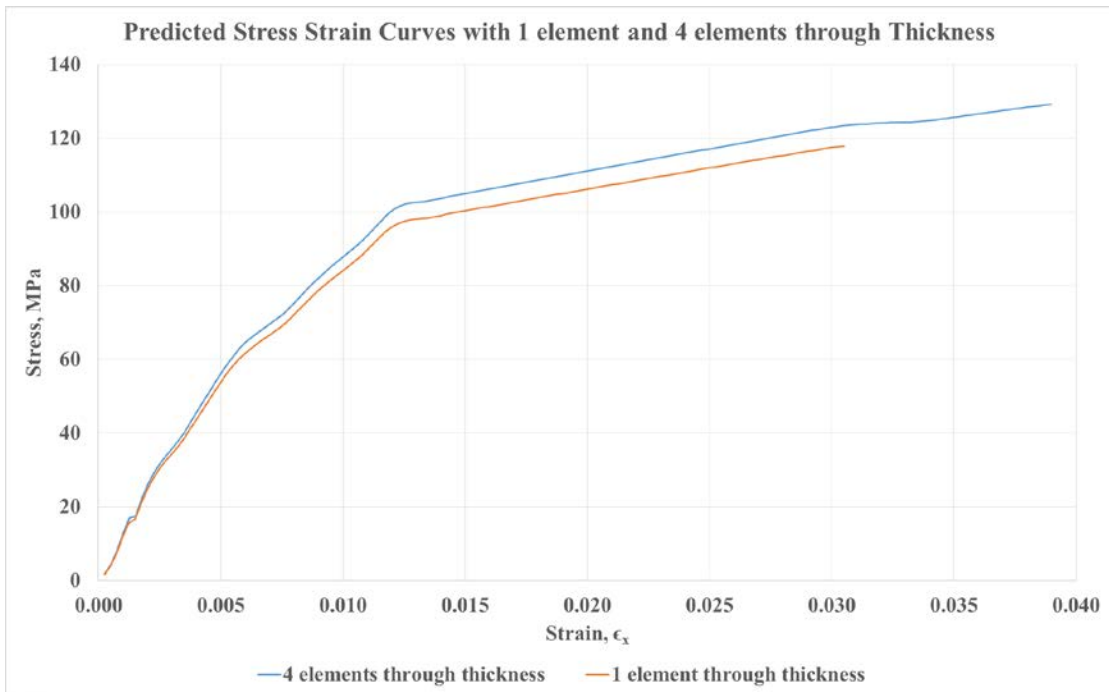Figure 5.8 Observed and predicted stress strain response with $G_{IIc}=1350Jm^{-2}$

Figure 5.9 Predicted stress strain response with 4 elements through thickness

However, the main intention of this work is to simulate the dielectric response with simulated defect patterns and hence the displacement fields and damage patterns obtained from the initial model with value of $(\sigma_{22} = Y_t = 13\ MPa, \tau_{12} = S_L = 24.2\ MPa, G_{IC} = 140\ Jm^{-2}$ and $G_{IIC} = 280\ Jm^{-2})$ were used to simulate the dielectric response.

5.5.2 Dielectric response

The STL files generated by the python script were imported. The model with cracked domains (transparent rendering) is shown below in Figure 5.10.
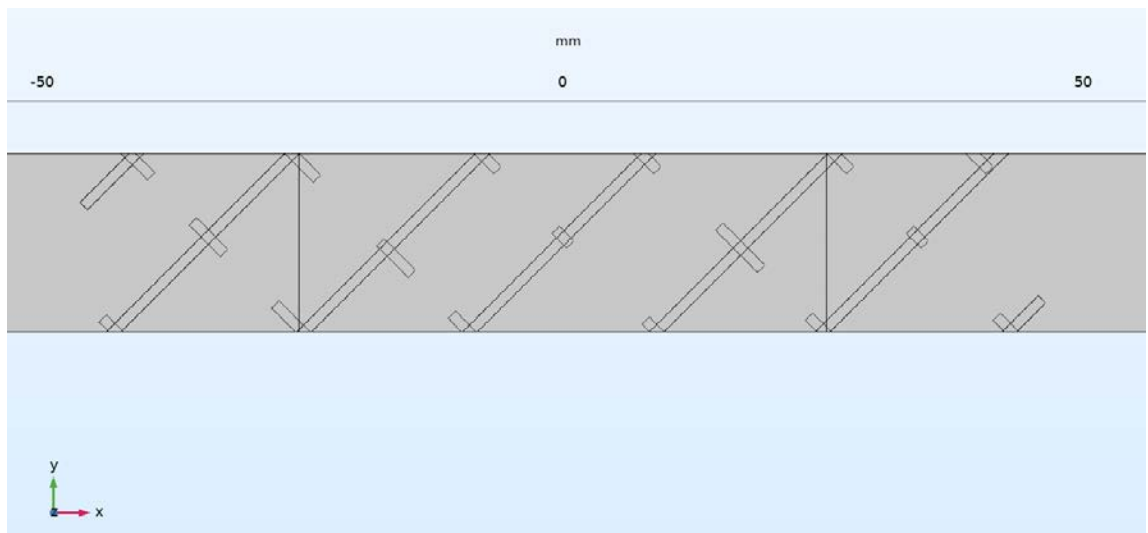

Figure 5.10 Transparent rendering of model with imported undamaged and cracked domains

In the initial study, the cracked domains are assigned with vacuum properties whereas the undamaged domains are assigned with the properties from section 5.4.2. The potential distribution through thickness of the laminate with in a cracked domain is shown below at a load step in Figure 5.11.
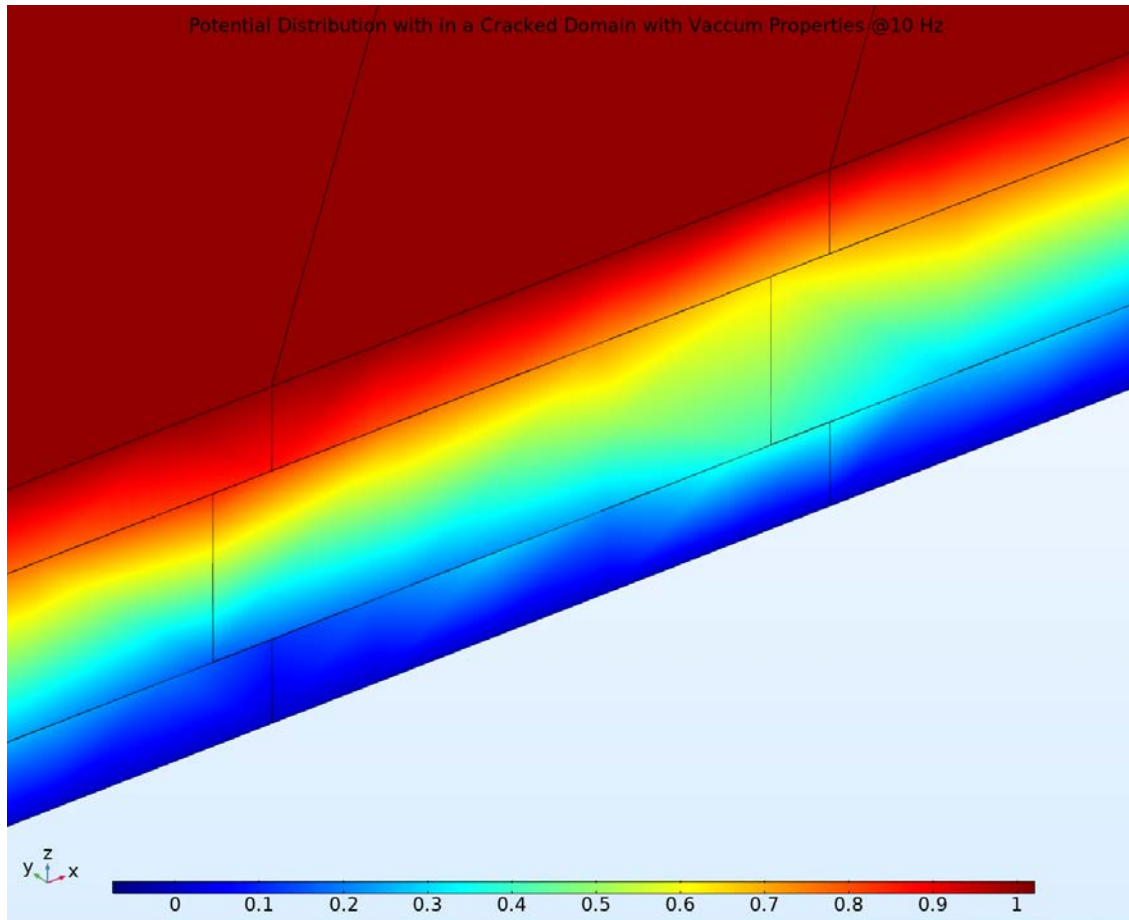
Figure 5.11 Potential distribution through thickness with in a cracked domain

From Figure 5.11 it can be observed that there exists a potential drop across the cracked domain. A potential drop across the domain indicates electric field distribution with in the domain exists or charge build-up with in the cracked domain. But as per Maxwell-Wagner-Sillars (MWS) polarization theory "interfacial polarization processes occur in heterogeneous dielectrics as a result of the build-up of space charges at interfaces between two media having differing permittivity's and conductivities", and hence to model interfacial polarization with accumulation of space charge at the interface, the dielectric properties in the cracked domain have to be more conductive than the bulk material. This theory was validated in section 3.5.2 where the more conductive inclusion results in build-up of charge at the interface.

So the next question is what should be the properties of the cracked domain. The primary requirement is that the cracked domain has to be more conductive than the undamaged domain to be able to simulate interfacial polarization. A viable fit for this requirement was moisture which always exists within the laminate or can diffuse into the laminate from environment or from environment in to the laminate [22-24].

So using moisture properties ($\varepsilon_r = 20, \sigma = 1E - 5[S/m]$) in the cracked domain would then lead to uniform potential distribution with in and hence leads to build-up of space charge at the interface as shown below in Figure 5.12. It is important to note that we don't claim that moisture is diffusing into the crack, we are only using moisture as a trigger for interfacial polarization. The variation in the dielectric state variable with damage is shown in Figure 5.13.
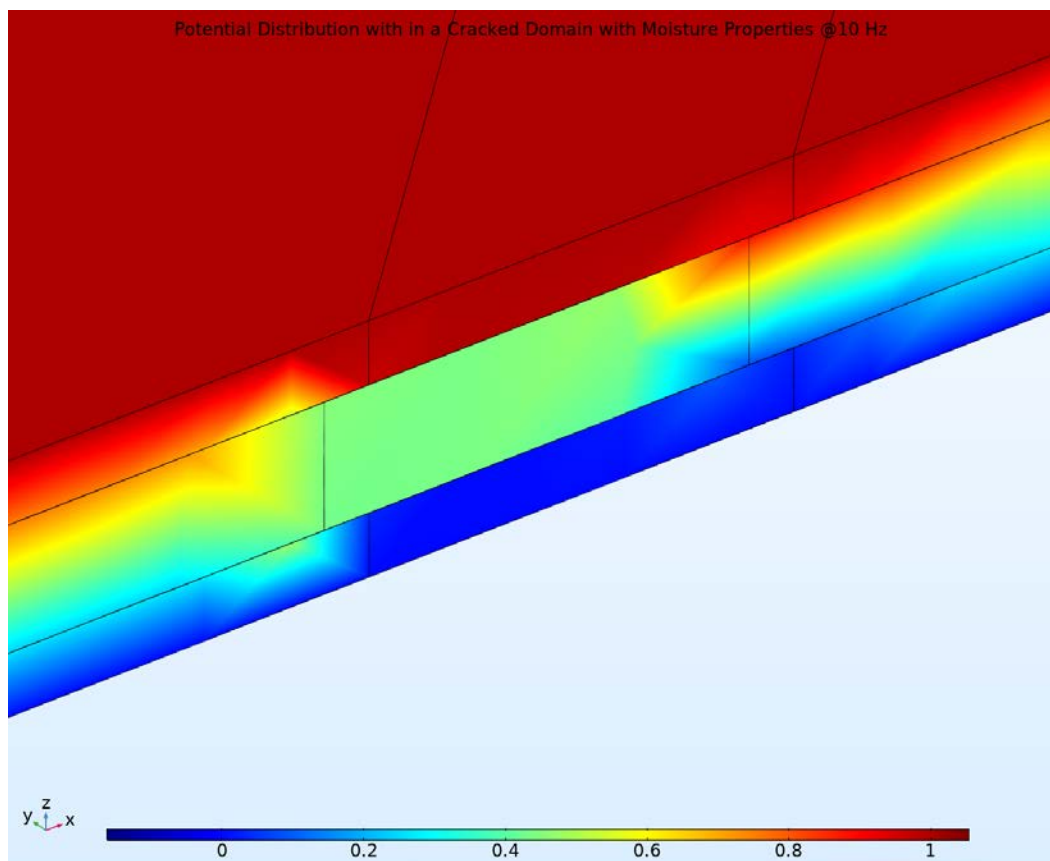

Figure 5.12 Potential distribution through thickness with in a cracked domain with moisture
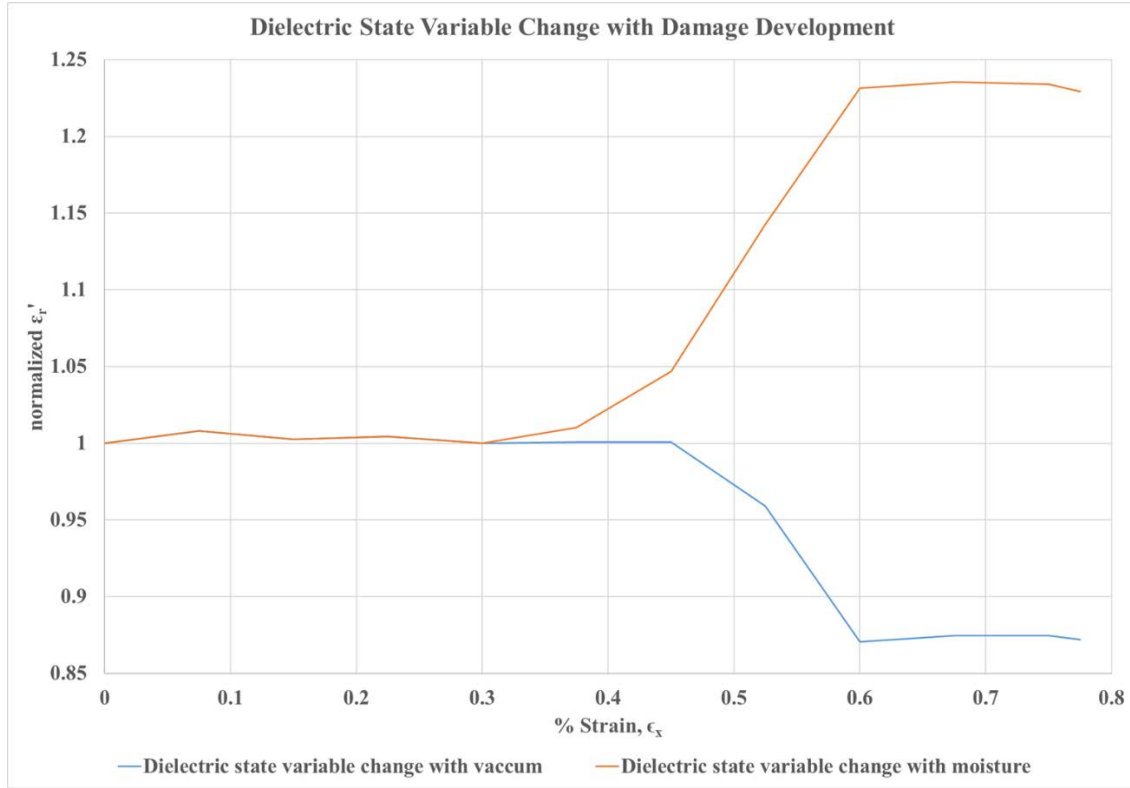
Figure 5.13 Dielectric state variable change with damage development

From Figure 5.13, it can be observed that with moisture we simulate interfacial polarization and hence the normalized dielectric state variables increases with damage development. To explain it in the analytical sense, as per the current conservation governing equation $(-\nabla.((jw\varepsilon_0\varepsilon_r + \sigma)\nabla\emptyset) = 0)$; within the cracked domain the potential gradient is almost negligible this results in higher net conductivity $(jw\varepsilon_0\varepsilon_r + \sigma)$ of the volume. If the conductivity increases, the current with in the volume increases as well. If the current with in the volume increases this indicates that $\nabla.J$ of the volume is negative and as per the continuity equation $(\nabla.J = -\frac{\partial\rho}{\partial t})$, a negative $\nabla.J$ indicates $\frac{\partial\rho}{\partial t}$ is positive which indicates that the charge with in the volume is building up resulting in higher capacitance and hence higher permittivity.

In the case of vacuum, since the electric field with in the cracked domain is higher as per the current conservation governing equation this increase in electric field with in the volume is compensated by a drop in the net conductivity of the volume. If net conductivity decreases then the current with in the volume decreases and hence $\nabla . J$ is positive. A positive $\nabla . J$ indicates $\frac{\partial \rho}{\partial t}$ is negative which indicates that the charge with in the volume is dissipating resulting in reduced capacitance and hence lower permittivity.

However, if we compare the simulated dielectric state variable change with the observed variation, there is a discrepancy not with respect to strain but with the trend of the dielectric response as shown below in Figure 5.14, there is a significant drop in the dielectric state variable with damage development. This discrepancy is observed because we haven't modeled delamination in the dielectric perspective.
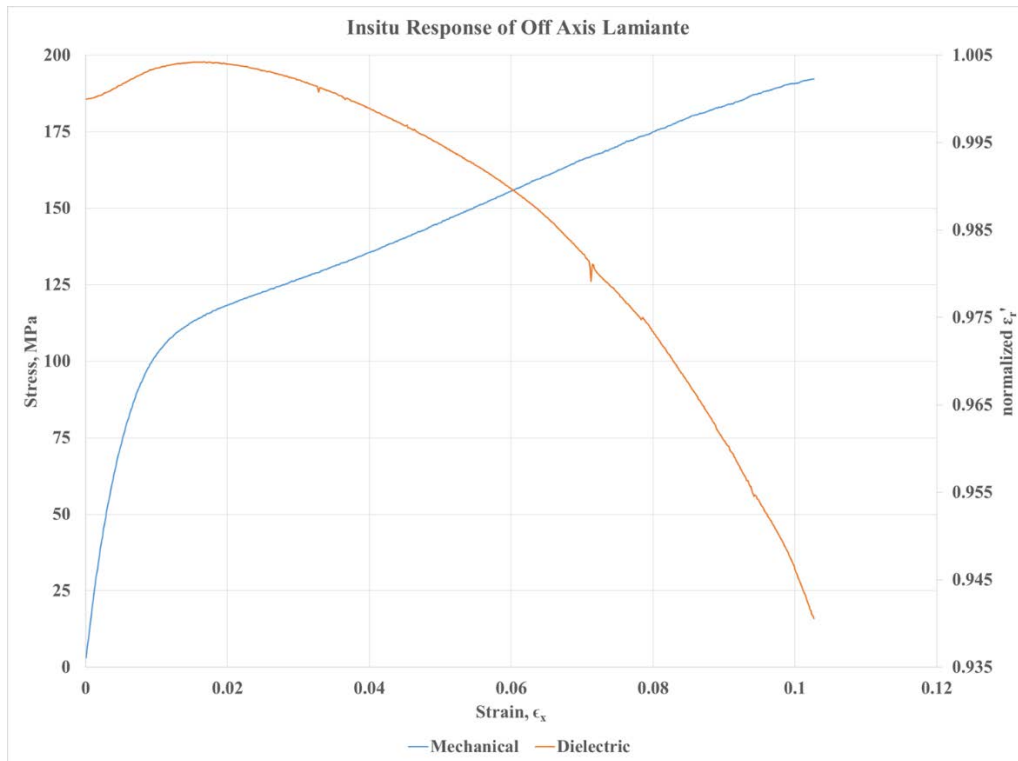

Figure 5.14 Observed insitu response of the off axis laminate

To model delamination in the dielectric perspective, it is important to revisit the Maxwell's boundary conditions across the interface of two heterogeneous dielectric materials. Let's say that we have two dielectric materials stacked together with similar or different dielectric properties now for the electric displacement field to be continuous across this interface the boundary condition at this interface would be given by Eq. (5.15).

$$n. D_1 = n. D_2 \tag{5.15}$$

However, now when a delamination is developed at the interface between the two materials, then the boundary is discontinuous and hence there can be no flux across the interface between the two materials which is given by Eq. (5.16).

$$n. D_1 = n. D_2 = 0 \tag{5.16}$$

To validate these boundary conditions, we modeled a 2D laminate with two plies stacked. The continuity at the interface is governed by Eq. (5.15). The finite element mesh and the boundary conditions are shown below in Figure 5.15. The potential distribution is continuous as shown below in Figure 5.16.

Now let's say an initial delamination of length 2a is created at the interface between (-a, 0.5) and (a, 0.5) as shown below in Figure 5.17. We start with (a = 0.25 mm) and run a parametric sweep till (a = 10 mm). The potential distribution for (a = 0.25 mm) is shown in Figure 5.18. The distribution is no longer uniform and is discontinuous in the delaminated region. The potential distribution for (a = 10 mm) is shown in Figure 5.19. It can clearly be observed that because of the delamination the second ply is isolated from the electric field and the potential distribution is continuous only where the continuity boundary still exists at the ends of the plies.
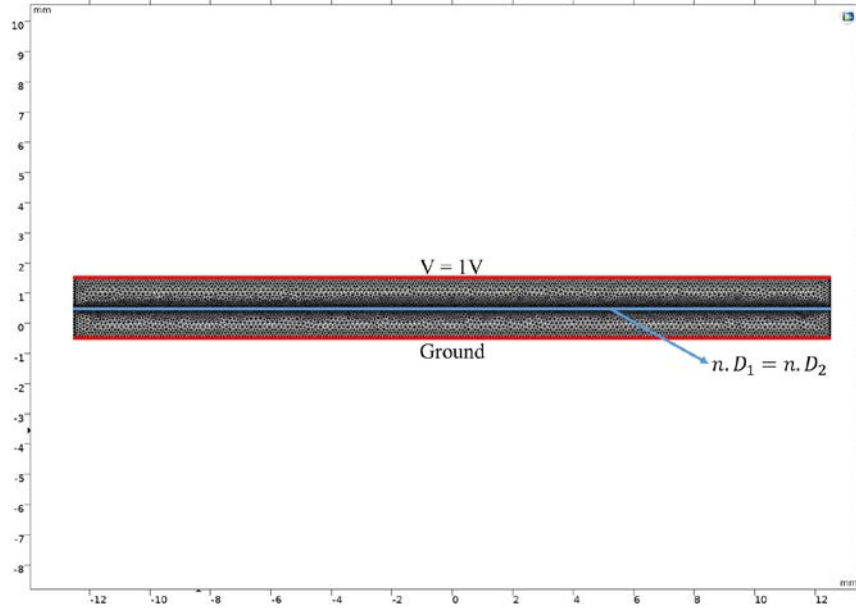
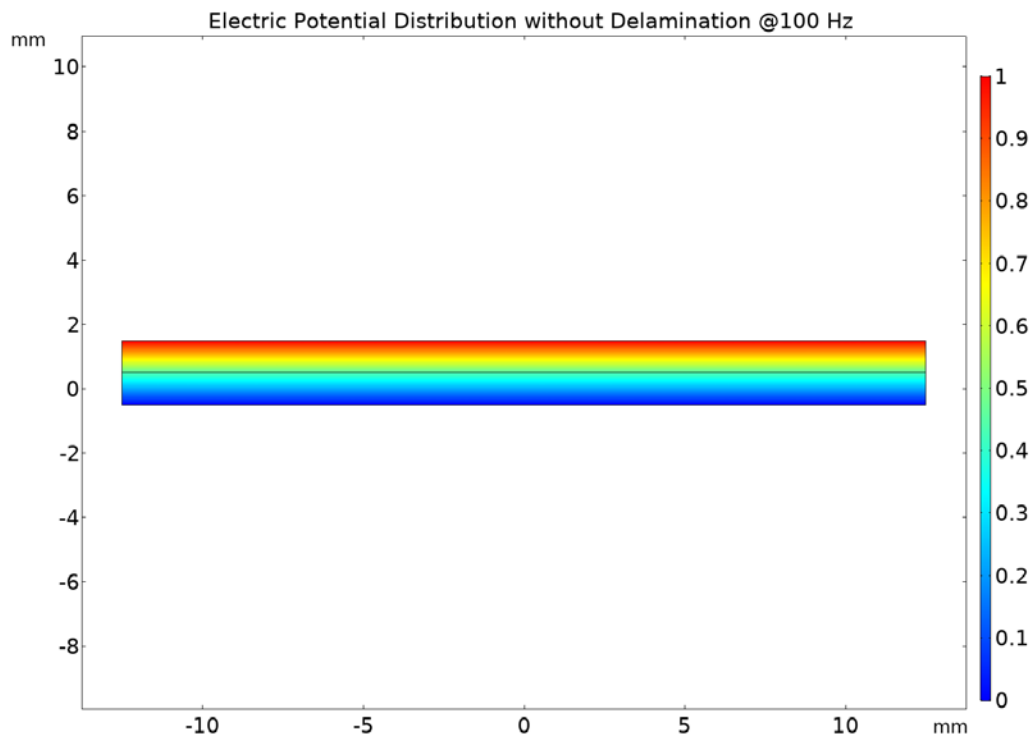Figure 5.15 FEM with boundary conditions for the initial model without delamination

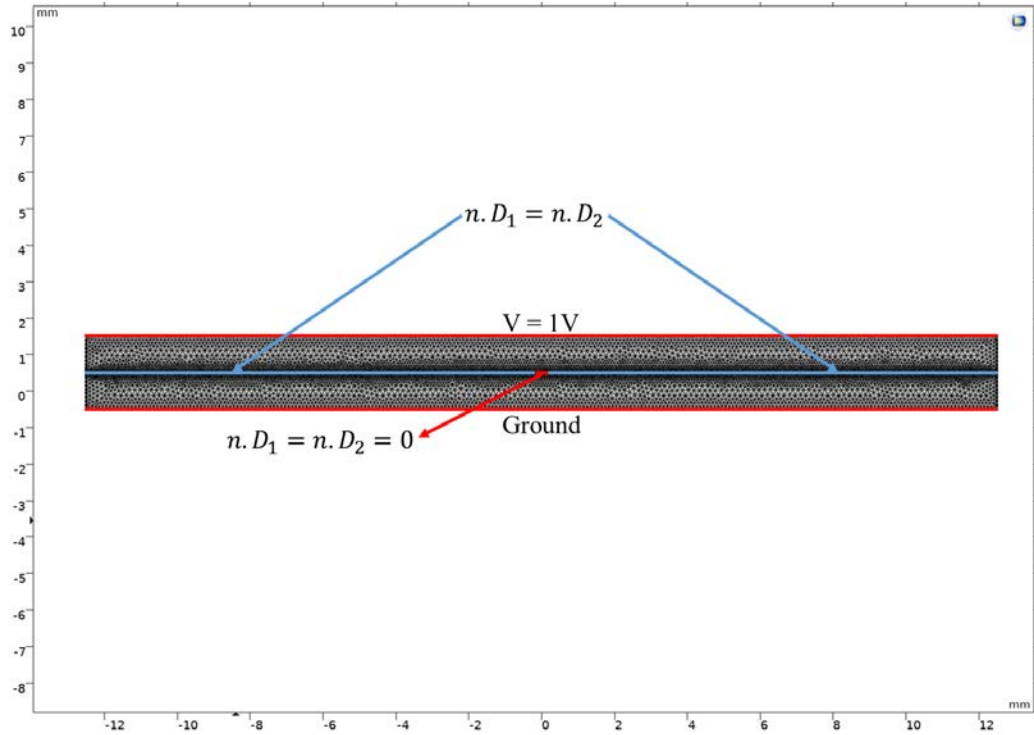Figure 5.16 Electric potential distribution without delamination @100 Hz

Figure 5.17 FEM with boundary conditions for the model with initial delamination (a=0.25mm)
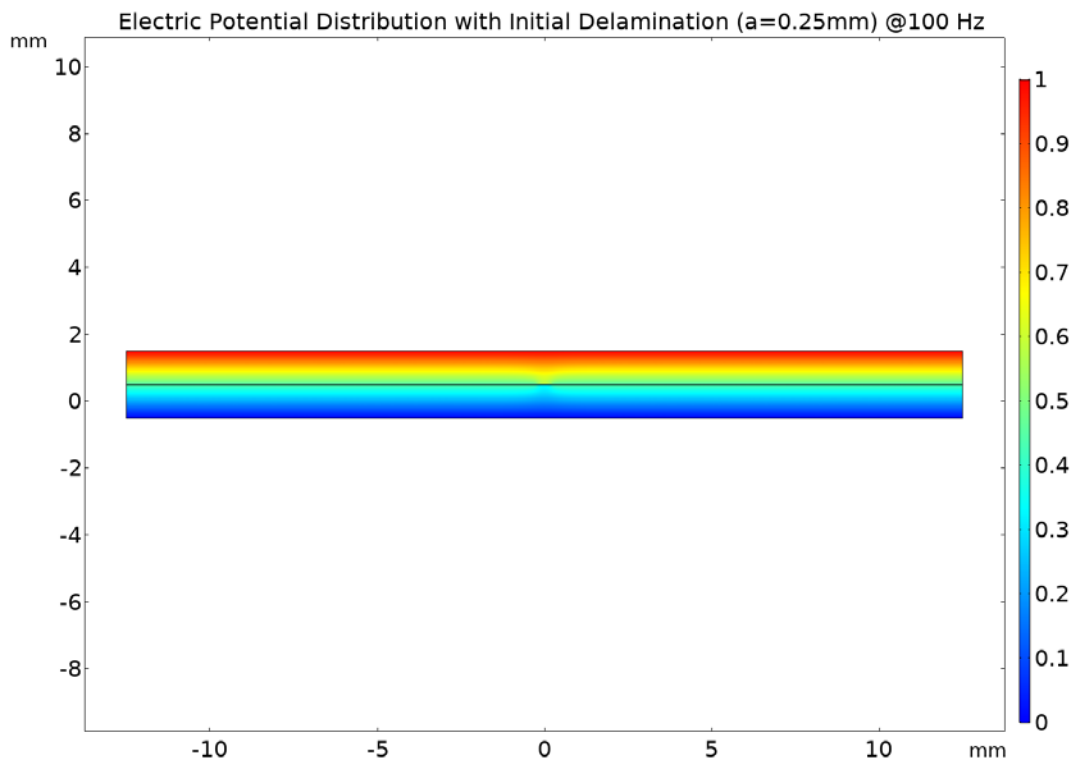
Figure 5.18 Electric potential distribution with initial delamination (a=0.25mm) @100 Hz
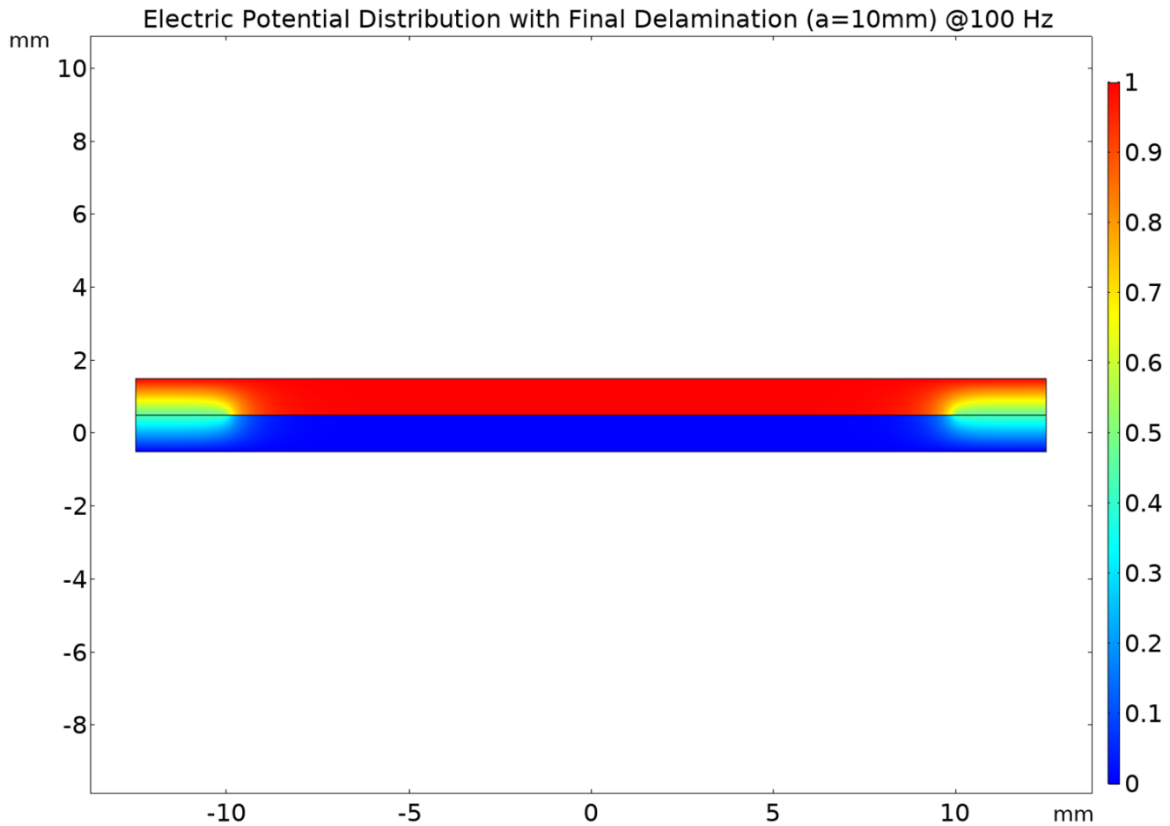
Figure 5.19 Electric potential distribution with final delamination (a=10 mm) @ 100 Hz

This is very analogous to what one would observe in a delaminated composite laminate. For example, a [0/90]$_s$ laminate. The delamination at the interface of the 0/90 results in all the load transfer to the 0° ply as shown below in Figure 5.20. The illustration shown below is from a cross ply simulation under uni axial tensile loading. The stress in the 90° ply is transferred to the 0° ply because of delamination, the similar analogue in the dielectric perspective is there is no electric field in the isolated region.
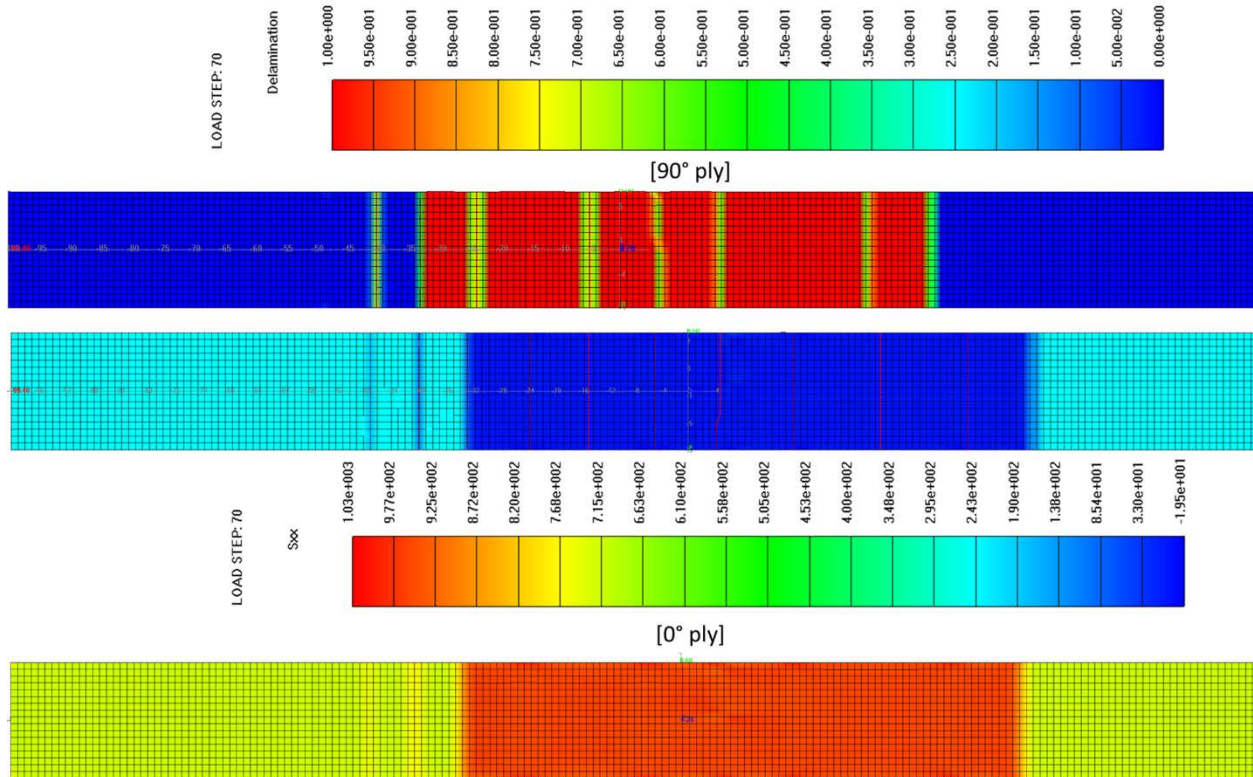
Figure 5.20 Illustration of delamination and load transfer in a cross-ply laminate

The next big question is, what is the effect of delamination on the dielectric state variable? Let's understand this analytically. Delamination is enforced by the boundary condition $n.D_1 = n.D_2 = 0$. This implies that in the volume under consideration once a delamination occurs the electric displacement field in the volume decreases and hence the time varying displacement electric field current $\frac{\partial\rho}{\partial t}$ decreases. This implies that the charge inside the volume is dissipating and hence the capacitance reduces and hence ε_r decreases as observed below in Figure 5.21.
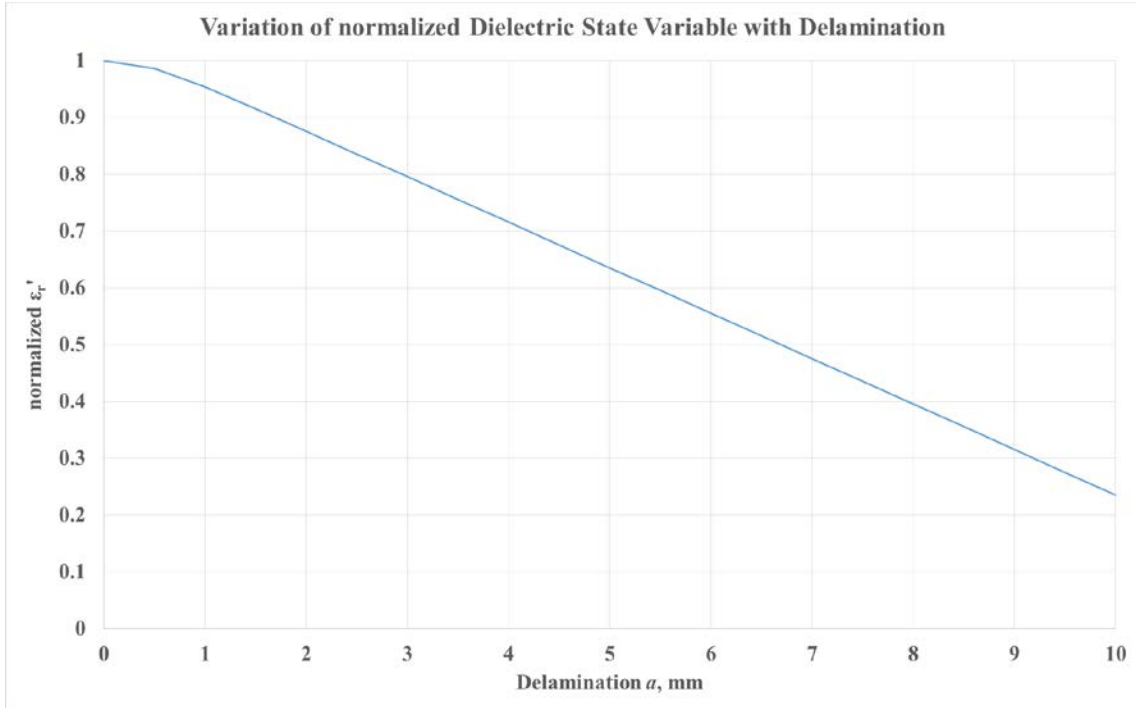
Figure 5.21 Variation of normalized ε_r with delamination growth

Figure 5.21 illustrates that ε_r varies linearly with delamination growth as *a* is modeled to grow linearly. In a real laminate, delamination initiates, slowly grows and coalesces rapidly at the end leading to failure and hence in our insitu experimental results we always observe the slope changes of the dielectric state variable during the interaction of discrete damage events. Now after including delamination in the multiphysics model the simulated trend is similar to observed trend as shown in Figure 5.22.
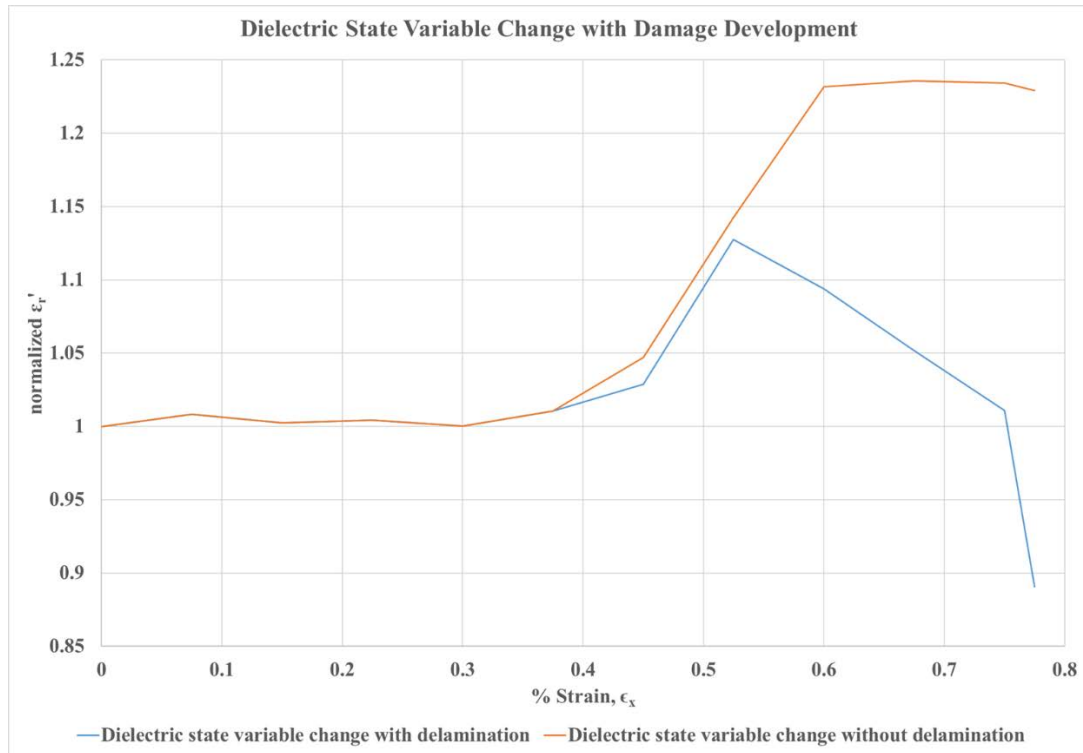
Figure 5.22 Simulated dielectric state variable change with and without delamination

5.6 References

[1]   Maimí, P., Camanho, P. P., Mayugo, J. A., & Dávila, C. G. (2007). A continuum damage model for composite laminates: Part I–Constitutive model. Mechanics of Materials, 39(10), 897-908.

[2]   Maimí, P., Camanho, P. P., Mayugo, J. A., & Dávila, C. G. (2007). A continuum damage model for composite laminates: Part II–Computational implementation and validation. Mechanics of Materials, 39(10), 909-919.

[3]   Alfano, G., & Crisfield, M. (2001). Finite element interface models for the delamination analysis of laminated composites: mechanical and computational issues. International journal for numerical methods in engineering, 50(7), 1701-1736.

[4]   Jiang, W. G., Hallett, S. R., Green, B. G., & Wisnom, M. R. (2007). A concise interface constitutive law for analysis of delamination and splitting in composite materials and its application to scaled

notched tensile specimens. International journal for numerical methods in engineering, 69(9), 1982-1995.

[5]   Turon, A., Camanho, P. P., Costa, J., & Dávila, C. G. (2006). A damage model for the simulation of delamination in advanced composites under variable-mode loading. Mechanics of materials, 38(11), 1072-1089.

[6]   Krueger, R. (2004). Virtual crack closure technique: history, approach, and applications. Appl. Mech. Rev., 57(2), 109-143.

[7]   Deobald, L., Mabson, G., Dopker, B., Hoyt, D., Baylor, J., & Graesser, D. (2007, April). Interlaminar fatigue elements for crack growth based on virtual crack closure technique. In 48th AIAA/ASME/ASCE/AHS/ASC Structures, Structural Dynamics, and Materials Conference (p. 2091).

[8]   Wawrzynek, P. A., & Ingraffea, A. R. (1989). An interactive approach to local remeshing around a propagating crack. Finite Elements in Analysis and Design, 5(1), 87-96.

[9]   Iarve, E. V., Gurvich, M. R., Mollenhauer, D. H., Rose, C. A., & Dávila, C. G. (2011). Mesh-independent matrix cracking and delamination modeling in laminated composites. International journal for numerical methods in engineering, 88(8), 749-773.

[10]   Adluru, H. K., Hoos, K. H., Iarve, E. V., & Ratcliffe, J. G. (2019). Delamination initiation and migration modeling in clamped tapered laminated beam specimens under static loading. Composites Part A: Applied Science and Manufacturing, 118, 202-212.

[11]   McQuien, J. S., Adluru, H. K., Iarve, E., & Harman, A. (2019). A global-local discrete damage modeling framework for composite laminates. In AIAA Scitech 2019 Forum (p. 1550).

[12]   Pinho, S. T., Dávila, C. G., Camanho, P. P., Iannucci, L., & Robinson, P. (2005). Failure models and criteria for FRP under in-plane or three-dimensional stress states including shear non-linearity.

[13]   Bathe, K. J., Zhang, H., & Yan, Y. (2014). The solution of Maxwell's equations in multiphysics. Computers & Structures, 132, 99-112.

[14]   Guo, S., & Ghosh, S. (2014). A finite element model for coupled 3D transient electromagnetic and structural dynamics problems. Computational Mechanics, 54(2), 407-424.

[15]   Trimarco, C. (2007). Material electromagnetic fields and material forces. Archive of Applied Mechanics, 77(2-3), 177-184.

[16]   Sillars, R. W. (1937). The properties of a dielectric containing semiconducting particles of various shapes. Journal of the Institution of Electrical Engineers, 80(484), 378-394.

[17]   Banhegyi, G. (1988). Numerical analysis of complex dielectric mixture formulae. Colloid and Polymer Science, 266(1), 11-28.

[18]   Leone, F. A., Davila, C. G., Mabson, G. E., Ramnath, M., & Hyder, I. (2017). Fracture-based mesh size requirements for matrix cracks in continuum damage mechanics models. In 58th AIAA/ASCE/AHS/ASC Structures, Structural Dynamics, and Materials Conference (p. 0198).

[19]   Vadlamudi, V., Shaik, R., Raihan, R., Reifsnider, K., & Iarve, E. (2019). Identification of Current Material State in Composites using a Dielectric State Variable. Composites Part A: Applied Science and Manufacturing, 105494.

[20]   Marom, G., & White, E. F. T. (1972). Improvements in the transverse properties of composites. Journal of Materials Science, 7(11), 1299-1307.

[21]   Ilcewicz, L. B., Keary, P. E., & Trostle, J. (1988). Interlaminar fracture toughness testing of composite mode I and mode II DCB specimens. Polymer Engineering & Science, 28(9), 592-604.

[22]   El-Sa'ad, L., Darby, M. I., & Yates, B. (1990). Moisture absorption by epoxy resins: the reverse thermal effect. Journal of Materials Science, 25(8), 3577-3582.

[23]   Chahal, R., Adnan, A., Reifsnider, K., Raihan, R., Ting Wu, Y., Vadlamudi, V., & Elenchezhian, M. R. P. (2018). Molecular Dynamics for the Prediction of the Interfacial Shear Stress and Interface Dielectric Properties of Carbon Fiber Epoxy Composites. Proceedings of the American Society for Composites—Thirty-third Technical Conference.

[24]   Bond, D. A., & Smith, P. A. (2006). Modeling the transport of low-molecular-weight penetrants within polymer matrix composites. Applied Mechanics Reviews, 59(5), 249-268.

Conclusions and Future Research Direction

The motivation of this work is the sudden death behavior of composite materials which makes it challenging to make the assessment of how 'critical' the material state is given the damage tolerant behavior of composites. Given the complexity of damage modes; the location of the damage is mostly internal. Using advanced non-destructive evaluation (NDE) techniques one can accurately determine the location and nature of damage; however by the time that information is obtained the structure would have already lost its load bearing capability and we are still left with the inability of these NDE techniques to answer the question, what is the current material state and is it 'critical'?

The starting point of this work is the experimental findings, where the in-situ variation of the dielectric state variable with various stages of damage development was obtained. However, the physics behind the variation of the response with damage development was not clearly determined.

In the quest to understand the physics, we started with the Maxwell's equation of conservation of current in a volume ($\nabla . J + \frac{\partial \rho}{\partial t} = 0$) which requires that the flow of charge in the volume to be conserved. However, in the real material during development of damage, the source term (RHS of the equation) will no longer be 0, but is dependent on different physical phenomenon (such as fracto emission Figure 2.2). On the application of a time harmonic electric field and simplifying the Maxwell's equation leads us to ($\nabla . ((jw\varepsilon_0\varepsilon_r + \sigma)\mathrm{E}) = J_{source}$). This equation suggests that the perturbation caused by J_{source} in a volume has to be balanced by the product of ($jw\varepsilon_0\varepsilon_r + \sigma$)$\mathrm{E}$ of the volume in order to be in equilibrium. This fundamental necessity of

equilibrium is the reason why the dielectric properties of the material change during damage development.

Given the complexity of the physical phenomenon, approximating the magnitude or nature of J_{source} is not straight forward and hence we solved the inverse problem instead in this work as the nature of the global variation of dielectric properties with damage development (from experiments) was known. So we first predicted the discrete damage events using Rx-FEM. Now, from the original form of Maxwell's equation (without the source term), $(\nabla.\left((jw\varepsilon_0\varepsilon_r + \sigma)E\right) = 0)$, the product of $(jw\varepsilon_0\varepsilon_r + \sigma)E$ has to be constant to maintain equilibrium. Combining this with Maxwell-Wagner-Sillars polarization theory, we developed a CDM approach to locally vary the dielectric properties (of damaged regions (matrix cracks)), and enforced Maxwell's continuity boundary conditions at the interface between the plies (for delaminations), and we were able to predict/simulate the observed global dielectric response.

From this phenomenological model, we were able to interpret the observed variation of dielectric response during damage development. Primarily when matrix cracks form, the charge displacement due to externally applied electric field is impeded at the cracks surfaces and hence results in charge trapping at these interfaces. This trapping (accumulation) of charges results in increase in capacitance and hence the increase in permittivity ε_r of the material. On continued loading, secondary cracks are created in the neighboring plies due to the change in stress state triggered by the primary matrix cracks. The coupling of these cracks at the free edge induces edge delaminations resulting in an increase in permittivity ε_r with a reduced slope (due to local volume isolations). As these cracks grow across the width, interior delaminations are induced (where the cracks cross each other) hence resulting in a decrease in permittivity ε_r with a gradual slope (due to local volume isolations). Under continued loading, these cracks tend to grow at a higher rate

resulting in coalescence of delaminations leading to local failures and hence increased rate of decrease of permittivity ε_r (due to increase in rate of local volume isolations). These locally failed regions find a path which are then aided by fiber fractures leading to a sudden drop in the strength and final failure and hence an accelerated decrease in permittivity ε_r (due to global volume isolation).

These findings were validated with different stacking sequences resulting in different sequence and/or rate of damage mechanisms and hence different global dielectric response variations.

However there are questions to think about; is there any alternate explanation for the variation of response? Is delamination represented by Maxwell's boundary condition the only responsible mechanism leading to drop in permittivity? The other aspects that need to be investigated are the environmental effects which haven't been included in this work and these play a vital role in understanding and predicting long term behavior of composites.

From the multiphysics perspective, there is a need to develop a fully coupled analysis where in the stress field which leads to increase in strain energy of the material resulting in damage development that results in instantaneous release of this energy leading to formation of new surfaces (fracture mechanics), acoustic emissions, localized heating (thermal) and emission of charges (fracto emission) and other physical phenomenon. If the physics is accurately modeled, then it would now be an engineering challenge to be able to develop and apply this technique in structures to monitor the real time material state and provide warning of impending failure.

The goal of this work was to present a single 'state' variable that could capture the interaction of damage events that develop during service and be able to provide an assessment of

how 'critical' the state of the material is which can be used by an engineer to make a call on either repair/replace the component to avoid catastrophic failures. We believe this work is a major step forward in that direction.